ABSTRACT

Title of Document: EVALUATION OF MASS FILTERED, TIME DILATED, TIME-OF-FLIGHT MASS SPECTROMETRY

Leonard Thomas Demoranville, Ph.D., 2010

Directed By: Professor Alice C. Mignerey, Department of Chemistry and Biochemistry

The Naval Research Laboratory's Trace Element Accelerator Mass Spectrometer (NRL-TEAMS) system offers a unique opportunity to develop a new type of time-of-flight (TOF) SIMS. This opportunity derives from use of a Pretzel magnet as a recombinator and mass filter in the injector to the accelerator. Mass filtering prior to time-of-flight analysis removes extraneous species, shortening the analysis time for a single beam pulse, thereby improving the duty cycle. Using this approach, it is possible to obtain an expanded portion of a narrow segment of the entire time-of-flight spectrum created by a single beam pulse. A longer flight path for greater momenta in the Pretzel magnet introduces time dilation. Potential benefits derived from time dilation and mass filtering include improved duty cycle, shorter analysis time, increased precision, and better resolution.

While the NRL-TEAMS system is not designed for TOF work, it has been used as a test bed to prove the theoretical benefit of such a design. Theoretical

Report Documentation Page

Form Approved
OMB No. 0704-0188

1. REPORT DATE	2. REPORT TYPE	3. DATES COVERED
2010		**00-00-2010 to 00-00-2010**

4. TITLE AND SUBTITLE	5a. CONTRACT NUMBER
Evaluation of Mass Filtered, Time Dilated, Time-Of-Flight Mass Spectrometry	5b. GRANT NUMBER
	5c. PROGRAM ELEMENT NUMBER
6. AUTHOR(S)	5d. PROJECT NUMBER
	5e. TASK NUMBER
	5f. WORK UNIT NUMBER
7. PERFORMING ORGANIZATION NAME(S) AND ADDRESS(ES) **University of Maryland, College Park,College Park,MD,20742**	8. PERFORMING ORGANIZATION REPORT NUMBER
9. SPONSORING/MONITORING AGENCY NAME(S) AND ADDRESS(ES)	10. SPONSOR/MONITOR'S ACRONYM(S)
	11. SPONSOR/MONITOR'S REPORT NUMBER(S)

12. DISTRIBUTION/AVAILABILITY STATEMENT
Approved for public release; distribution unlimited

13. SUPPLEMENTARY NOTES

14. ABSTRACT

The Naval Research Laboratory?s Trace Element Accelerator Mass Spectrometer (NRL-TEAMS) system offers a unique opportunity to develop a new type of time-offlight (TOF) SIMS. This opportunity derives from use of a Pretzel magnet as a recombinator and mass filter in the injector to the accelerator. Mass filtering prior to time-of-flight analysis removes extraneous species, shortening the analysis time for a single beam pulse, thereby improving the duty cycle. Using this approach, it is possible to obtain an expanded portion of a narrow segment of the entire time-offlight spectrum created by a single beam pulse. A longer flight path for greater momenta in the Pretzel magnet introduces time dilation. Potential benefits derived from time dilation and mass filtering include improved duty cycle, shorter analysis time, increased precision, and better resolution. While the NRL-TEAMS system is not designed for TOF work, it has been used as a test bed to prove the theoretical benefit of such a design. Theoretical treatments of the spectrometer have shown improved resolution is possible under certain conditions, when compared to a traditional TOF spectrometer. SIMION 8.0 computer simulations were used to model the system and provide insight to the theoretical capabilities of the Pretzel magnet. As expected, models have shown that as field decreases, and therefore path length increases, mass resolution improves. Generally, the model matched well to experimental results provided by the NRL TEAMS system. These experimental results have predicted fundamental parameters of the system accurately and consistently, and confirmed the validity of the model. This research improved the current system?s performance through improved electronics and pulsing and further uses the model to predict the theoretical benefits of a system designed for use with a Pretzel magnet.

15. SUBJECT TERMS

16. SECURITY CLASSIFICATION OF:			17. LIMITATION OF ABSTRACT	18. NUMBER OF PAGES	19a. NAME OF RESPONSIBLE PERSON
a. REPORT **unclassified**	b. ABSTRACT **unclassified**	c. THIS PAGE **unclassified**	**Same as Report (SAR)**	**168**	

Standard Form 298 (Rev. 8-98)
Prescribed by ANSI Std Z39-18

treatments of the spectrometer have shown improved resolution is possible under certain conditions, when compared to a traditional TOF spectrometer. SIMION 8.0 computer simulations were used to model the system and provide insight to the theoretical capabilities of the Pretzel magnet. As expected, models have shown that as field decreases, and therefore path length increases, mass resolution improves. Generally, the model matched well to experimental results provided by the NRL TEAMS system. These experimental results have predicted fundamental parameters of the system accurately and consistently, and confirmed the validity of the model. This research improved the current system's performance through improved electronics and pulsing and further uses the model to predict the theoretical benefits of a system designed for use with a Pretzel magnet.

EVALUATION OF MASS FILTERED, TIME DILATED, TIME-OF-FLIGHT MASS SPECTROMETRY

By

Leonard Thomas Demoranville

Dissertation submitted to the Faculty of the Graduate School of the
University of Maryland, College Park, in partial fulfillment
of the requirements for the degree of
Doctor of Philosophy
2010

Advisory Committee:
Professor Alice C. Mignerey, Chair
Associate Professor James Farquhar
Dr. Kenneth S. Grabowski
Professor Emeritus George Helz
Professor William Walters

Foreword

This thesis includes portions two previously published works, primarily authored by Leonard Demoranville: “Testing of mass filtered, time dilated, time-of-flight mass spectrometry L. T. Demoranville, D. L. Knies, K. S. Grabowski, A. C. Mignerey Journal of Radioanalytical Nuclear Chemistry 282, 2009, 305” and “Experimental demonstration of mass-filtered, time-dilated, time-of-flight mass spectrometry. L. T. Demoranville, K. S. Grabowski, D. L. Knies, C. Cetina, Surface and Interface Analysis, 2010”. Leonard made substantial contributions to the relevant aspects of the jointly authored work included in the thesis and was the primary author of these articles.

-Dr. Alice C. Mignerey

Dedication

To Kristin,

Thank you for being “that witness to my life”.

Acknowledgements

In this small space it is impossible to acknowledge all those who have influenced my life and the creation of this document. To all those family, friends, and mentors that are not mentioned specifically, thank you for your continual support and patience as I have gone through this journey.

To my colleagues Mara Dougherty and Cassandra Taylor, at University of Maryland, and Dr. Catalina Cetina, at the Naval Research Laboratory (NRL), thank you for sharing my daily trials and travails, both personal and professional.

To the several technicians at NRL that kept the facility running, Britton Renfro, Victor Cestone, and Claire Kennedy, this thesis is a testimony to the work you do every day.

I must also thank several scientific mentors. Dr. Lowell Hall, my undergraduate advisor, was the first person to encourage my entrance to graduate school. For that, and so many other pieces of advice, I am forever grateful. Dr. Alice Mignerey, my graduate advisor, has been the best guide through the graduate school process I could have imagined. Her willingness to let her students explore various interests is unparalled. Without her encouragement and input, this thesis would not be possible. Dr. Kenneth Grabowski has been a phenomenal mentor. He is constantly pushing those around him toward a deeper understanding of data. I could always depend on his critical eye to strengthen an argument. Finally, without Dr. David Knies, this thesis would not exist. He conceptualized Mass Filtered, Time Dilated, Time-of-Flight Mass Spectrometry and has allowed me, with his assistance, to bring the idea to fruition; for that, I am indebted.

Table of Contents

List of Tables

List of Figures

Chapter 1: Nuclear Forensics

Beginning with the end of the Cold War, smuggling of nuclear material began to receive attention. The terrorist attacks of 9-ll reinforced the need for improved security from such threats. Around that time a spike in interdicted nuclear material was observed. To determine the source and potential use of this nuclear material and improve detection capabilities, governments began funding new scientific endeavors in the field of nuclear forensics.

Nuclear forensics is the scientific field that endeavors to analyze nuclear materials interdicted in cases of smuggling or obtained through investigations of nuclear facilities or post-detonation scenarios. These analyses work to establish the chemical, elemental and isotopic composition and physical characterization of the material in order to provide insight to the source, age, and intended use of the material. More complete overviews of the state-of-the-art can be found in May et al. (2008) and Moody et al. (2005).

Nuclear forensics employs radiometric techniques traditionally used with nuclear materials, i.e. counting methods, gamma spectroscopy, along with techniques which are used more broadly, such as mass spectrometry. Mass spectrometry can be used to aid in the determination of many attributes important to the nuclear forensics investigation. The background of mass spectrometry will be developed in Chap. 2, but its general application to nuclear forensics will be discussed here.

Magnetic sector mass spectrometry is routinely used to determine the isotopic composition of a sample of nuclear material, which provides information regarding the intended use and age of the material. Enrichment of specific isotopes can indicate

the use of the material for peaceful purposes or for weapons. The presence of certain isotopes in a uranium sample, ^{236}U for instance, indicates the material has been irradiated, as that isotope is not present in natural samples. For plutonium and uranium the half-life of a given isotope and its decay products are well known. By measuring the composition of a given sample and comparing the specific isotopic and elemental information, it may be possible to determine the age of a sample. This age corresponds to the last time of separation and can be used to narrow the origin of the sample.

In addition to determining the use and age of a sample, knowing its origin is also a concern. For some samples, oxygen isotope ratios can offer insight into the location of a sample's origin. During the processing of uranium ore into reactor pellets, the sample is converted into a uranium dioxide compound. This compound will contain the oxygen isotope ratio of the water used in the processing. While this ratio will be disturbed if the pellet is irradiated, it is possible to use the oxygen isotope ratio of a non-irradiated pellet to determine its probable processing location. Further, some studies have suggested the isotopic composition of plutonium samples can be used to determine the type of reactor used in its creation (Wallenius et al., 2000). Others have suggested the use of several rare earth elements, produced as activation and fission products in the reactor, and metallic impurities may be able to be used for a similar purpose (Mayer and Wallenius, 2008; Weaver et al., 2009).

In all of the cases, instrumentation exists that can be used to collect the desired information. Yet, all the measurements could benefit from increased capabilities. The joint American Physical Society-American Association for the

Advancement of Science working group on nuclear forensics pointed to the need for small, automated, field-deployable instruments, specifically mass spectrometers, to speed the collection of information (May et al., 2008). Researchers developing the isotope ratio procedures for nuclear forensics have suggested improvements are needed in mass resolution, because as mass resolution increases, sensitivity decreases (Esaka et al., 2007; Török et al., 2004). Others have noted the need for more routinely available techniques that can improve isotopic ratios of uranium near the natural abundance (Mayer and Wallenius, 2008). These factors have led to the investigation of mass filtered, time dilated, time-of-flight mass spectrometry to determine if it could advance the field of mass spectrometry for nuclear forensics.

Chapter 2: Mass Spectrometry

Mass spectrometry is an analytical technique used to determine the chemical, elemental, or isotopic composition of a material by ionizing the analyte and measuring the mass-to-charge ratio. Typical mass spectrometers are composed of three main parts: an ion source, mass analyzer, and detector. Improvements to any one of these three components can lead to advances in mass spectrometry and this thesis evaluates the utility of a Pretzel magnet as an improved mass analyzer. Skoog et al. (2007) present a more complete view of mass spectrometry, the types of instruments currently available, and their applications.

Section 2.1: Applications of Mass Spectrometry

Mass spectrometry is used for a host of applications across the natural sciences. Improvements in mass spectrometry instrumentation have led to advances in many areas that would not have otherwise been possible. The development of accelerator mass spectrometry (AMS) significantly advanced the field of radiocarbon dating, allowing older and smaller samples to be dated with greater precision than was possible with radiometric counting techniques. Progress in Matrix Assisted Laser Desorption/Ionization (MALDI) and Electrospray Ionization (ESI) ion sources for mass spectrometers significantly improved the characterization of proteins and peptides. Work on orthogonal acceleration mass spectrometry (OA-MS) increased the ability of mass spectrometers to be coupled with continuous sources, such a gas chromatographs and capillary electrophoresis. The development of secondary ion mass spectrometry (SIMS) allowed the analysis and imaging of sample surfaces,

resulting in research advances in areas as scientifically diverse as comsochemistry and bio-medicine. The creation of new ion sources and mass analyzers enabled progress in many fields and further research continues to contribute improvements to various techniques for mass spectrometry.

Section 2.2: Time-of-Flight Mass Spectrometry

The development of time-of-flight (TOF) analysis will not be covered completely here, rather a review of the history of the development written by one of the pioneers of the technique is recommended (Mamyrin 2001). Mamyrin's contribution to TOF analysis was the implementation of reflectron ion mirrors as the TOF mass analyzer (Mamyrin et al. 1973). The reflectron TOF analyzer, Fig. 2.1, enhances mass analysis by correcting, in some measure, for the initial energy dispersion of the analyzed beam.

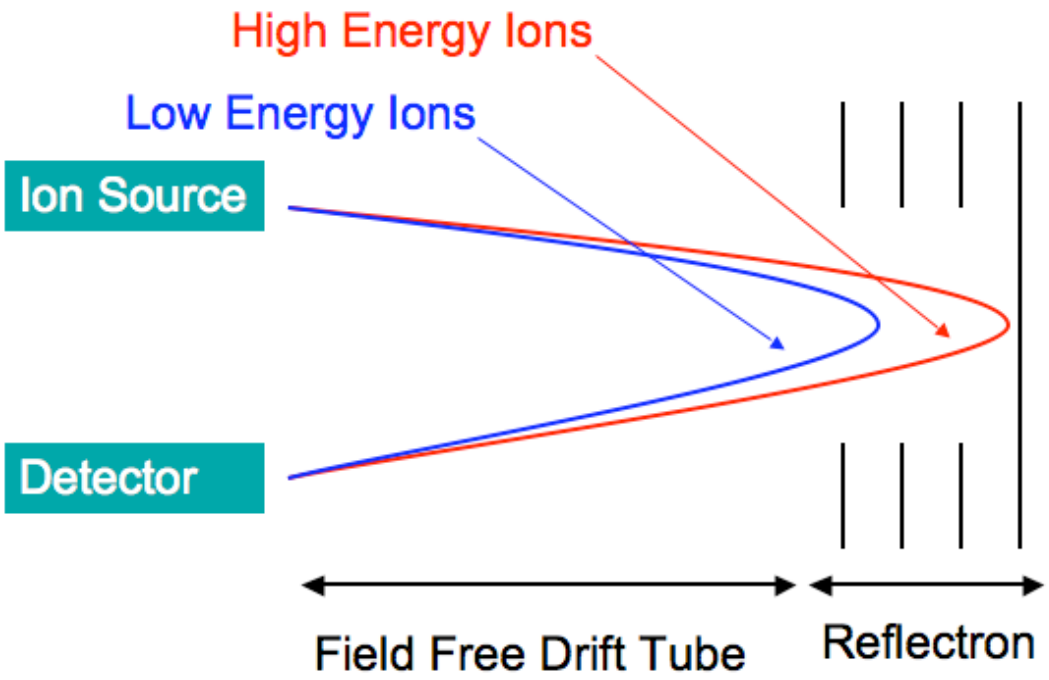

Figure 2.1: Illustration of a reflectron TOF analyzer.

Ions are generally created with a distribution of initial kinetic energies. In TOF analysis this can result in a broadening of the beam over time, causing a decrease in mass resolution. In a reflectron ion mirror, ions entering the electrostatic field with higher energy penetrate further into the field, therefore taking a longer time to reach the detector than if both high and low energy ions followed an identical flight path. Over small energy distributions, this can result in a near perfect energy compensation, with all ions of the same mass arriving at the detector simultaneously (Karataev et al., 1972). Although Mamyrin's review covers the development of the reflectron-style TOF technique, additional developments have occurred to further enhance TOF analysis. These recent developments have sought to improve the mass resolution and duty cycle of TOF instruments so that new applications and improved results may be pursued.

Orthogonal Acceleration TOF (OA-TOF) has taken a different approach to the initial energy distribution problem, while at the same time improving duty cycle. OA-TOF instruments apply the accelerating voltage and conduct the mass analysis orthogonal to the direction of the ion beam. By doing so, the acceleration is decoupled from the direction of the natural drift of the ions. This decoupling means all ions in the beam experience the same acceleration in the direction of analysis and thus have uniform kinetic energy in the direction of analysis, regardless of the initial kinetic energy in the orthogonal direction. Additionally, ions slowly fill the orthogonal accelerator region of the analyzer while the original beam is analyzed. When properly designed, the analysis time can match the fill time, resulting in orders of magnitude improvements in mass analyzer efficiency over other types of TOF-MS,

which is related to duty cycle (Guilhaus et al., 2000). Others have reported duty cycles of 5-15% (Zare et al., 2003). Mass resolutions of up to 10,000 m/δm have been achieved in some circumstances (Guilhaus et al., 2000).

Other developments to improve the duty cycle of TOF-MS have been made in Zare's lab by using Hadamard Transform (HT) TOF-MS (Brock et al., 1998). This type of system uses a sophisticated mathematical transform, the Hadamard transform, to rapidly pulse the primary beam in a pseudo-random, but distinguishable pattern. Thus the analyzed ion packets overlap, but the mass spectrum can be deconvoluted by use of the transform. This can improve the duty cycle of such an instrument up to 100%, by using two detectors (Yoon et al., 2005). The mass resolution of such systems remains at <5,000 m/δm, and it was claimed peptides were detectible at the fmol level under certain conditions (Brock et al., 2000).

Other attempts to improve mass resolution have focused on developing multi-turn TOF-MS systems. These systems employ ion optics that attempt to perfectly focus the ion beam in space and time, resulting in the ability to transmit the beam continuously around the mass spectrometer. As a result, the path length of the transmission of the ions can be extended, without increasing the spectrometer size. These instruments have achieved mass resolution >300,000 m/δm FWHM, but do have problems because of low transmission (Toyoda, 2010).

Thus, several novel approaches to TOF-MS have led to increased applicability and usage of the technique. These approaches have created opportunities for new applications. In the case of OA-TOF and HT-TOF instruments, it has allowed for TOF analysis on continuous sources, such as those coupled with chromatography

instrumentation. Improvements in TOF-SIMS have led to advances in several areas of study, such as bio-molecular studies (Boxer et al., 2009; Fletcher, 2009) and polymer surfaces (Mahoney, 2010). Thus it is important to investigate new approaches to TOF-MS, to determine whether such approaches will improve the state-of-the art of TOF analysis, and thereby create opportunities for new advances in a number of fields.

Section 2.3: Secondary Ion Mass Spectrometry (SIMS)

Secondary Ion Mass Spectrometry (SIMS) is a mass spectrometric technique that differs from other types of mass spectrometry in the way it generates ions. Although more fully explained by Benninghoven et. al. (1987) and Wilson et. al. (1989), SIMS will be briefly described in Sec. 2.3.1.

Subsection 2.3.1: The SIMS Concept

Various types of SIMS instruments exist that utilize magnetic sector, quadrupole, or TOF mass analyzers, but all operate with the same general method of analyte ion creation. In the primary column, an initial ion beam is created, typically at an energy < 30 keV. This initial ion is often Cs^+, O^-, or O_2^+, but many different beams have been used and considerable research effort has been dedicated to the investigation of new primary ion beams. This energetic ion beam bombards the sample, creating a cascade of collisions that impart energy to the sample atoms, some of which gain sufficient energy to leave the sample surface, in a process known as sputtering and illustrated in Fig. 2.2. These sputtered, or secondary particles have low energy, usually <100 eV, and may be sputtered in atomic or molecular form. Most of these

secondary particles are neutral, although some are sputtered as ions. It is the sputtered ions that SIMS analyzes; a slightly different technique, sputtered neutral mass spectrometry, analyzes neutrals by using a post-ionization step. The ionization energy, electron affinity, and composition of the sample matrix dictate the efficiency with which they are sputtered and the type of species, i.e. positive, neutral, negative, that will be formed.

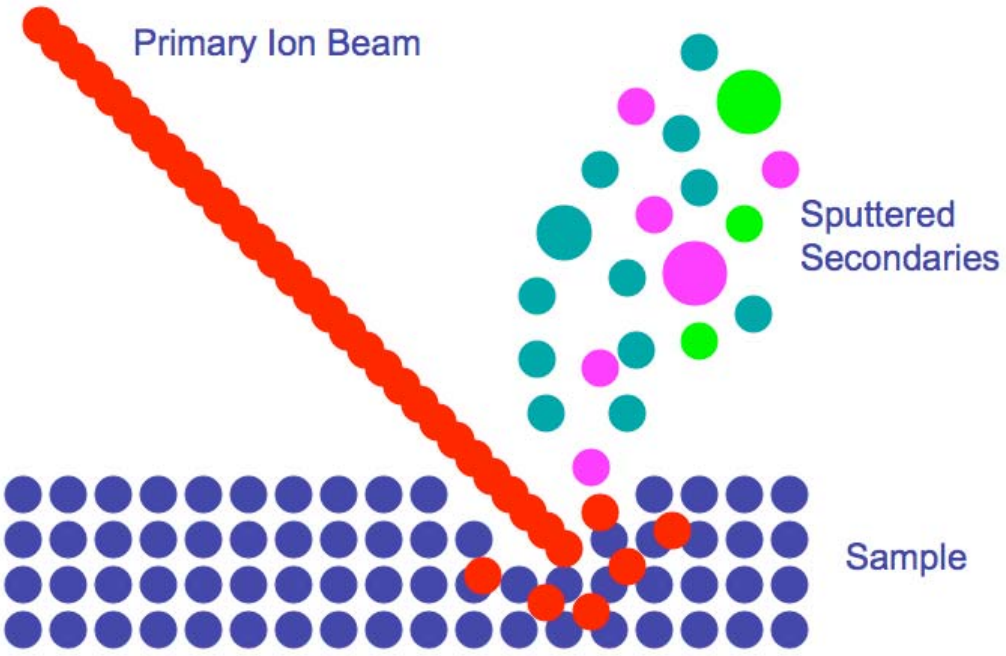

Figure 2.2: Illustration of sputtering in SIMS.

The sputtering process occurs in the first few nanometers of the sample. As the sample is sputtered and layers of the sample are removed, a depth profile may be obtained over time. Also, SIMS instruments provide for rastering, or the movement across the sample of the primary ion beam, which can be correlated to the detection of ions, creating a mass image of the sample. Thus, rather than providing a bulk

measurement, SIMS analysis allows for a depth analysis and determination of where analytes are located within a sample in three dimensions.

The low-energy, sputtered ions are then accelerated, focused with various lenses, collimated with apertures, and steered with other optics, all collectively considered the secondary extraction optics. This focused ion beam is then transmitted to the chosen mass spectrometer. In most cases, this mass spectrometer is a TOF, magnetic sector, or quadrupole instrument. A general block diagram of a SIMS instrument is presented in Fig. 2.3.

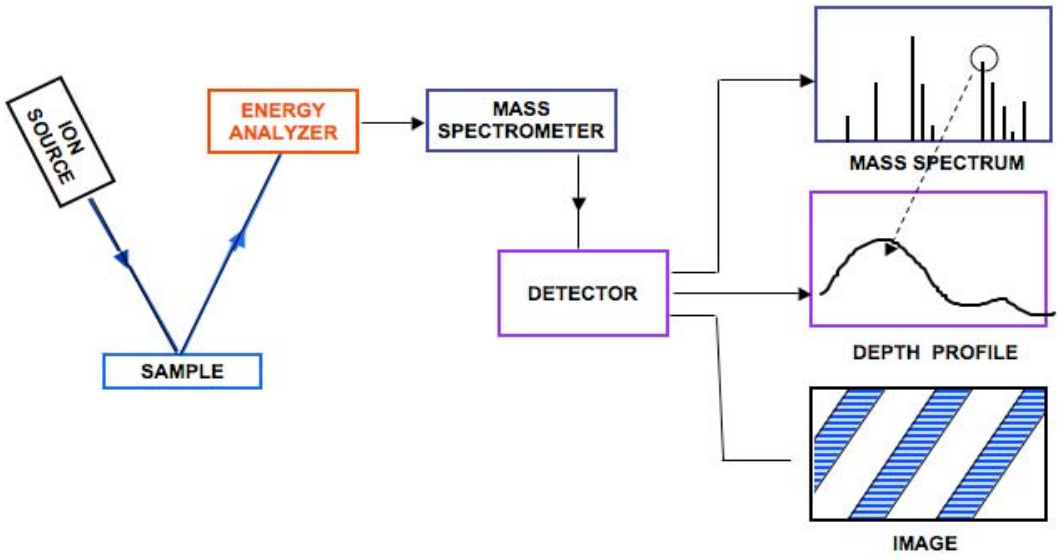

Figure 2.3: Block diagram of SIMS instrument.

Subsection 2.3.2: Secondary Ion Mass Spectrometry and Nuclear Forensics

Over the past several years, SIMS has been employed as a tool for nuclear forensics. The micro-beam capability of modern SIMS instruments allows investigators to analyze single particles without time consuming chemical

preparation, while maintaining precision comparable with other tools (Hou et al., 2005). However, SIMS instruments have limitations.

One limitation is the presence of molecular interferences. Often SIMS facilities will use an injection energy offset to eliminate some molecular background, at the cost of lowering collection efficiency. In nuclear forensics, an interference in the measurement of ^{236}U is ^{235}UH. Uranium-236 is a good indicator of a material's historical use because it is not a naturally occurring isotope. It is measurable by SIMS only after a correction based on the measured ratio of ^{238}U to ^{238}UH (Ranebo et al., 2010; Tamborini et al., 1998). Other interferences reported in swipes from nuclear facilities involve PbCO ions, which interferes with ^{236}U and other mass 236 species. These are problematic since swipes from facilities using lead shielding will always include lead isotopes. To overcome this limitation and analyze such samples, researchers removed uranium particles from the swipe and moved them to a blank carbon planchet (Esaka et al. 2007). Although this is one solution, it may not be sufficient in all situations, because extremely small particles may be impossible to move and the process is time consuming. Table 2.1 presents the mass resolution required to differentiate between atomic and molecular masses in several situations, including those mentioned in the literature. Many common instruments can achieve mass resolution of several thousand. It has been reported that some SIMS instruments can achieve 25,000 m/δm (Erdmann et al., 2000). But this increased mass resolution comes at the reduction of sensitivity, because of the use of an energy offset. The presence of molecular interferences, particularly in nuclear forensics

applications, points to the need for increased mass resolving power, while achieving high collection efficiency and thus high sensitivity.

Table 2.1: Required Mass Resolution for Cases of Interest in Nuclear Forensics

Nominal Mass	Species	Atomic/Molecular Mass	Required m/δm
234	^{234}U	234.040946	
	^{233}UH	234.047460	35928
	$^{206}Pb^{12}C^{16}O$	233.969364	3270
235	^{235}U	235.043923	
	^{234}UH	235.048771	48483
	$^{207}Pb^{12}C^{16}O$	234.970796	3214
239	^{239}Pu	239.052163	
	^{238}PuH	239.057385	45782
	^{238}UH	239.058608	37093
240	^{240}Pu	240.053814	
	^{239}PuH	240.059988	38876
18	^{18}O	17.991600	
	^{17}OH	18.006957	1172

SIMS measurements for nuclear forensics are currently conducted with either TOF systems or using magnetic sector mass spectrometers. SIMS-TOF systems are hindered by the duty cycle needed to ensure all species are collected before the introduction of new material, causing long analysis times. To shorten analysis time, material is often sputtered quickly without the collection of data to reach a new depth where data is then collected. This results in a loss of information. By limiting the mass range that can get to the TOF detector, the duty cycle can be improved because the pulse time would only need to pause for the difference in flight times of species of interest.

At this time, most nuclear forensics measurements are conducted with magnetic sector instruments. One limitation of these instruments is that they determine several masses simultaneously by using several detectors. These detectors must be cross-calibrated and only a limited number can be used over a narrow mass range. The limitation in mass range is overcome by peak hopping. Several groups use this technique, even within a few amu, to measure multiple masses (Ranebo et al., 2010; Lehto, 2002; Pajo et al., 2001). Peak switching results in lower collection efficiency because during the time one isotope, or set of isotopes is counted, ions resulting from other isotopes are not being collected. Thus, a mass spectrometer with a wide dynamic range could improve instrument sensitivity.

Subsection 2.3.3: An Idealized Instrument for Nuclear Forensic Analysis

In order to achieve the best possible results for the analysis of materials for nuclear forensics, no one tool can currently be used. As noted in Chap. 1 an idealized instrument would be automated and field deployable. To achieve this goal, sample preparation must be minimal. Many techniques currently used in nuclear forensics, such as the selection of non-lead containing particles mentioned in Sec. 2.3.2, are far from this goal. Further, ICP-MS techniques have also been employed in nuclear forensics and require careful, lengthy preparations. Additionally, for certain situations it has been shown that bulk measurements are not always sufficient for analysis and spatial information can be required (Desgranges et al., 2006). Current techniques used to measure uranium and plutonium isotope ratios use a correction factor to account for hydrides. This results in decreased precision and also requires user input and data analysis. In order to reduce user interaction, the need for sample

preparation requirement, and meet the need for spatial information, increases in mass resolution are needed. As noted in Table 2.1, mass resolution approaching 50,000 m/δm is necessary. While a few commercial instruments can achieve this, it is achieved with limited sensitivity.

The precision that must be achieved varies with the application and specific measurements. For oxygen isotope ratios, the observed variation in natural abundance is up to about 3%. From work by Pajo (2001) it can be estimated that isotope ratio precisions of up to 0.05% may be required to determine the origin of the material. Currently, experimental precisions of 0.1-0.25% have been achieved (Tamborini et al., 2002). For uranium enrichment, isotope ratio precisions of 0.5-2.0% have been achieved, which is sufficient to determine the material's use (Betti et al., 1999).

For uranium age measurements with small sample sizes, it has been noted by Mayer (2008) that using the current SIMS instruments, only highly enriched uranium can be aged. The half-life of the uranium isotopes, the efficiency of ion detection, and the size of the sample limit sensitivity and therefore the age determination. Figure 2.4 is adapted from Mayer (2008), and depicts the in-growth of ^{230}Th decay from ^{234}U. The figure was created assuming a 1-μm particle of uranium at the given enrichments and assuming ^{234}U will be enriched at the same rate as ^{235}U. The efficiencies were calculated assuming the detection of 10 ^{230}Th atoms. From Fig. 2.4, it can be determined that to achieve the dating of low-enriched uranium, efficiency of the system would need to approach 10%. Mayer (2008) estimates the current efficiency of SIMS as 0.5%. The low efficiency is due to source characteristics as

well as transmission through the spectrometer. To improve efficiency from the source, Sputtered Neutral Mass Spectrometry could be investigated to ionize more of the particles leaving the sample. The efficiency through the spectrometer can be improved by achieving high transmission and by detecting the entire sputtered beam. During peak switching only a part of the ion beam is detected at the same time, lowering efficiency by at least half. A spectrometer that detected the entire beam would at least double the efficiency, with additional gains if more than two species are detected.

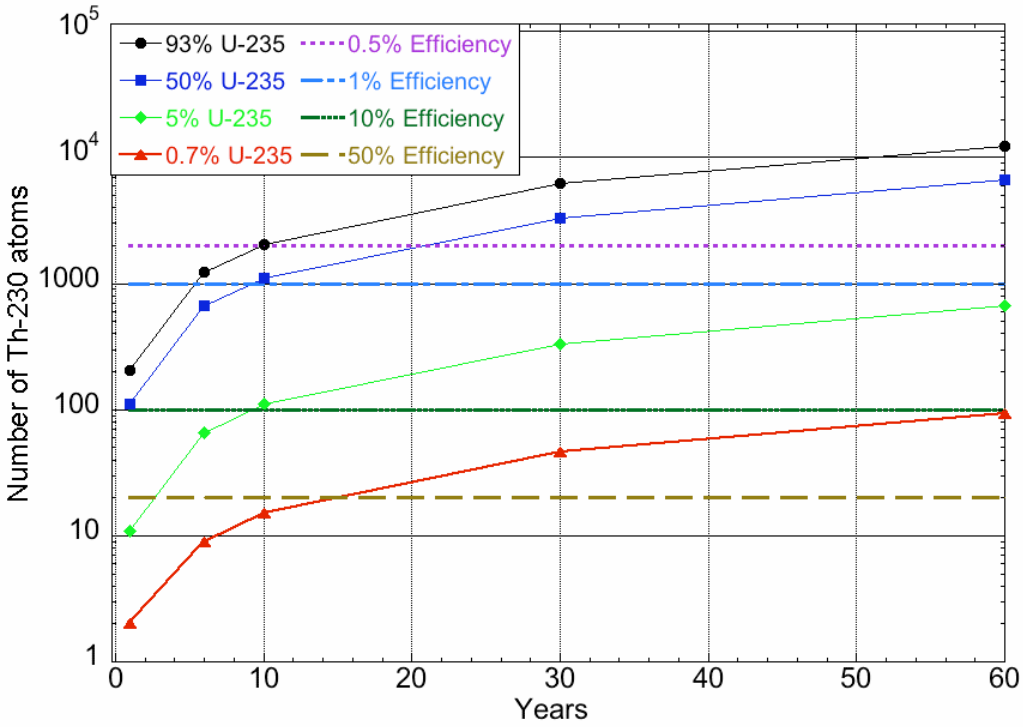

Figure 2.4: Number of ^{230}Th atoms produced in a ^{235}U sample, by different enrichment values. Efficiency values are presented for the number of atoms required in a sample to detect 10 atoms.

One method of collecting the entire sputtered beam is to switch to a TOF instrument. Currently sample measurement time is limited by sample preparation. However, if the previously mentioned gains in mass resolution, precision, and sensitivity were achieved and sample preparation time became small, the duty cycle of a time-of-flight spectrometer would become important. In work by Lehto (2002), uranium particles were completely sputtered in under 700 s, using a magnetic based technique and, therefore, constant sputtering. Using this value, Table 2.2 was constructed to demonstrate the effect of duty cycle on analysis time. A 20% duty cycle is common in commercial TOF instruments. For a single particle analysis, this duty cycle does not have a large impact on analysis time. However, if 100 particles are analyzed, to improve precision for instance, the analysis time increases from 1 day at 100% duty cycle to 3 days at 20% duty cycle. For the worst-case scenario of a post-detonation nuclear forensics case, time is critical, thus a spectrometer with a duty cycle as near to 100% as possible is desired.

Table 2.2: Effect of Duty Cycle on Analysis Time

Duty Cycle (%)	Analysis Time (hr) 1 particle	Analysis Time (hr) 10 particles	Analysis Time (hr) 100 particles
100	0.2	2	19
50	0.4	4	39
20	0.8	8	78
10	2	16	156
5	3	31	311
1	6	62	622
0.1	12	124	1244

Thus, an ideal TOF spectrometer would have a mass resolution near 50,000 m/δm, precision for measuring isotope ratios better than 0.05%, better than 50% efficiency at detection of atoms, and a duty cycle near 100%.

Section 2.4: Accelerator Mass Spectrometry and the Naval Research Laboratory's Trace Element Accelerator Mass Spectrometer

Accelerator mass spectrometry (AMS) is an ultra-sensitive technique used for the analysis of isotopes with a long half-life. The technique has found great success in radiocarbon dating, as well as contributing to other scientific arenas such as: archeology, geology, cosmochemistry, hydrology, biomedical sciences, and nuclear forensics. The sensitivity and isotopic resolution of this technique is achieved by the use of an accelerator that causes break-up of molecules in a gas-filled stripper canal or stripper foil, and because of the use of low-background nuclear detection techniques. Because AMS is only referred to here as part of the description of the system used, the reader is referred to Tuniz et al. and Gove for a more complete treatment of the technique (Tuniz et al., 1998; Gove, 1999).

Traditionally, AMS is a bulk sample technique. Most ion sources designed for AMS are not meant for surface analysis. A few systems have been designed which, like the Naval Research Laboratory Trace Element Mass Spectrometer (NRL-TEAMS), couple the surface analysis capabilities of a SIMS instrument with the isotopic sensitivity and accuracy of an AMS system (McDaniel et al. 1992; McDaniel et al. 1993; Ender et al. 1997a; Ender et al. 1997b; McKeegan et al. 2005; Knies et al. 2006). These hybrid SIMS-AMS instruments have been given various names in the literature: TEAMS, accelerator SIMS, and MegaSIMS. The applications have

likewise been varied. The University of North Texas instrument has been predominately used to determine trace contaminants in semi-conductors (Datar et al., 2000; McDaniel et al., 1998). The PSI/ETH instrument has been used for geology purposes, focusing on Beryllium, Osmium, and Platinum Group elements (Maden et al., 2001, 2004; Sie et al., 2002; Maden, 2003). It has also been used to measure tritium in the vessel walls of fusion reactors (Stan-Sion et al., 2002). The UCLA Mega-SIMS was specifically designed to analyze the oxygen isotope ratio of solar wind to high precision, as part of the NASA Genesis project, which seeks to understand the origin of the sun by analyzing the composition of the solar wind (McKeegan et al., 2005, 2009, 2010; Mao et al., 2006, 2008; Kallio et al., 2008).

The NRL-TEAMS facility includes the micro-beam primary column and secondary extraction optics of a Cameca IMS-6f SIMS instrument (Grabowski et al. 1997; Grabowski et al. 2000; Knies et al. 2004; Knies et al. 2006; Knies et al. 2007). The facility's AMS supplants the normal detector portion of the Cameca IMS-6f. The AMS system was designed for parallel mass analysis and has a unique injection magnet and an unusual detection magnet, which can be outfitted with an array of detectors, along a 1.5-m-long focal plane (Cetina et al., 2003). A representation of the instrument is presented in Fig. 2.4.

In addition to being bulk analysis instruments, most AMS systems, including the few SIMS-AMS instruments, do not have truly parallel mass capabilities over a broad range. In many systems a "bouncing" injection is employed (Fifield, 1996; Sie et al., 2002). This means the trace beam is analyzed for a significant amount of time, followed by a short measurement of the matrix beam, after which the cycle is

repeated. For bulk measurements, where the matrix beam is not changing in time, this provides a reasonable estimation. However, for the most precise data, and for situations such as near-surface analysis where the matrix beam may vary with time, parallel mass analysis may be preferred. Other systems, such as the MegaSIMS, have some parallel mass capability, but they are limited to a restricted mass range. In the case of the MegaSIMS, this limitation is $\Delta m/m \leq 30\%$, which, for example, allows transmission of all oxygen isotopes and hydrides (Mao et al., 2008).

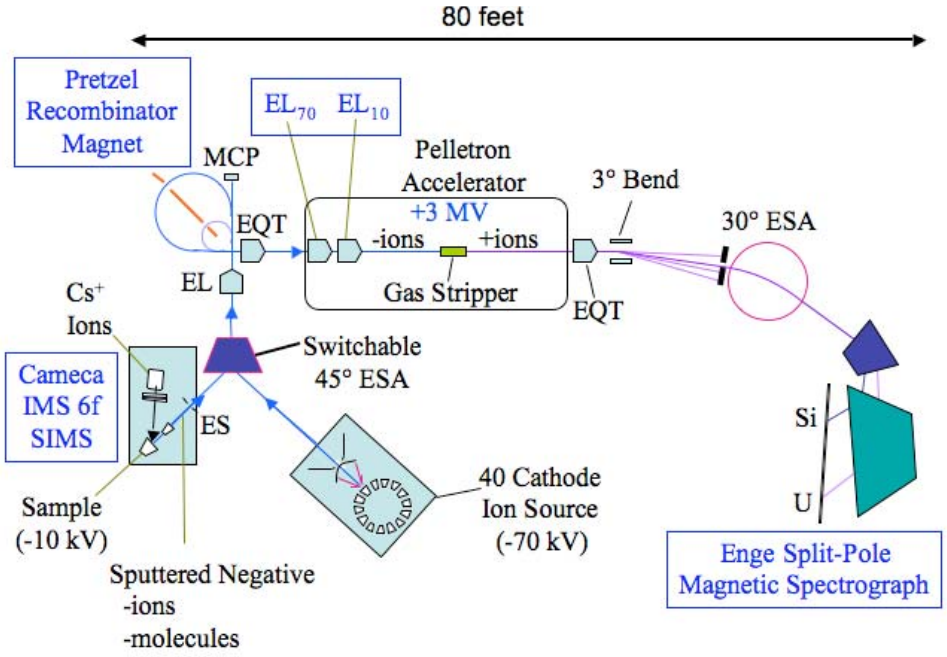

Figure 2.5: Representation of the NRL-TEAMS facility. ES is energy slit; ESA is electrostatic analyzer; EL is Einzel Lens; MCP is micro-channel plate; EQT is electrostatic quadrupole triplet.

The original design concept for the NRL-TEAMS was to apply truly parallel mass analysis capabilities to challenging materials problems. An initial study analyzed rare earth elements and was able to measure nanogram quantities, achieving limits of detection comparable with other competitive techniques (Cetina et al., 2007). Other experiments were conducted in preparation for the analysis of NASA GENESIS samples (Cetina et al., 2008, 2009, 2010). These results were achievable only by the use of parallel mass analysis, which is enabled by two unique features, the spectrograph detection magnet and the use of a Pretzel magnet for injection.

Section 2.5: The Pretzel Magnet

Enge originally described the Pretzel magnet in 1963 (Enge 1963). Magnetic systems used to deflect beams had previously been dispersive in ion momentum or had a limited range where they were non-dispersive. Enge's "achromatic magnet mirror" resolved this problem and created a magnet that could be used to deflect beams approximately 90^0 without adding dispersion over a wide range of momenta. This "achromatic magnetic mirror" was later termed a Pretzel magnet, due to the nearly 270^0 bend experienced by ions traveling through it. Enge's magnet design has been previously employed for the momentum analysis of electron beams (Rowe, 1970).

To enable the parallel mass analysis capability in the NRL-TEAMS, a Pretzel injection magnet was developed to allow for the injection of a wide mass range in parallel, while simultaneously providing the ability to remove unwanted species (Knies et al., 1997). A schematic of the Pretzel magnet with simulated ion trajectories is given in Fig. 2.5. The NRL system is capable of transmitting 1-200

amu when the ion energy is 40 keV and higher mass ranges at lower energy (Knies et al., 1997). Ion beams enter the Pretzel magnet at 42.3^0 and separate according to momentum along a 0.75-m-long focal plane. These ion beams are then recombined and leave the Pretzel magnet with the same optical characteristics with which they entered. By placing masks along its symmetry axis, only the momenta of interest are transmitted through the entire system. Because the NRL-TEAMS system is designed to be mono-energetic and utilize a single charge state, the momentum can be considered as mass, and such masks can be used as a mass filter. The magnetic field in a Pretzel magnet is inhomogeneous, but all references to field in this document are measured at the same location in the Pretzel magnet, at a penetration depth of approximately 0.8425 m, based on historical NRL-TEAMS calibrations.

The inherent Pretzel magnet properties can be exploited for TOF analysis (Knies et al., 1997; Demoranville et al., 2009; Demoranville et al., 2010). Mass filtering (MF) can be added to TOF analysis similarly to its use in TEAMS. Additionally, the Pretzel magnet's ability to separate individual masses, giving each a unique trajectory, and then recombining them into a single beam can be exploited to provide improved mass resolution.

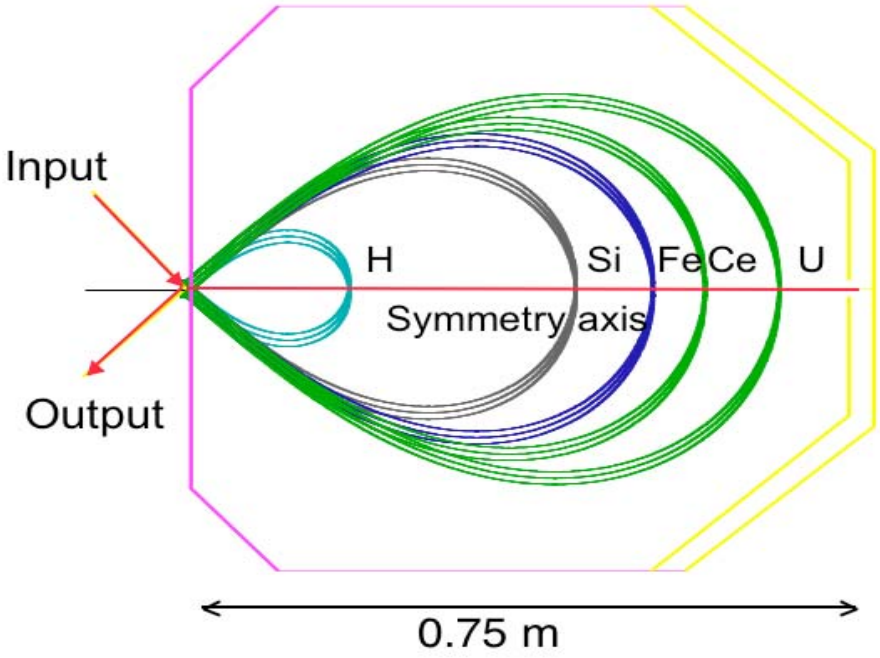

Figure 2.6: Illustration of simultaneous ion trajectories in the Pretzel magnet.

Section 2.6: The Mass Filtered, Time Dilated, Time-of-flight Concept

When particular regions of the TOF spectra are of interest, MF can be added to TOF analysis in a way analogous to its use in traditional AMS, namely, masses can be selectively analyzed or rejected using a mask in the Pretzel magnet. When masses are rejected, gaps are left in the TOF spectrum. If enough masses are rejected, it is possible to interleave spectra, so that more than one spectrum can be collected at the same time. This provides a tunable duty cycle, meaning that the instrument only needs to wait for the dwell time between species of interest before introducing the next burst of ions. By this method, the second pulse of ions can be injected to the system before the first is collected. This results in an increased duty cycle. The mask also minimizes noise by removing non-interesting species before they enter the rest of the spectrometer. If a particular mass has a significantly high count rate and is not of interest, such as a matrix beam not needed for normalization, it can be selectively

blocked before analysis. This will prevent flooding of the detector and lower dead time. This consideration may lead to better sensitivity than the current capability of standard TOF systems.

The concept of time dilated (TD) TOF utilizes an inherent property of the Pretzel magnet. That is, since all trajectories scale with momentum, essentially mass, and have the same geometric shape, species with higher mass have longer flight paths in the magnet. Traditional TOF spectrometers make use of the fact that heavy mass species take longer to fly than lighter ones when all ions are of the same energy and follow identical flight paths. In the Pretzel magnet, species of higher mass follow a longer flight path than those of a lower mass. These two factors, the ion velocity difference and the flight path difference, when taken together result in a mass-dependent time dilation of the transmitted ions. If time peaks are separated further in time, without a proportionate spread in the width of the peak, this time dilation will produce an increase in mass resolution over more traditional methods of TOF-MS.

Because of the needs of nuclear forensics, a TOF-MS system with higher duty cycles and improved mass resolution, particularly at low mass, relative to many mass spectrometric applications, e.g. amu < 500, would prove to be an effective and important tool. Additionally, advances in many fields have benefited from the advances made in TOF-MS, SIMS and AMS. Research is continually improving the state of the art in mass spectrometry through new and innovative approaches. MF-TD-TOF-MS is such an approach that merits investigation into its utility and potential benefits. The NRL-TEAMS offers an opportunity to investigate MF-TD-TOF-MS in

order to determine if it is a technique that may offer improvements to the state-of-the art of TOF-MS.

Chapter 3: Theoretical Background and Calculations

Several important equations in TOF-MS, and specifically Pretzel magnet based TOF-MS, can be derived based on the theoretical underpinnings of the technique. These equations can be used to predict the fundamental behavior of such a system if a few empirically determined parameters are known. Specifically, it is possible to compare traditional and Pretzel magnet based systems of similar physical footprints. Because the NRL-TEAMS system is limited in its ability to perform TOF experiments, as will be shown in Chap. 4, this theoretical analysis provides valuable insights that cannot be obtained using the NRL-TEAMS system alone.

Section 3.1: Theoretical Derivations

In TOF spectrometry, the TOF, t, is described by:

$$t = L\sqrt{\frac{m}{2E}}, \tag{3.1}$$

where L is path length, m is ion mass, and E is the ion kinetic energy. In typical TOF analysis, path length is constant so time is proportional to the square root of mass, $\sqrt{m}$, at constant energy. However, in a Pretzel magnet based TOF spectrometer, path length is dependent on the analyzed mass. Additionally, in a physical system, the time is delayed by the response of electronics. Thus, for a Pretzel magnet TOF system the total flight time as measured by the system t_{total} is the sum of the flight times in the Pretzel magnet, in the portion of the system outside the Pretzel magnet, and the time delay of the acquisition electronics, yielding:

$$t_{total} = L_P\sqrt{\frac{m}{2E}} + L_O\sqrt{\frac{m}{2E}} + t_{electronics}. \quad (3.2)$$

In a traditional system, it is trivial to determine the path length L_O, however in a Pretzel magnet based system the relationship is more complex. Because the geometric shape of the trajectories in the Pretzel magnet is independent of momenta, i.e. mass, it is possible to relate the length of the trajectory L_P to the maximum penetration depth by a proportionality constant K_P,

$$L_P = K_P * X_{max}, \quad (3.3)$$

where X_{max} is the maximum penetration along the symmetry axis of an ion in the Pretzel magnet. By combining Eq. 3.2 and 3.3 an expression for the total time t_{total} can be obtained

$$t_{total} = K_P X_{\max}\sqrt{\frac{m}{2E}} + L_O\sqrt{\frac{m}{2E}} + t_{electronics}. \quad (3.4)$$

In the original description of a Pretzel magnet, Enge developed the relationship:

$$X_{\max} = \left[\frac{(n+1)(mv)(1+\sin\alpha)}{qG_P}\right]^{\frac{1}{n+1}}, \quad (3.5)$$

where n is the field index, ν is velocity, α is the entrance angle, and q is the electric charge (Enge, 1963). The constant G_P describes the relationship of field to penetration of the magnet, according to

$$G_P = \frac{B_z}{X_z^n}, \quad (3.6)$$

where B_z is the field measured at location X_z. Combining Eqs. 3.5 and 3.6, and using the definition of kinetic energy it is possible to say:

$$X_{\max} = \left[\frac{(n+1)\sqrt{2mE}\,(1+\sin\alpha) X_{DTM}^{n}}{qB_{z,DTM}} \right]^{\frac{1}{n+1}}, \qquad (3.7)$$

where $B_{Z,DTM}$ is the field as measured at location X_{DTM}.

Combining Eq. 3.4 and 3.7 gives,

$$t_{total} = K_P \left[\frac{(n+1)\sqrt{2mE}\,(1+\sin\alpha) X_{DTM}^{n}}{qB_{z,DTM}} \right]^{\frac{1}{n+1}} \sqrt{\frac{m}{2E}} + L_O \sqrt{\frac{m}{2E}} + t_{electronics}. \qquad (3.8)$$

The NRL Pretzel magnet was designed to have n = 0.925 and $\alpha = 42.3^0$ (Knies et al. 1997). Additionally, historical measurements at NRL provide the location of the Digital Tesla Meter (DTM), the field measuring device, as 0.8425 m. Using these values in Eq. 3.8 and converting units such that m is in units of u, E is in units of keV, B is in units of Gauss, and X is in units of m, yields an expression for t_{total} in seconds:

$$t_{total} = 2.55X10^{-5} K_P \frac{m^{(n+2)/(2n+2)}}{B^{1/(n+1)} E^{n/(2n+2)}} + 2.2764X10^{-6} L_O \sqrt{\frac{m}{E}} + t_{electronics}. \qquad (3.9)$$

Equation 3.9 can be used to analyze the ability of a Pretzel magnet to improve mass resolution. Since mass resolution can be represented as:

$$\frac{m}{\delta m} = \frac{m}{\delta t} \bullet \frac{\delta t}{\delta m}, \qquad (3.10)$$

and m/δt is a measurable quantity equal to the mass of a given peak divided by its width in the time domain, it is possible to differentiate Eq. 3.9 to obtain δt/δm and compute m/δm. This leads to the following representation of mass resolution:

$$\frac{m}{\delta m} = \frac{m}{\delta t}\left(\frac{1.94X10^{-5} K_P}{B^{1/(n+1)} m^{n/(2n+2)} E^{n/(2n+2)}} + \frac{1.14X10^{-6} L_O}{\sqrt{Em}} \right). \qquad (3.11)$$

Given these parameters, a Pretzel magnet based system will have the highest mass resolution with low energy, low field, and large path lengths outside the Pretzel magnet.

Section 3.2: Analysis of Mass Resolution

To determine the potential benefits of the Pretzel magnet, a theoretical approach using Eq. 3.11 was used to compare the mass resolution of the current NRL Pretzel magnet with a linear TOF system, as described by the first and second terms in the sum of Eq. 3.11, respectively. The value of K_P has been determined experimentally as 2.3 ± 0.2, as will be presented in Sec. 6.2.

To constrain the analysis to a particular situation, a Pretzel magnet of the current size, that is a penetration depth of 0.75 m, was assumed. To compare the Pretzel magnet to a TOF instrument with a similar footprint, an L_O of 1.5 m was chosen. This is twice the penetration depth to account for a reflectron style instrument. For nuclear forensic applications, masses in the 240 u range are of interest. Traditionally the NRL TEAMS instrument has been used at a 9 keV secondary ion energy because this energy is needed to match with the acceptance of the accelerator system. However, most SIMS analysis is typically conducted at lower secondary ion energies and this has the benefit of improving mass resolution. A secondary ion energy of 1 keV was thus chosen for this exercise. While according to Eq. 3.11 it is beneficial to use as low a field as possible, the applied field must be sufficient to bend the heaviest isotope (i.e. most rigid momenta). For the chosen case of 240 u, this requires approximately 2300 G, as calculated from an empirical

calibration of the magnet. A pulse width of 5 ns, comparable to that reported by Katta and Chait (1991), was considered for the estimates generated.

A series of calculations was then conducted using Eq. 3.11. Figures 3.1-3.4 present the results of this analysis. In each, the blue, solid line is the mass resolution from the Pretzel magnet alone and the red, dashed line is the mass resolution of a reflectron TOF spectrometer of similar depth. In Fig. 3.1 the solid, vertical line represents the field below which 240 u cannot be bent through the magnet, at the given energy. In Fig. 3.2, the masses above the solid, vertical line cannot be bent through the magnet at the given field and energy. In Fig. 3.3, solid, vertical line represents the energy above which 240 u cannot be bent at the given field.

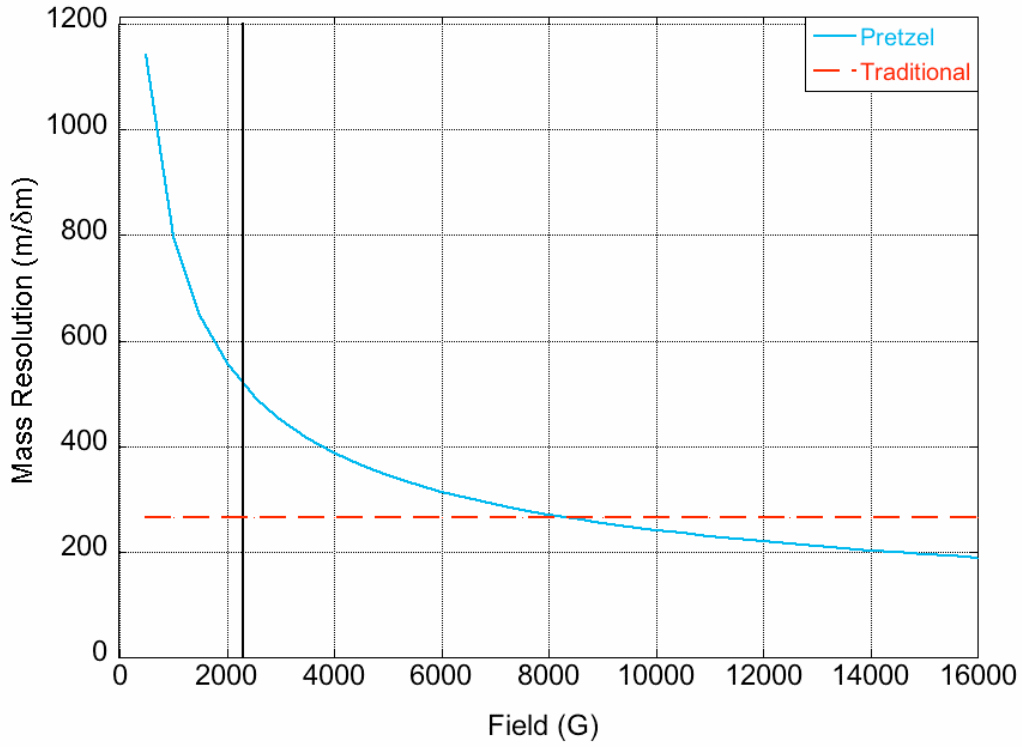

Figure 3.1: Mass resolution variation due to field (m = 240, E = 1 keV, L_O = 1.5m)

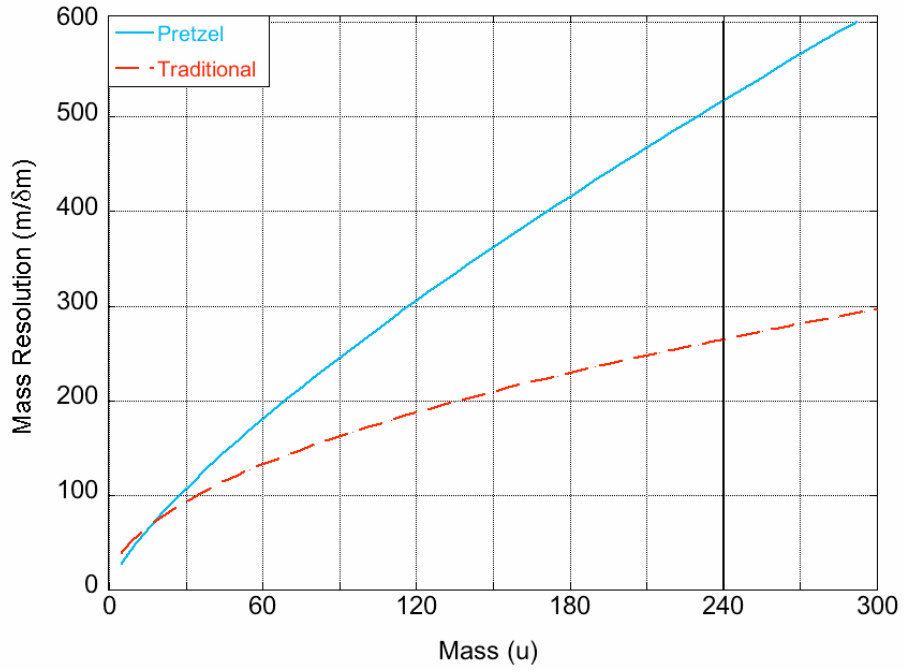

Figure 3.2: Mass resolution variation due to mass (B = 2300 G, E = 1 keV, L_O = 1.5 m)

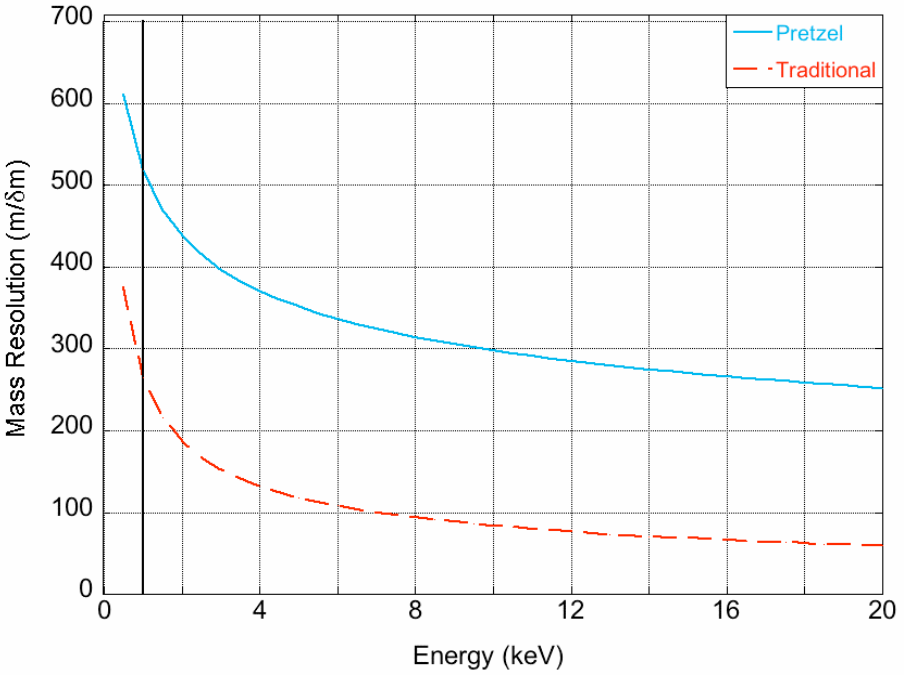

Figure 3.3: Mass resolution variation due to energy (B = 2300 G, m = 240, L_O = 1.5m)

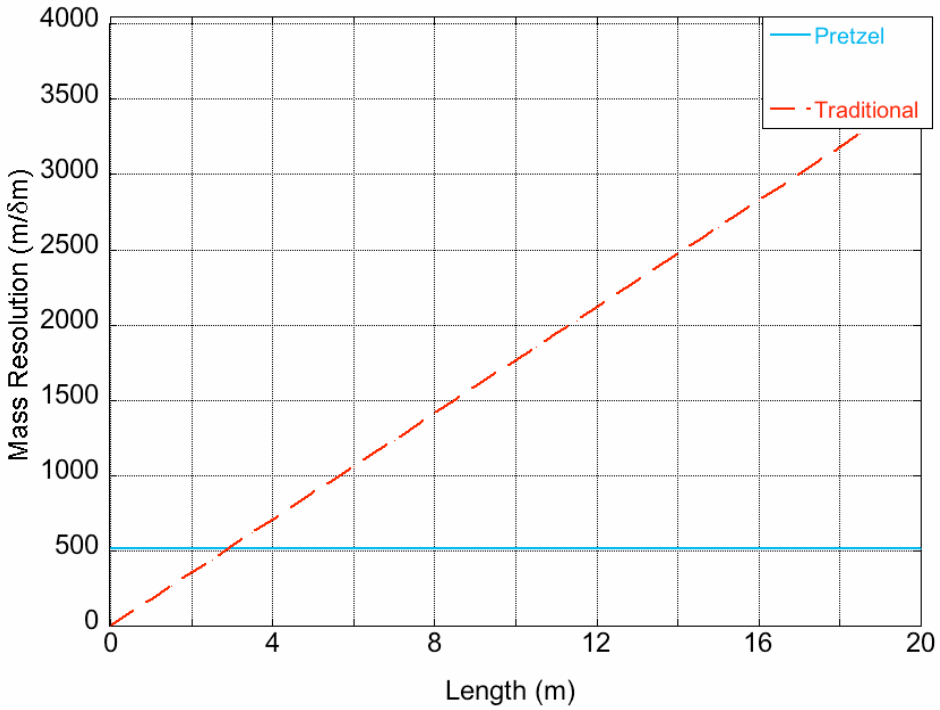

Figure 3.4: Mass resolution variation due to non-Pretzel spectrometer path length (B = 2300 G, m = 240, E = 1 keV)

It can be seen that in most cases under these starting conditions a Pretzel magnet based system is preferable to a traditional spectrometer. In fact only at fields above 8 kG, masses below 12u, or spectrometer lengths larger than 3 m, do the benefits of a traditional spectrometer overtake those offered by a Pretzel magnet based system.

As further evidence, a specific example can be selected. For E = 1 keV, m = 240 u, B = 2300 G, and L_O = 1.5 m, the mass resolution can be estimated at 10,350 m/δm for the magnet, and only about half of that for the reflectron system. A somewhat better mass resolution would need to be achieved in order to separate hydride molecules in the actinide region. However, the Pretzel magnet would still offer an advantage over a reflectron TOF system of a comparable depth.

Looking at the results more broadly, with the parameters used to create Fig. 3.1-3.4 a Pretzel magnet should offer increased mass resolution over a similar reflectron TOF spectrometer for $L_O < 3.0$ m, $B < 8800$ G, and $m > 19$ u. Based on empirical calibrations of the Pretzel magnet, fields higher than 8800 G would be needed only if heavier masses, that is > 8700 u, were to be analyzed. Such masses are not of interest for nuclear forensics, as actinides and their oxides will have mass < 300 u. In some cases the low-mass region, $m < 19$ u, would be of interest. For example it may be necessary to measure the oxygen isotope ratios to high precision for geo-location. In this case, the Pretzel magnet system could still offer an advantage since the field could be reduced and thus the mass resolution increased. Table 3.1 illustrates this scenario, and is calculated based on $E = 1$ keV, $L_O = 1.5$ m, $\delta t = 5$ ns. Mass 12 u was selected and can be bent with 600 G. Under this condition, higher masses will not be transmitted through the Pretzel magnet. Thus, the analysis of low masses sacrifices the detection of high mass species in order to improve the mass resolution of the low mass species. However, the mass resolution for $m = 12$ u is 2130 $m/\delta m$, which is almost double the mass resolution of a reflectron of similar length. Alternatively, if the higher field, 2,300 G, is used mass 240 can be simultaneously detected with high mass resolution with a slightly reduced mass resolution for mass 12, when compared to a reflectron of similar size.

These calculations assume a uniform energy. However, it is known the sputtering process does not produce a uniform energy, but rather an energy distribution. It has long been established that over a small range of energy distributions a reflectron-style TOF-MS can compensate for this energy distribution

(Karataev et al. 1972). A Pretzel magnet will have some energy-focusing properties, but whether it can completely compensate for the distribution is not currently understood. Thus, while this analysis provides some valuable insight into the capability of a Pretzel magnet based system, the analysis is not complete. If the Pretzel magnet does not have sufficient energy-focusing, it may still be possible to use this technique as part of a more complex system that includes energy-focusing or orthogonal accelerations techniques to reduce or eliminate the impact of energy straggle.

Table 3.1: Calculated Resolution for Selected Masses and Fields.

Mass (u)	Field (G)	Pretzel Mass Resolution (m/δm)	Reflectron Mass Resolution (m/δm)
12	600	2130	1185
12	2,300	1062	1185
240	2,300	10,350	5,298

Chapter 4: SIMION Modeling

SIMION is a software package commonly used to model ion trajectories in electrostatic and magnetic fields (Manura and Dahl, 2008). It was used to create a model of the pre-accelerator portion of the NRL-TEAMs facility, which was later used experimentally as the test bed for mass filtered, time dilated, time-of-flight mass spectrometry (MF-TD-TOF-MS). This model was used to estimate the overall mass resolution of the system, as well as aid in the determination of its mass resolution limiting elements and the impact of starting conditions.

Section 4.1: The SIMION software and the NRL-TEAMS model

In the SIMION software package each electrostatic or magnetic element in a given system can be created as a potential array. The electrostatic or magnetic field produced by the array is predicted by the software and used to calculate the likely trajectory of ions through a given system element. These potential arrays can be adjusted in the software to model a variety of conditions (e.g. different voltages or magnetic fields). In order to model a system, the potential arrays are placed in the software's "ion bench" in the proper orientations to one another, creating a model of the complete system.

Individual ions, or groups of ions, can be defined by a variety of starting conditions, including location (x,y,z), kinetic energy, initial angular direction, mass, charge, etc. These can be given single values or a variety of distributions. This starting ion, or group of ions, can then be "flown" through the system. The software package

predicts the trajectory through the components and final conditions of the ion (i.e. TOF, velocity, energy, etc.).

In order to create the model of the system, potential arrays for each of the elements were created. The design of the element is contained within a "Geometry" or "GEM" file. An example of such a file is given in App. G for the reflectron ion mirror that was used in the ion bench for the NRL-TEAMS system. These were then located within an ion bench. The location of each element was measured using the physical system, system design drawings, and schematics of the elements in the system. The coordinates and orientation of these elements are presented in Table 4.1.

Table 4.1: Location and Angles of Potential Arrays in SIMION Ion Bench Model.

Element	X	Y	Z	Azi-muthal	Ele-vation	Rotation
Immersion Lens	0	0	0	0	0	0
Transfer Lens	276.2	0	0	0	0	0
Contrast Aperture	422.2	0	0	90	0	0
Field Aperture	498.2	0	0	90	0	0
ESA	1316.53	135	0	-90	0	180
LE Slits	2085.44	624.1	0	90	0	-45
Einzel Lens	2261	799.2	0	0	45	0
Pretzel Magnet	2737.44	1276.10	-190	0	87.3	90
EQT	3238.97	669.85	0	-180	-39.6	-90
Reflectron	3615.4	214.83	-139.7	0	39.6	90

Section 4.2: Simulations of MF-TD-TOF-MS in the NRL-TEAMS model

To evaluate the magnitude of the benefits provided by MF-TD-TOF using the NRL Pretzel magnet and studying the mass resolution of the system and the TD effect, computer simulations modeled the low energy, or pre-accelerator, portion of the NRL-

TEAMS facility.

The mass resolutions of the simulations were determined using Eq. 3.11. In Sec. 6.2, the path length of the complete system outside the magnet will be experimentally determined to be 4.7 ± 0.1 m and K_P will be experimentally determined to be 2.3 ± 0.2. These values were used in the mass resolution calculations. The δt term was determined from the FWHM of the simulated data when fit with a gaussian curve, using the Kaleidagraph software package (Synergy Software, 2010). The error bars presented are ± 1σ, as calculated by the Kaleidagraph fitting algorithm and propagated through the calculations.

The simulations were conducted with a secondary ion extraction voltage of 9 keV. While this is a higher accelerating voltage than is typically used for TOF analysis, it is the voltage typically used at the NRL-TEAMS facility because of compatibility issues with the accelerator. A line sequence of starting origins from -0.1 mm to 0.1 mm in the vertical direction of the model was used to simulate the impact of variation in the location of ion origin in the vertical direction. Any horizontal variation, due to rastering of the beam, can be compensated by the dynamic transfer system of the Cameca instrument, so was not modeled. Because its lower magnetic rigidity allowed for wide-range scans of the Pretzel magnet, ^{28}Si was initially chosen for study. This isotope was "flown" through the low energy portion of the system, including the Pretzel magnet. The magnetic field was varied in order to produce a variety of different path lengths, and produce the time-dilation effect.

Other simulated parameters include a uniform distribution of initial kinetic energies from 0.5-10 eV. This is not an exact model of the true distribution of initial energies, but provides a measure of the influence of the initial energy (Wilson et al., 1989). The true ion energy distributions vary slightly by atomic mass, cluster size (e.g.

Si_1, Si_2, Si_3, etc.), matrix, primary ion voltage, and primary ion species. Data for the specific conditions used were not available, however, 14.5 keV Cs^+ primary ions used to sputter Si offer some insight. For negative Si atoms and clusters, there is a strong peak in emission energy at < 5 eV, with emission energies tailing to more than 100 eV for monoatomic Si negative ions (Gnaser, 2007). These tails decrease exponentially by three orders of magnitude. Additionally, the exponential tail in emission energy is more steep with increasing cluster size, reducing by 5 orders of magnitude to 20 eV for Si_5 clusters. This fact is commonly used in SIMS analysis to reduce the impact of molecules by employing an energy offset. Because of this steep decay in kinetic energy, it is likely that the chosen initial model condition, a uniform distribution of initial kinetic energies from 0.5-10 eV, provides a reasonable estimation of ion energies. The literature provides similar emission energy profiles for 14.5 keV Cs^+ on graphite (Gnaser, 2000).

Arithmetic sequences of direction angles from -90^0 to 90^0 in both the horizontal and vertical direction were also used. Again, emission angle is dependent on a number of factors, including the primary ion energy, angle of incidence, and species, as well as the matrix. The choice of an 180^0-wide emission angle distribution for the simulations is again a worst-case scenario and will therefore overestimate the width of arrival times. In fact, the literature suggests emission angles are significantly narrower for Cs^+ sputtered Si at 10 keV, with a range of approximately 40^0 and the peak emission angle and width depending on the incidence angle (Verdeil et al., 2008).

An additional simulation was conducted that used the energy data from Gnaser (2007) and the angular data from Verdiel et al. (2008). The distributions used are presented in Fig. 4.1. The simulation also utilized a uniform distribution of starting origins from -0.1 mm to 0.1 mm in the vertical direction of the model and 9 kV extraction voltage in order to more realistically simulate the initial starting conditions. This simulation was also used to determine the applicability of the more generalized, but more easily modeled uniform distribution of ion energy and emission angle.

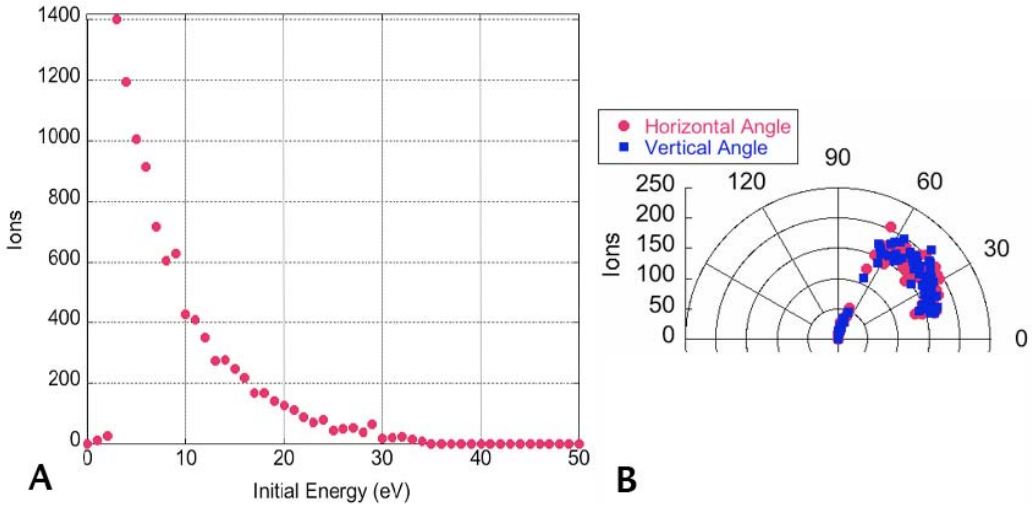

Figure 4.1: Initial energy and angular starting conditions for simulation. (a) Energy data based on 14.5 keV Cs^+ on Si from Gnaser (2007). (b) Angular data based on 10-keV Cs^+ on Si at a 30^0 incidence angle from the normal given in Verdeil et al. (2008).

The results of these two simulations are shown in Fig. 4.2 and display the expected trend of decreasing mass resolution with increasing field. Increasing field decreases path length and, therefore, decreases the TD effect. Additionally, the use of a uniform distribution of initial ion energy and angular distribution under-predicts the

mass resolution, when compared with the simulations based on measured data for sputtered ions under similar conditions to those expected at NRL-TEAMS. In both cases, however, the mass resolutions were insufficient to be useful as a functional instrument.

Due to the small discrepancy in mass resolution, the difficulty in running literature-based simulations, and the lack of literature data for many species of interest, particularly actinides, the uniform ion energy and angular distributions, which under-predict the mass resolution were used for further simulations. In this way the simulations could be compared more directly.

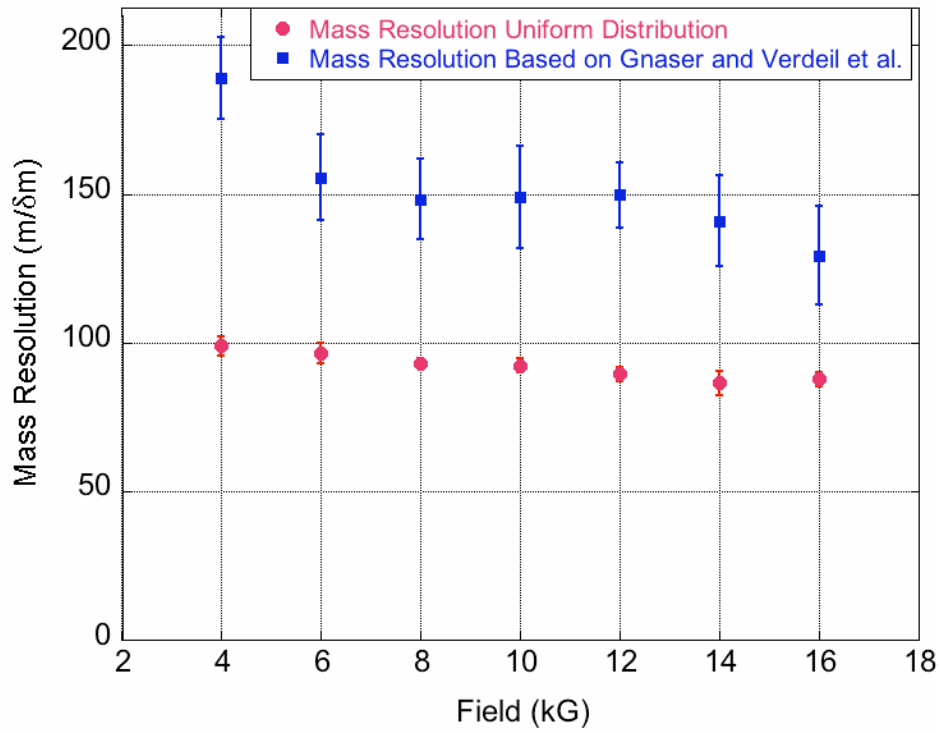

Figure 4.2: Mass resolution dependence on field for entire low energy system. Red circles are from simulation using a uniform distribution of initial energy and angles. Blue squares are from simulations based on the data from Gnaser (2007) for initial energy and Verdeil et al. (2008) for initial angular distribution.

In order to determine if the mass resolution was limited fundamentally or by some component of the NRL-TEAMS system, simulations were conducted with beam stops placed after different elements of the system and the mass resolution was calculated. These simulations were conducted using the uniform distribution of initial energy (0.5-10 eV), an arithmetic sequence of angles (-90^0 to 90^0), a line sequence of starting origins in the vertical direction (-0.1 mm to 0.1 mm), and 9 kV extraction voltage. For positions prior to the Pretzel magnet, there is no TD effect. Therefore, the term in Eq. 3.11, which is derived from the Pretzel magnet portion of the system, was omitted in mass resolution calculations. Mass resolution for these positions can therefore be calculated as:

$$\frac{m}{\delta m} = \frac{m}{\delta t}\left(\frac{1.1382X10^{-6}L_O}{\sqrt{Em}}\right). \tag{4.1}$$

The path lengths for non-Pretzel based portions of the system used in the calculations are presented in Table 4.2 and were derived from drawings of the system, with one exception. Because the total path length was experimentally determined (see Sec. 6.2), the experimentally determined value of 4.68 m was used, rather than the value of 4.63 m derived from construction drawings.

Table 4.2: Distance Outside the Pretzel Magnet to Various System Locations.

Physical Location	L_o (m)
Contrast Aperture	0.422
Low Energy Slits	2.269
Pretzel Entrance	3.265
Pretzel Exit	3.265
Reflectron	4.68

Figure 4.3 presents the results of these simulations on an image of the model. These simulations suggest the electrostatic analyzer (ESA) is the major limitation to mass resolution. This was not unexpected, as ESAs are known to be non-time-compensated, when used individually. Other TOF systems use various compensation schemes to correct for this (Verdeil et al., 2008). While the NRL system is not designed for TOF experiments and has inherent resolution limitations, it still enables some practical, experimental assessment of MF-TD-TOF-MS.

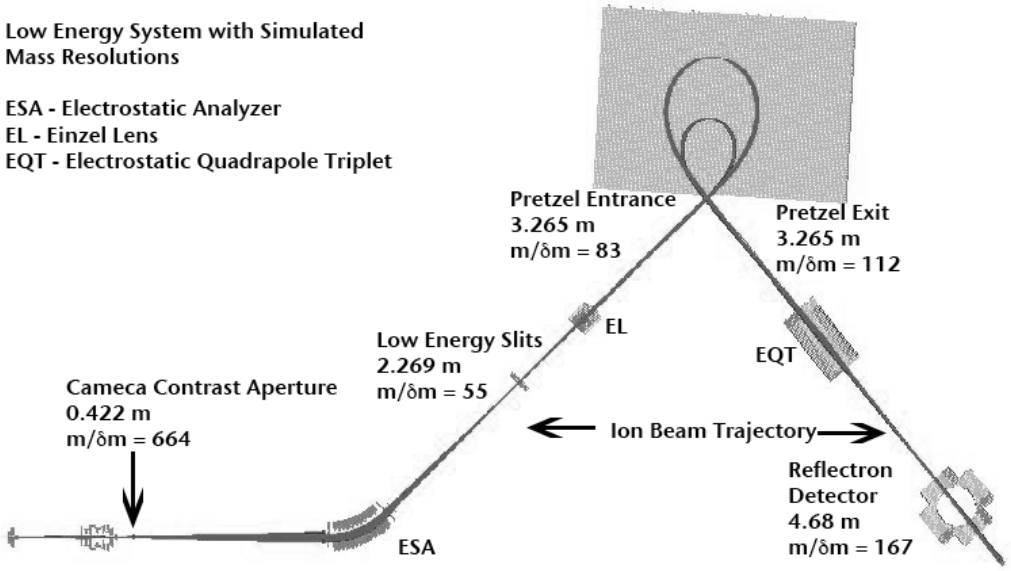

Figure 4.3: Mass resolution at various locations in the low energy system. Length measurements are the distance outside the Pretzel magnet from the source to the location.

Having established the general trend of mass resolution in relation to field behaves as predicted and the mass resolution in NRL system is limited by the ESA, simulations through the system depicted in Fig. 4.3 were conducted to determine the behavior of mass resolution at higher masses. Actinides, in particular, were of

interest. Isotopes and molecules modeled were ^{208}Pb, $^{208}Pb^{16}O$, ^{232}Th, ^{238}U, and $^{232}Th^{16}O$. These simulations were conducted under the same initial conditions as the previous study. As presented in Fig. 4.4, the mass resolution of these actinides and actinide surrogates again follow the anticipated pattern of a decrease with increased field. The mass resolution remains low, at approximately 90-100 m/δm.

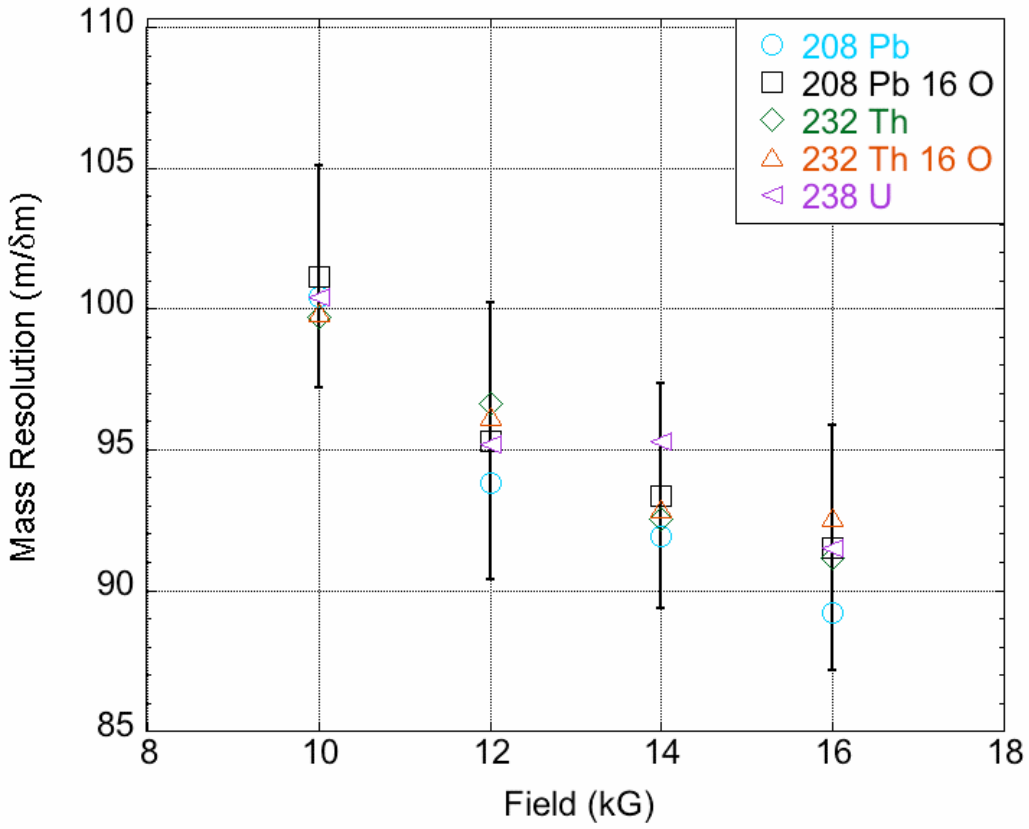

Figure 4.4: Mass resolution dependence on field for selected actinides and surrogates. Error bars are presented for $^{208}Pb^{16}O$ and are indicative of the error associated with each species.

In order to further explore the factors limiting mass resolution, several groups of ^{238}U ions were flown with different initial conditions at 10 kG. Each group

removed one or more of the factors leading to a difference in flight time, in order to help determine which initial parameters cause the greatest limitation to mass resolution. These parameters are presented in Table 4.3. When no source variation is listed the position was the origin, in the case of no angular distribution 0^0 was used, and for no initial KE distribution 0.5 eV was used.

Table 4.3: List of Parameters for Different Ion Groups.

Group Number	± 1 mm source position	-90^0 to 90^0 vertical angular distribution	-90^0 to 90^0 horizontal angular distribution	0.5-10eV initial KE
1	Yes	Yes	Yes	Yes
2	No	Yes	Yes	Yes
3	Yes	No	Yes	Yes
4	Yes	Yes	No	Yes
5	Yes	No	No	Yes
6	Yes	Yes	Yes	No

The mass resolutions resulting from these simulations are presented in Fig. 4.5. It can be determined from the plot that initial source position, within the limits modeled, and vertical angular distribution, that is angles coming into and out of the page when looking at Fig 4.3, provide little limitation to the mass resolution. Further, the use of the initial energy distribution contributes some limitations to mass resolution. It is the horizontal angular distribution, however, that is the greatest limiting factor to mass resolution.

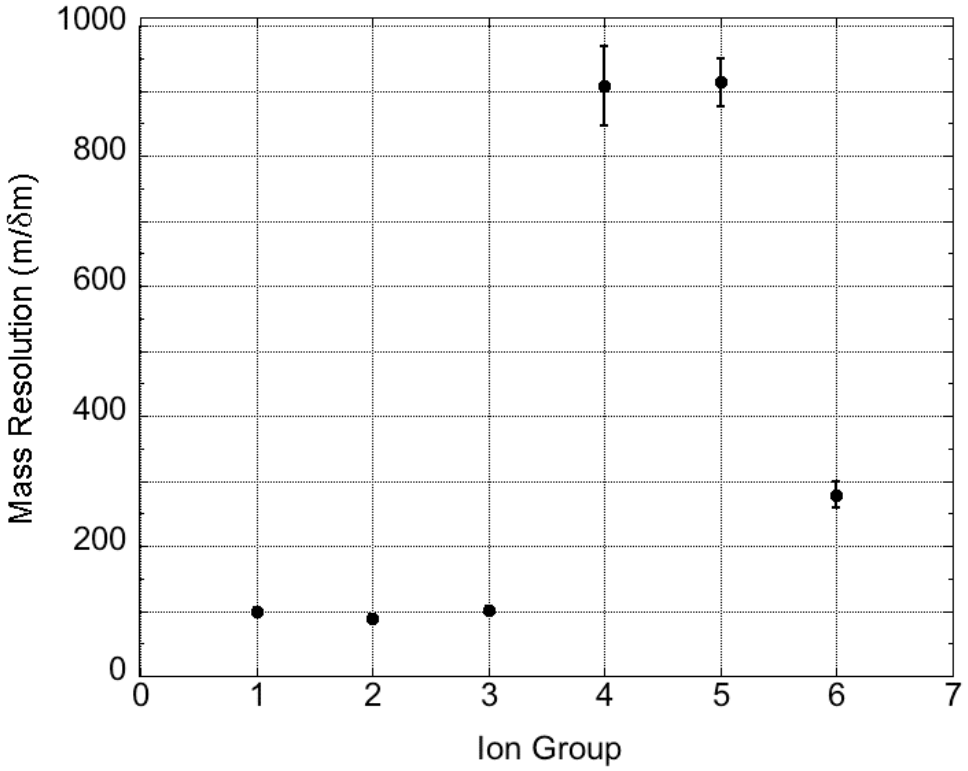

Figure 4.5: Presentation of mass resolution for various starting parameters. The ion groups are described in Table 4.3. For ion groups 1-3 the error bars are smaller than the data points.

This angular divergence is an overestimation of the physical system, based on literature values. To further determine if the poor mass resolution presented in Fig 4.2 was caused by the ESA, as suggested in Fig. 4.3, or by the horizontal angular divergence, as suggested in Fig. 4.5, the simulations conducted to create Fig. 4.3 were repeated but with no initial horizontal angular divergence. The results from these simulations are presented in Fig. 4.6 and show a consistent increase in mass resolution through the system. This suggests it is the angular divergence in conjunction with the ESA that cause the drop in mass resolution before and after the

ESA. When no horizontal angular divergence is modeled, the ESA does not cause a limit to mass resolution. Therefore, while the ESA does contribute to limiting the mass resolution if angular divergence is present, the angular divergence is a more important factor to control than changing the ESA.

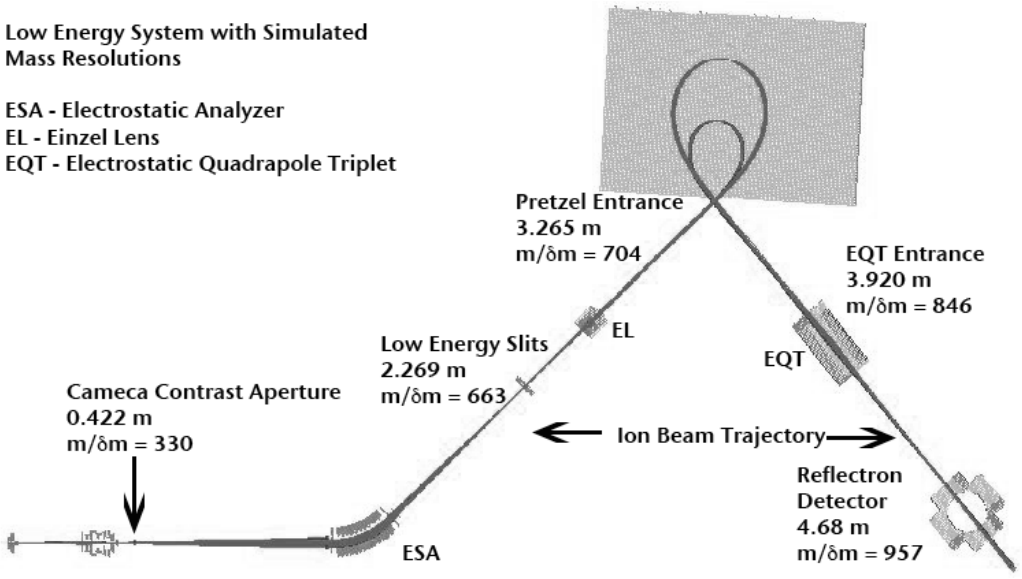

Figure 4.6: Mass resolution at various locations in the low energy system, simulated with no horizontal angular divergence. Length measurements are the distance outside the Pretzel magnet from the source to the location.

Although it is not possible to absolutely eliminate the effect of angular divergence, it is possible to limit the divergence by strategic positioning of apertures. Although these improvements were not implemented in the physical system, it was of interest to obtain an upper limit on the mass resolution of the system if they were implemented. Therefore, the actinide elements and surrogates for actinide elements were modeled in the system using no initial angular divergence, an initial beam height

of ± 1 mm, an initial beam width of 2 μm, and a uniform distribution of 0.5-10 eV initial kinetic energy at several fields. The addition of a small beam width was used because, although the dynamic transfer optics of the Cameca instrument account for a centering of the beam during rastering, it does not compensate for intrinsic beam width. The results are presented in Fig. 4.7.

The data presented in Fig. 4.7 further confirm the existence of a time dilation effect in the Pretzel magnet. Again, the overall trend shows a decrease in mass resolution with increasing field. The mass resolution for ^{238}U at 10 kG is slightly lower than that presented in Fig. 4.5 for ion group 5. However, the error bars are relatively large and could account for the slight difference. There also is a slight contribution from the initial beam width included in the simulations for Fig. 4.7, which was not used in Fig. 4.5 and would further limit the overall mass resolution.

For many routine applications of MS, mass resolutions of a few hundred m/δm are sufficient. However, commercial mass spectrometers are easily able to achieve this level of mass resolution and this system does not represent a significant improvement to the state of the art. In order to separate hydrides in the actinide region the mass resolution must approach 50,000, as presented in Table 2.1. Thus, as currently configured, the NRL system is not capable of resolving hydrides in the actinide region, which is important for nuclear forensic analysis. These simulations suggest it can, however, be used as a test bed for MF-TD-TOF-MS and could potentially be used for routine applications of MS, if the impact of angular distribution was negated. This may be addressed with the proper use of apertures or an isochronous ESA. The NRL-TEAMS system can be used to generate valuable experimental information to confirm the validity of system modeling and provide insight into the design of a true MF-TD-TOF-MS by suggesting what fundamental limitations may exist.

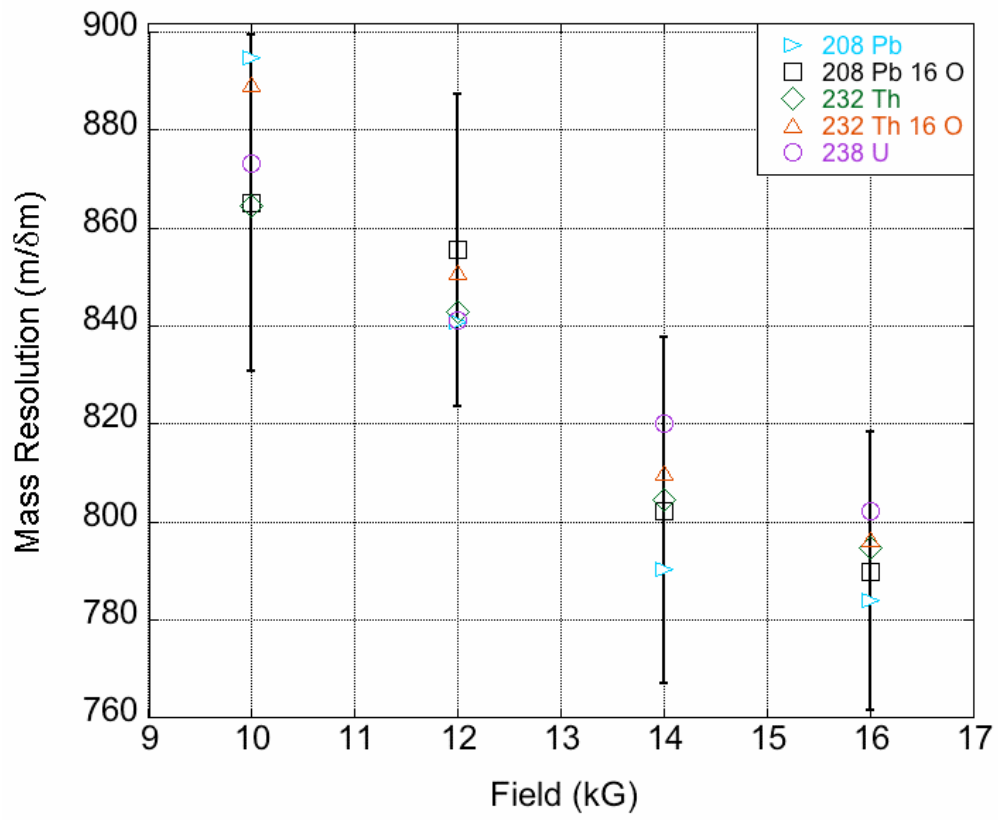

Figure 4.7: Mass resolution dependence on field for selected actinides and actinide surrogates, modeled with no initial angular distribution. Error bars are presented for $^{208}Pb^{16}O$ and are indicative of the error associated with each species.

Chapter 5: System Design & Improvements

The NRL-TEAMS facility, described in Sec. 2.4, was used to provide experimental confirmation of the theoretical and modeling results presented in Chap. 3 and 4. For this work, only the pre-accelerator portion of the system was used, the SIMION representation of which is presented in Fig. 4.3. This system is not an ideal system, as is discussed in Sec. 4.2, yet it can be used to evaluate the potential of an optimally designed TOF system. This chapter discusses the necessary system improvements required to perform TOF experiments. Several experiments regarding pulse generation are described. To provide counting detection in the pre-accelerator, a reflectron was added immediately prior to the accelerator to either electrostatically deflect the beam 90^0 into a microchannel plate detector or allow the beam to enter the accelerator. A microchannel plate detector was used to provide counting detection. These improvements, described in this chapter, allowed for a series of TOF-MS experiments, the results of which will be presented in Chap. 6.

Section 5.1: Beam Pulsing

The first generation of beam pulsing electronics used for experiments employed a waveform generator (HP 33120A) to produce a top-hat pulse shape. This waveform generator drove a high voltage switch (DEI PVM-4140) that switched between positive and negative high voltage power supplies. A number of different power supplies were attempted. In the final design, a Bertan Associates PMT 2kV-20A negative supply and a Glassman EW05120-115 positive supply were used.

The pulsing system was designed to pulse a set of deflectors after the electrostatic analyzer (ESA). The design was such that beam would be pulsed into the system at a high voltage and out at all other voltages. This pulsing scheme had several problems. First the waveform generator was not capable of producing short pulses. This is crucial to TOF measurements as the width of the analysis peak is partially limited by the width of the start pulse. A particularly long start pulse produces very wide analysis peaks, resulting in poor mass resolution. The waveform generator being used was limited to a 20% duty cycle. This produced analysis peaks limited to 2-μs wide out of a 10 μs spectrum. Thus at most 5 peaks would be able to be measured. Additionally, the pulsing system was difficult to tune to the proper voltage for pulse-in.

Therefore, a second generation of pulsing electronics was developed. A homemade circuit was designed by NRL electronics technician Claire Kennedy to provide an adjustable injection pulse width of 0-8.4 ms and an adjustable dwell time of 5.7 μs – 4.1 ms. Initially, this pulsing system was applied to the post-ESA deflection plates. The system was again difficult to tune to the proper voltage for pulse-in. Additionally, it was found that the beam, when in the pulsed-out position, could be deflected around the outside, rather than through the center, of the low energy slits following the deflector plates. This resulted in ghost peaks unrelated to the actual TOF spectrum. The voltage range for which the beam would be pulsed out of the center of the slits, but not beyond them was difficult to determine. At this location in the system, marked as LE slits in Fig. 4.3, the distance between the components is quite long, i.e. tens of centimeters, meaning that a small deflection

angle causes a large deflection downstream at the slit. Since the ESA is on the secondary, not the primary, ion column, sample was being consumed constantly although only a small portion was detected. This caused a significant loss in sensitivity. Therefore, the pulsing system was moved to deflector 4 of the Cameca 6f SIMS primary column, presented in Fig. 5.1. At this location the distance from the deflector to the slit is much shorter, i.e. < 10 cm, and the beam stop is a single aperture so that no beam could be deflected around it.

This second generation pulsing system produced reasonable results but was still not ideal. Because the deflector used was important to the tuning of the primary beam onto the sample, the voltage needed to transmit the beam varied from sample to sample. Additionally, it was found that the beam was difficult to tune to the proper pulse-in voltage. Further study of this second issue revealed that the pulse-in voltage suffered from ringing. This ringing caused the beam to be pulsed in and out several times over the course of the pulse-in time.

In determining the third generation of the pulsing system both the location and the pulse-in voltage problem were considered. The Cameca 6f SIMS primary column (Fig. 5.1) deflector 3a is before a different aperture but is earlier in the column. Additionally, this deflector is not optically important for the tuning of the beam and is maintained at ground. It is included in the primary column for use with an additional lens not present in the NRL configuration. Since using a primary beam deflector showed some success in the previous iteration, this lens was selected as the pulsing location.

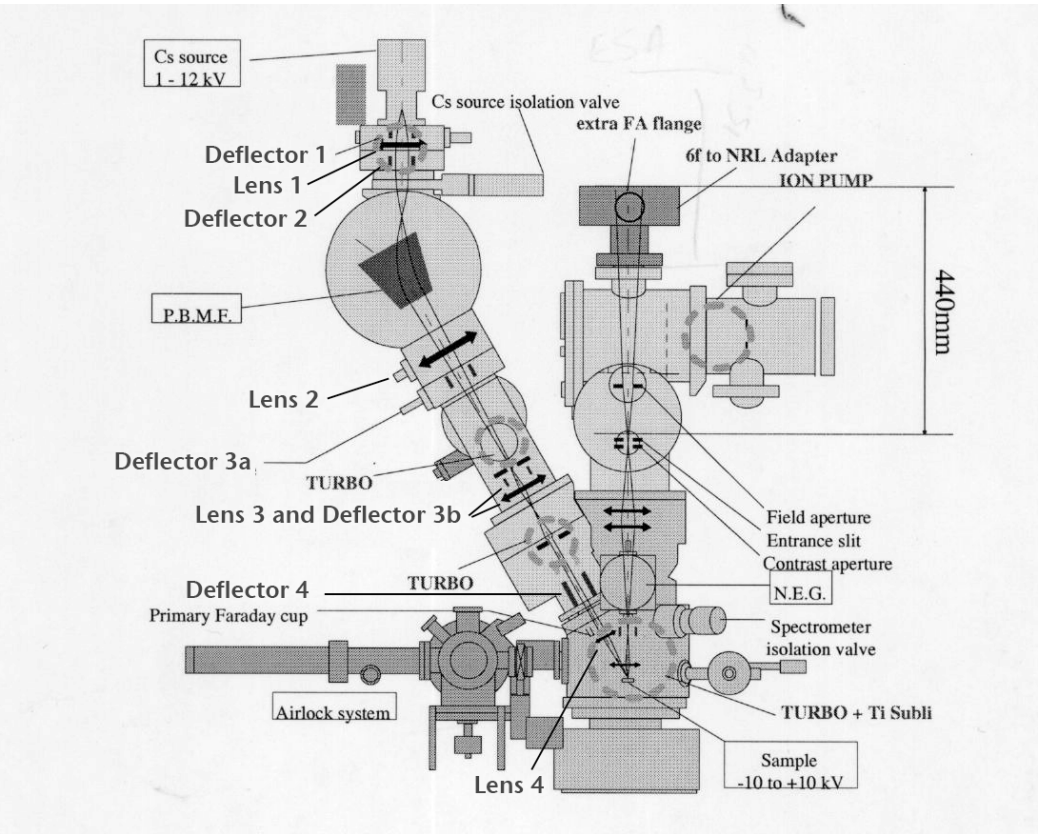

Figure 5.1: The primary and secondary beam column of the Cameca IMS6f. The primary column is the left set of optics, starting at the Cs source and ending at the sample. The secondary column is the right set of optics, starting at the sample and ending at the NRL adapter flange. Lenses are presented with double-headed arrows, deflectors with parallel lines. P.B.M.F. is the Primary Beam Mass Filter and N.E.G. is the Negative Electron Gun.

The second problem of being able to accurately maintain the pulse-out voltage was also investigated. It was found that most modern TOF instruments do not attempt to pulse in this manner. Instead, these systems pulse by sweeping the beam across a slit (Chait & Standing 1981; Rathmann et al. 1985; Katta & Chait 1991; Ma

et al. 1992; Piel et al. 1999). Therefore, a top-hat waveform was again applied to the high voltage switch, however, rather than attempting to reach the pulse-in voltage and maintain it, the top-hat was used to sweep the beam across an aperture in the primary column.

This third generation pulsing system is reliable and relatively easy to use. However, the counting system is triggered on the rising edge of the top-hat pulse, yet beam can pass on both the rising and falling edge of the pulse. As noted by Ma et al. (1992), the rising and falling edges can have slightly different rise and fall times. This results in two slightly different mass spectra, or the splitting of peaks. Ma also notes that if the rising and falling edges are not sufficiently separated, it can lead to overlap of spectra. This is true in the current configuration of the pulsing system. Thus the dwell time must remain high, e.g. at least twice the collection time of the spectrum. This significantly limits the duty cycle.

Although each described system was an improvement over the previous generation, it was possible to obtain experimental data using each of them, which will be presented in Chap. 6. As a reference for those experiments, Table 5.1 presents a summary of each of the generations of pulsing equipment used.

Future work should focus on creating a “box” pulsing system, such as those described in Katta & Chait (1991), Ma et. al (1992), and Piel et. al (1999). In such a system the beam is swept across the aperture in one direction, for instance the positive y direction, by the leading pulse, then pushed in the orthogonal (positive x) direction and allowed to return by the falling pulse to the original y position, then

returned to the original x position. The cycle would then repeat creating a second pulse.

Table 5.1: Summary of Pulsing Electronics Development

Generation	First	Second	Third
Pulse Generator	Waveform generator (HP 33120A)	Homemade Pulse Circuit	Waveform generator (HP 33120A)
Pulse Characteristic	Top Hat 20-50 % Duty Cycle	Top Hat Pulse: 0-8.4 ms Dwell: 5.7 μs – 3.1 ms	Top Hat
Pulse In/Out	In: High V Out: Low V	In: High V Out: Low V	In: Transition between High and Low V Out: High and Low V
Pulse Location	Post-ESA deflectors	Final primary beam deflector (L4)	Unused primary beam deflector (L3a)

Section 5.2: Reflectron Ion Mirror Design

The majority of the research performed at the NRL-TEAMS facility involves utilizing the complete accelerator system, while this work was performed completely without the accelerator. It was therefore necessary to design a detection system that could be used for TOF research, while at the same time maintaining the capability of using the accelerator for other measurements.

The TOF system requires the use of a counting detector, such as a micro-channel plate detector (MCP). An MCP detector is composed of an array of glass micro-tubes, or channels, arranged at an angle to the impinging beam of ions or electrons. When held at high voltage, the charged particles impacting on the MCP

create a cascade of electrons that are accelerated through the channels to a collection plate. This cascade amplifies the incoming signal. Usually the channel plates are used in multiple, either as a chevron - two arrays - or as a z-stack - three arrays, to further improve the gain. These detectors have a dead time at high count rates, because of the time needed to recharge the electrons liberated in the cascade. An MCP is, therefore, limited to a count rate of some MHz, translating to approximately 1 pA.

Frequently, for other TEAMS research, beams of higher current are employed. These high currents can cause damage to MCPs, which also cannot provide reliable count rates at that level. The TEAMS system therefore employs a Faraday cup detector as a tool to determine the beam current being injected into the accelerator. There are times, however, when minor, trace beams are injected into the accelerator. Often, these constituents are so minor, they are below the limit of detection of the Faraday cup. The NRL-TEAMS research group has wanted the ability to detect these beams prior to acceleration as a diagnostic tool to aid in the tuning of the NRL-TEAMS system.

It was decided that the TOF detection system should be designed so both needs were filled. The goal of the design was to have a system that would allow beam to pass through for typical use of the NRL-TEAMS, but enable a fast switch into a counting detector to determine the count rate of trace species or to employ as a TOF detector. A reflectron ion mirror is a suitable choice for this purpose.

In an ion mirror, when a voltage equal to the voltage of the ion beam is applied, it has the property of bending an ion beam entering it at twice the entrance

angle. Thus a beam entering at 45^0 to the mirror will be bent by 90^0. Further, under these conditions the optical properties of the beam are conserved. Thus, the use of an ion mirror in the NRL-TEAMS system allows the analysis beam to be bent off-axis into an MCP detector when a voltage is applied to the mirror or to enter the Faraday cup or remainder of the system when no voltage is applied.

In order to test the design prior to implementation, SIMION was used to create a number of models of the system to optimize the design. All the simulations performed in Chap. 4 utilized the final reflectron design as it was installed. This SIMION model was used to determine if the reflectron operated properly. It was also used to ensure that the reflectron plates fit inside the required vacuum chamber without degradation of operation. Because the chamber is grounded and components were to be in close proximity it was possible the chamber could alter the electro-potential field lines.

After several iterations of design, the reflectron shown in Fig. 5.2 was constructed. Oval plates were necessary to fit into the vacuum chamber, an eight-inch, six-way cross, as can be seen in the engineering drawing presented in Fig. 5.3. It was also determined a “halo” electrode was necessary. This electrode is the middle plate in Fig. 5.2. It is hollow through the center. When the rear electrode is held at the voltage required to bend the beam, the halo electrode is held at half that voltage, while the front electrode is held at ground.

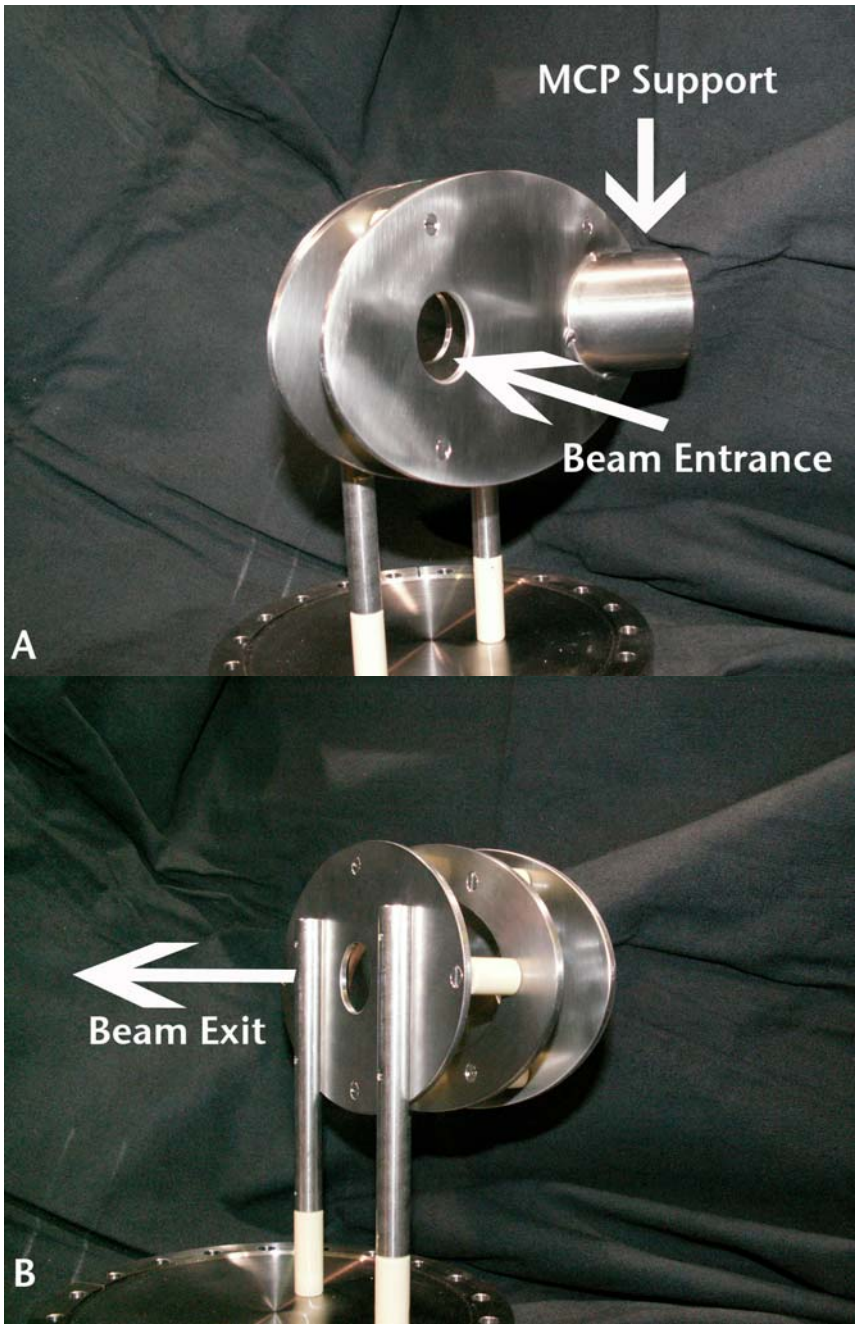

Figure 5.2: Reflectron ion mirror (a) front view and (b) rear view. The ion beam enters in (a) as indicated by the arrow, passing straight through at 0 V, and bending 90^0 at voltage. Structure on right is a support for the MCP. In (b) the beam leaves through the visible hole at 0 V. The middle ring visible in both (a) and (b) is the halo electrode.

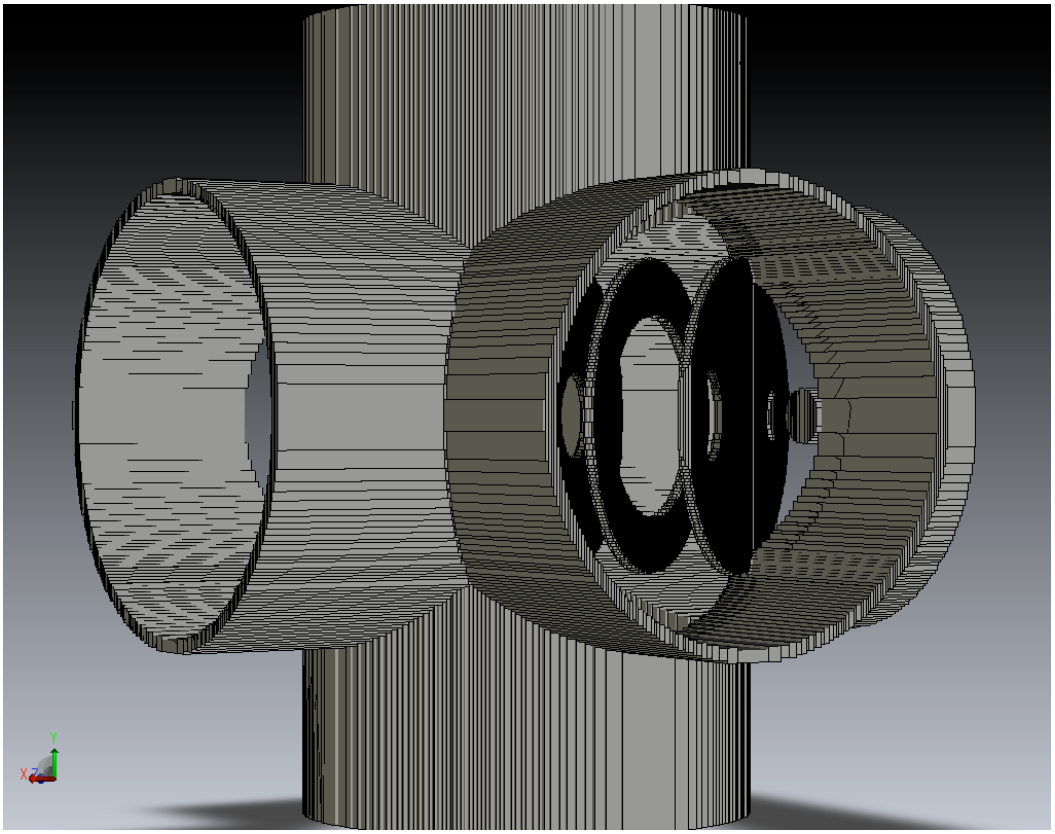

Figure 5. 3: Engineering drawing of the reflectron in an 8-inch, six-way cross.

By including a halo electrode the potential field shape is improved, i.e. the equipotential lines are held parallel to the electrode plates rather than having a bend to them. This is illustrated in Fig. 5.4. Figure 5.4a is the SIMION representation of the reflectron with no halo electrode; the front plate is at ground, the rear plate at -9 kV. The equipotential lines have an obvious bend to them throughout the reflectron. Equipotential lines that are parallel to the plates are crucial for proper operation of the reflectron because the ions travel perpendicular to the field potential, therefore, any curvature in the equipotential lines can cause aberrations in the beam. Figure 5.4b presents the SIMION model of the reflectron with the halo electrode included; the front plate is at ground, the halo is at -4.5 kV and the rear plate is at -9 kV. In Fig.

5.4b, the equipotential lines are significantly more parallel to the electrodes, which will cause significantly fewer aberrations. There is still some curvature to the field lines near the apertures in the electrode, however the potential field is significantly improved.

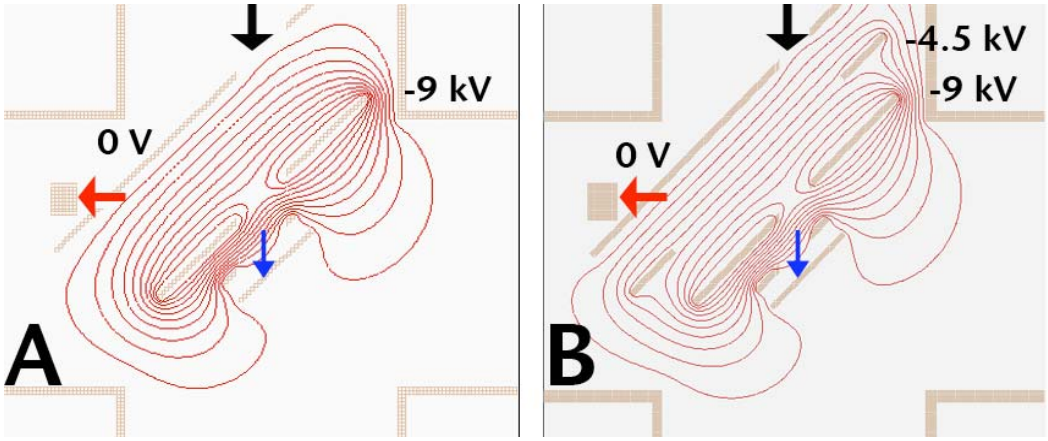

Figure 5.4: SIMION representation of the reflectron with field potentials (a) the reflectron with no halo electrode (b) the reflectron with halo electrode. The beam direction is presented with arrows. Black arrows denote the incoming beam, red arrows denote the bent beam (reflectron at voltage), and blue arrows denote the beam traveling through the reflectron (reflectron at ground). The voltages applied to the electrodes to create the field potentials are labeled. The electrically suppressed faraday cup is comprised of the two non-labeled electrodes, which are at ground for this diagram.

After installation, the reflectron was tested. During its initial use it appeared that the MCP, a Photonis 30227 chevron, was not responding to the beam at the expected level. It is not possible to measure current in the Faraday cup prior to the

Pretzel magnet while operating in TOF mode. However, using the total current at that cup in DC mode (i.e. no TOF pulsing), and the estimated pulse width and dwell times, it is possible to estimate the anticipated count rate.

Initial experiments, using the second generation pulsing system described in Sec. 5.1, did not allow for routine switching between TOF mode and DC mode. Thus a direct measurement of the total current in the pre-Pretzel magnet Faraday cup was not possible. It is possible, however, to estimate this current using the primary beam current and historical data. From this estimation, an order of magnitude comparison of the data can be made. For example, data taken with similar settings in DC mode suggest that approximately 50 na Cs^+ primary beam will produce approximately 500 pA total current. Using a 500 pA total beam, pulsed with a 100 ns pulse width and 76 μs dwell time, it is possible to estimate a 3.9 MHz average count rate. With the system producing 50 na Cs^+ primary beam and pulsing with a 100 ns pulse width and 76 μs dwell time, count rates were measured at approximately 4 kHz. Thus, the estimate that a 50 na Cs^+ primary beam will produce a 3.9 MHz average count rate provides evidence that the detection system was not working properly given the resultant beam current that was several orders of magnitude too low.

It was hypothesized that the reduced count rate could have been due to the beam being larger or more divergent than anticipated. Thus, the support tube for the MCP on the reflectron may have been cutting the beam. In order to test this hypothesis, the instrument was retuned to change beam divergence and size, yet the count rate could not be raised. This suggested that tuning was not, in fact, the factor limiting the count rate.

To further test the hypothesis that the reflectron was the limiting factor, an alternative detection scheme was devised. The reflectron was removed from the system and instead a linear positioning feedthrough was used. The MCP was mounted on the feedthrough so when it was fully extended the MCP was located at the center of the beamline, yet could be removed from the beamline so that the cup could also be inserted. This still allows for the operation of the NRL-TEAMS system in its normal configuration and enables the TOF or trace beam detection. It is not, however, as easily employed as the reflectron system would have been.

Unfortunately, data taken just before the reflectron was removed suggested the MCP may have been damaged. The pulse shape of the signal was not clean, and signs of breakdown between the MCP plates were evident. When it was removed the MCP showed no visible signs of damage, but it was, nonetheless, replaced. Because both the MCP and the reflectron were replaced, the determination of the source of the original low count rate is difficult.

To test the linear positioning feedthrough system, the third generation pulsing system, summarized in Table 5.1, was used. This pulsing system allowed for quick changes between DC and TOF mode, so that more direct comparisons of the data could be made. The beam was measured in the pre-Pretzel magnet Faraday cup and on the MCP. A mask that permitted transmission of 1 amu was inserted into the Pretzel magnet. The count rate from various graphite beam currents at two fields is presented in Fig. 5.5. Varying Lens 1 in the primary column (see Fig. 5.1) produced the differences in beam current.

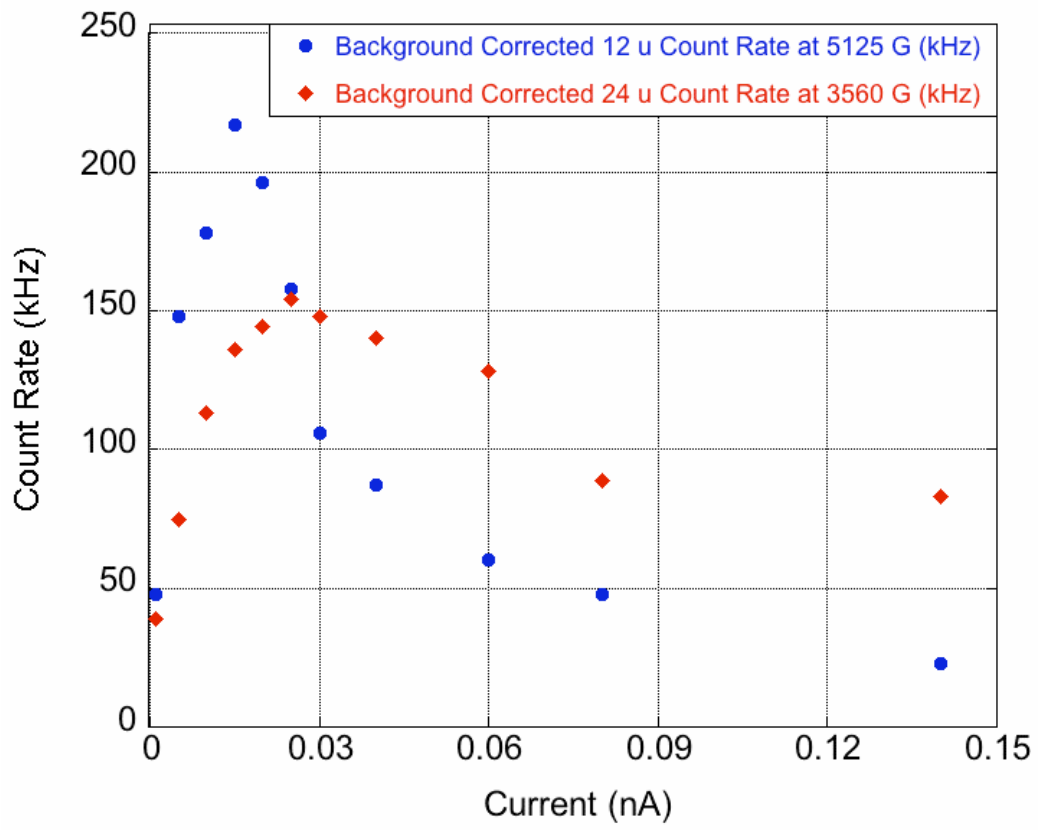

Figure 5.5: Count rate for given currents at mass 12 and 24 u. Blue circles are the count rate in kHz for mass 12 u transmitted at 5125 G. Red diamonds are the count rate in kHz for mass 24 u transmitted at 3560 G.

An examination of Fig. 5.5 shows higher count rates, by almost two orders of magnitude, than were obtained using the reflectron. Other experiments using the linear positioning feedthrough produced count rates of up to 700 kHz, which approaches the order of magnitude of the estimated count rates. This suggests the reflectron was not properly transmitting the entire beam to the MCP, but could also indicate an improperly functioning MCP.

Figure 5.5 also provides valuable insight into the MCP operation. At very low current, the count rate appears to scale linearly with current. However, as current is increased, the count rate loses linearity and, in fact, begins to decrease. It is possible to explain this trend by considering how beam arrives at the MCP. Prior to this, it has been claimed that the average count rate, that is the measured count rate averaged over the entire time of measurement, is an accurate reflection of the count rate experienced by the MCP. However, when looking at a single amu, all ions arrive at approximately the same time. These counts are then averaged over the entire collection period, in this case 1 s. This gives the appearance of a lower average count rate. However, when beam arrives at the MCP it instantaneously experiences a count rate analogous to a DC beam. As previously mentioned, MCPs are limited to count rates in the tens of MHz range. Thus, at low currents, the response is linear. But as current is raised, the instantaneous count rate exceeds the limit of the MCP and there is significant dead time, causing lower count rates.

In Fig. 5.5 linearity of the graphite beam count rate is maintained until approximately 0.015 nA, corresponding to an instantaneous count rate of 94 MHz. Functionally, the instantaneous count rate at the MCP is lower than this however, because the 0.015 nA is measured before the Pretzel magnet and represents the total beam. In this experiment, the beam is mass filtered to approximately 1 amu. This means the transmitted beam will be significantly less than the total beam.

This difference in measured beam current and transmitted beam also explains the difference in the peak location between the two masses observed in Fig. 5.5. Prior experience with the tuning of the Pretzel magnet has shown that, of the total current

from graphite, approximately half is from mass 12 u and a quarter is from mass 24 u. Thus the maximum MCP count rate is reached at higher currents for the 24 u beam than for the 12 u beam.

Although this realization may explain part of the deficiency in expected count rate in the reflectron, it cannot completely account for the deficiency. Higher count rates were found using the linear feedthrough detection scheme than using the reflectron. This suggests that, in fact, the reflectron was not working properly and that beam was in fact being cut somehow by the reflectron. Several possible explanations exist. First, the reflectron as constructed and installed could have slight variations in spacing and angle, which could cause differences in the flight path to the MCP. Related to this is the fact the beam enters and exits the Pretzel magnet at the proper theoretical angle in the SIMION model. In practice, the NRL system has no capability of ensuring this is true. There are many deflection plates that can correct for improper deflection of the ion beam. It is possible that beam enters the reflectron at a non-45^0 angle, which can affect the flight path through the reflectron. These alternate paths can cause the beam to be cut on several apertures in the reflectron. Additionally, as was explained in Sec. 4.2, the initial conditions for the SIMION model are poorly constrained. If the beam is in fact larger than modeled, it could be cut on the beam tube leading to the MCP.

To partially determine the impact these effects could have on the performance of the reflectron, further SIMION simulations were conducted. These simulations looked at the effect of the reflectron on an ion beam entering it at exactly 45^0 and with no angular dispersion. An F shape for the beam was employed, as shown in Fig.

5.6. This shape is frequently used in ion optical calculations as it displays the effects the optics have on beam shape. For these simulations only the reflectron was used. These simulations, presented in Fig. 5.6, reveal that the reflectron causes a slight distortion in the beam, particularly in the vertical direction.

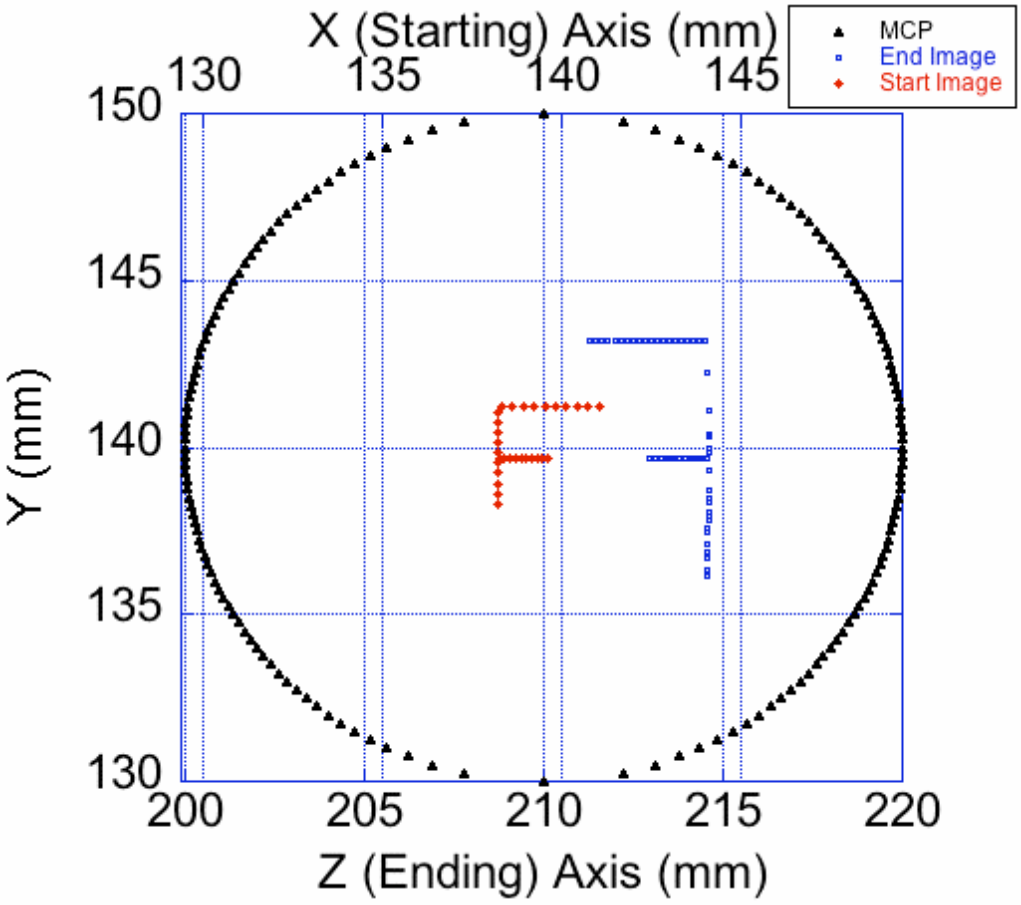

Figure 5.6: Graph depicting the starting ion image and final ion image through the reflectron ion mirror and its centering on the MCP. Red diamonds represent the starting position of ions in the simulation on the x axis, blue squares represent the end position of the ions on the z axis, and black triangles represent the area of the MCP on the z axis. The shift from the x to z axis reflects the 90^0 bend through the reflectron. Units are mm.

This distortion is due to the potential lines not being perfectly parallel to the plates and therefore perpendicular to the beam, as presented in Fig. 5.7a. The slight aberrations in the beam can be corrected in the simulations by adding a grounded grid to the front and rear plates of the reflectron. This smooths the potential lines and removes the aberrations, as shown in Fig. 5.7b. If the aberrations were limiting the performance of the reflectron, such grids could be employed on the physical reflectron. However, using grids in a physical system can reduce transmission as some ions will impact on the grid. This is not the case in the simulation, as they are transparent.

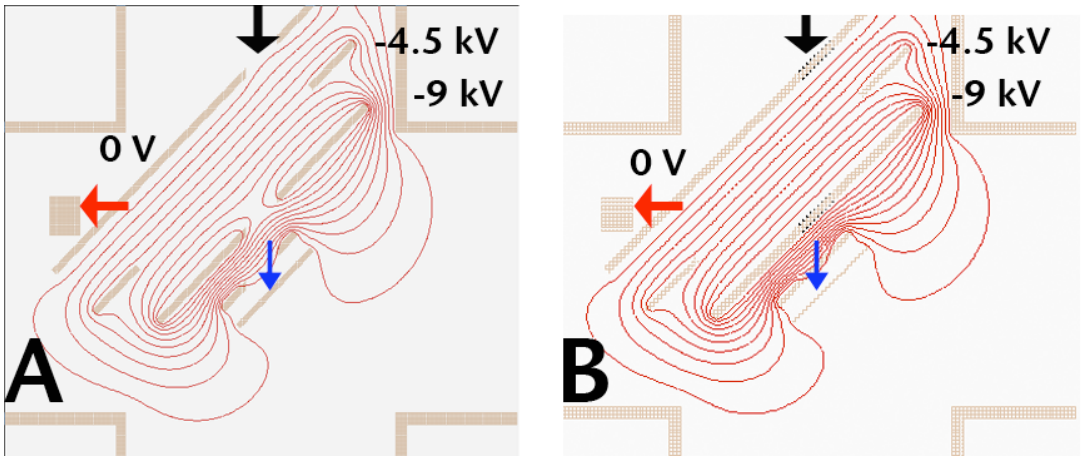

Figure 5.7: SIMION representation of the reflectron with equipotential lines. (a) presents the reflectron as constructed. (b) presents the reflectron with a grid on the front and rear electrodes. The labels on the figured are as described in Fig. 5.4.

A simulation identical to that used to create Fig. 5.6 was conducted, but the gridded reflectron was used. The results of this simulation are presented in Fig. 5.8. This simulation reveals that there is a magnification and steering effect caused by the

aberrations in the reflectron, when compared with Fig. 5.6. Even without the aberrations, the MCP appears to be positioned slightly off-center.

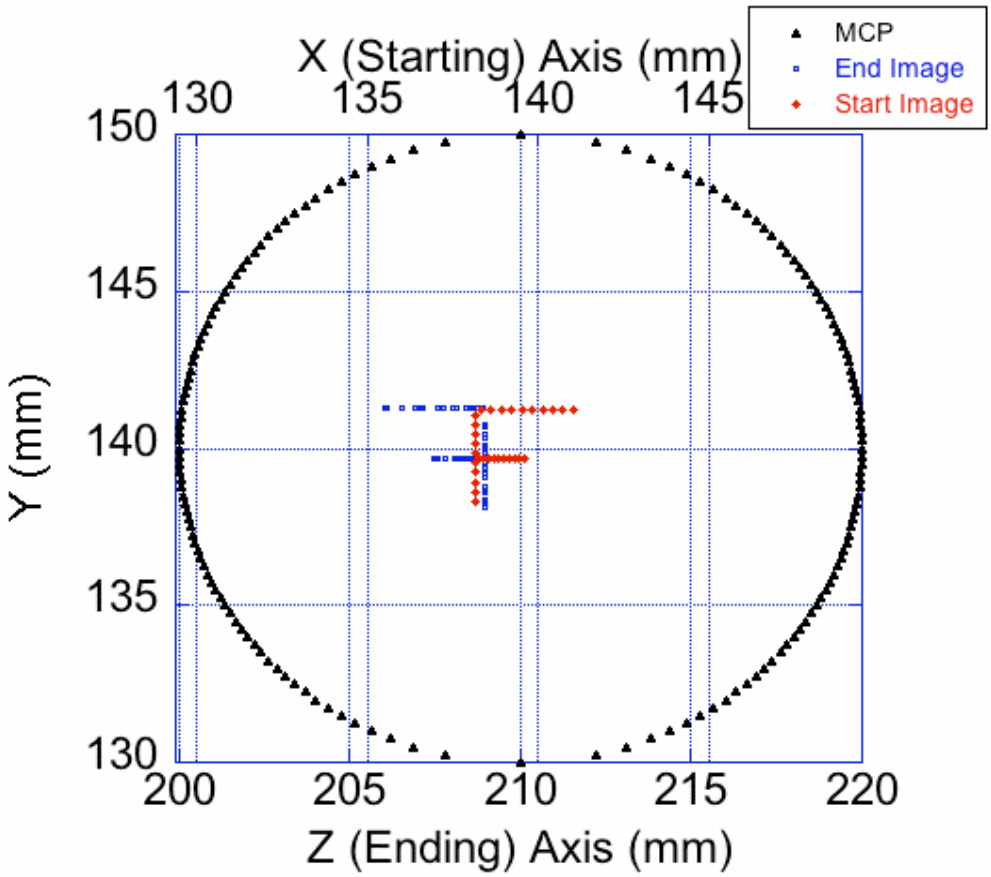

Figure 5.8: Graph depicting the starting ion image and final ion image through the gridded reflectron ion mirror and its centering on the MCP. Red diamonds represent the starting position of ions in the simulation on the x axis, blue squares represent the end position of the ions on the z axis, and black triangles represent the area of the MCP on the z axis. The shift from the x to z axis reflects the 90^0 bend through the reflectron. Units are mm.

Further studies using the reflectron simulation without the grid revealed the largest beam that could be completely transmitted to the MCP, without steering, was 6 mm in diameter. It is possible the beam could be larger than this in the experimental system and so is being cut by the reflectron. The beam can be centered on the MCP by an increase in reflectron voltages, however this causes increased aberrations and decreases the size of the beam that can be transmitted to the MCP. In order to truly correct for the non-centering of the MCP, the reflectron would need to be rebuilt to compensate for the aberrations.

Section 5.3: Detection Electronics

In order to properly detect negative ions, the rear plate of the MCP must be biased at high voltage. The signal therefore floats on the high voltage bias. This high voltage background must be removed in order to process the signal in most detection electronics. The first generation of detection electronics employed an Ortec 142PC pre-amplifier to accomplish this. This initial data, presented in Fig. 6.5 and 6.6, showed only one peak in the spectrum. Part of this was due to the pulsing system, as mentioned in Sec. 5.1, however, the Ortec 142PC also has a long rise time (~25 ns). The pre-amplified signal was then fed to a Canberra 2026 shaping amplifier. A shaping amplifier is typically not used in TOF systems because they are used to shape the pulse for accurate energy and pulse height information. This, however, comes at a sacrifice to time resolution. A Lecroy level discriminator was used to process the signal from the amplifier. Level discriminators are also not typically used in TOF analysis. A level discriminator produces a signal as soon as a pulse crosses a certain threshold level. Because the peaks generated from the MCP can have different pulse

heights, a level discriminator can cause jitter in the determined time of arrival of a pulse. All of these factors contributed to a broad time peak. The signal from the level discriminator was then processed by a time-to-digital converter (Lecroy VT960) and software to determine the TOF. In this first iteration of detection electronics, the equipment selections were based on equipment that was already in use with the NRL-TEAMS system. The results, however, forced an evaluation of the proper equipment needed.

Commercially available pre-amplifiers that include the ability to select the signal off a high-voltage bias with sufficient timing resolution could not be found. Therefore, for the second generation of detection electronics, a capacitively-coupled current pick-off (CCP) was designed by the NRL TEAMS facility's electronics technician, Claire Kennedy. A circuit diagram of the initial CCP is presented in Fig. 5.9. The resistor and capacitor between the high voltage and the output signal create a high pass filter. At DC and low frequency, the impedance through these components is high, isolating the DC voltage and any low frequency ripple. At high frequency, the impedance is low, allowing signal pulses from the MCP to cross the capacitor.

Initially, it was determined the signal peaks from the CCP were very broad, on the order of 100 μs. Upon investigation, the capacitor used in the CCP was too large, 1 μF, resulting in a 50 μs time constant. This long time constant integrated all the pulses generated by the MCP over time, resulting in the broad peaks seen in the initial data using this system. This was corrected by replacing the capacitor with a 1.5 pF capacitor, resulting a time constant of 75 ps. This allows for significantly sharper

peaks and provides the ability to collect spectra with multiple peaks. This CCP was used to collect all remaining data.

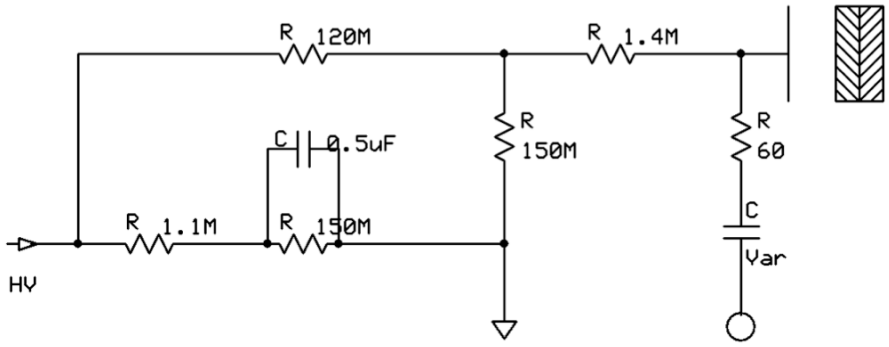

Figure 5.9: Capacitively-coupled current pick-off circuit diagram. The capacitor labeled "Var" was initially 1 μF, but changed to 1.5 pF in further experiments.

Further improvements were made in the second generation of detection electronics. Signals leaving the CCP are processed by an Ortec VT120-C pre-amplifier to increase the pulse height. This pre-amplifier has a 1 ns rise time, compared to that of 25 ns for the 142PC. Further amplification could broaden the peak width because of delays caused by amplifiers and after pre-amplification the pulse height was sufficient for analysis so further amplification was not employed. Also, the level discriminator was replaced by a Lecroy 3420 constant fraction discriminator (CFD). Unlike a level discriminator, a CFD produces an output signal at a constant fraction of each individual pulse's height. This provides a more consistent determination of the pulse time with less jitter. The Lecroy VT960 TDC was not changed.

These changes in electronics, combined with the improved pulsing system described in Sec. 5.1, produced a much greater capability of signal processing. The peaks produced from the system were reduced from 1 μs FWHM to 25 ns FWHM. However, the current settings used with the TDC only allow for 64 μs of data to be collected. This currently limits the mass range of the instrument because high mass species, approximately > 180 u, require longer than this time period to fly through the system. Several software-based solutions are available with the current TDC and alternative commercial schemes have also been investigated. Future work on this system should focus on such improvements. A summary of the different stages of detection electronics used in the experiments presented in Chap. 6 is presented in Table 5.2.

Table 5.2: Summary of Detection Electronics Development

Generation	First	Second
Signal pick-off	Ortec 142PC pre-amplifier	Home-made CCP (Fig. 5.8)
Amplifier	Canberra 2026 shaping amplifier	Ortec VT120-C pre-amplifier
Discriminator	Lecroy level discriminator	Lecroy 3420 constant fraction discriminator
Time to Digital Convertor	Lecroy VT960	Lecroy VT960

Chapter 6: Experimental Evidence

A series of experiments were conducted in order to provide experimental validation for the benefits of Pretzel-based TOF analysis. As was noted in Sec. 4.2, the SIMION simulations suggest the NRL-TEAMS system is not ideally designed for TOF work. Thus a true comparison of mass resolution between a Pretzel-based TOF system and a more traditional system cannot be conducted using the NRL-TEAMS system. This work instead seeks to confirm that the inherent Pretzel magnet properties allow mass filtering and time dilation to occur and that the theoretical relationships predicted in Chap. 3 from the derivation of equations describing the fundamental properties of the Pretzel magnet can be realized in an experimental system. Additionally, the experimental results can be used to confirm the validity of the SIMION model. In order for a more direct comparison of MF-TD-TOF and traditional TOF mass spectrometry, it would be necessary to design a TOF system with a Pretzel magnet as the spectrometer, rather than using the NRL-TEAMS system, which is not designed for TOF experiments.

For this work, only the pre-accelerator portion of the NRL-TEAMS facility was used (Fig. 4.3). All measurements were conducted with a Cs^+ primary beam with the primary and secondary ion energy set to 9 keV. All spectra were collected with 1-ns time resolution.

Section 6.1: Mass Filtering

Two mass filtering experiments were performed to determine the validity of the concept and to determine the potential benefits of its use. These experiments are summarized in Table 6.1.

Table 6.1: Summary of Mass Filtering Experiments.

Experiment	**1**	2
Sample	Graphite	Graphite
Pulsing electronics[1]	First generation	Second Generation
Detection electronics[2]	First generation	Second Generation
Pulse Width	2 μs	100 ns
Dwell Time	8 μs	78 μs, 6.8 μs,
Mass	12	16-17, 72-79
Field	5359 G	5890 G
Figure	6.1	6.2-6.4

1: See Table 5.1
2: See Table 5.2

Mass filtering experiment 1 was conducted using a graphite sample, the first generation pulsing system summarized in Table 5.1, and the first generation detection electronics summarized in Table 5.2. The Pretzel magnet was fitted with a mask that transmitted ^{12}C at 5359 G. A 2-μs-wide pulse followed by an 8-μs-long dwell was applied. Figure 6.1 presents this example of the benefit of mass filtering. Collected on the same TOF spectrum is the rapidly (100 kHz) and continuously pulsed ^{12}C beam. Because the Pretzel magnet mask filters all masses other than ^{12}C, one advantage of the Pretzel magnet is the ability to introduce pulses in rapid succession.

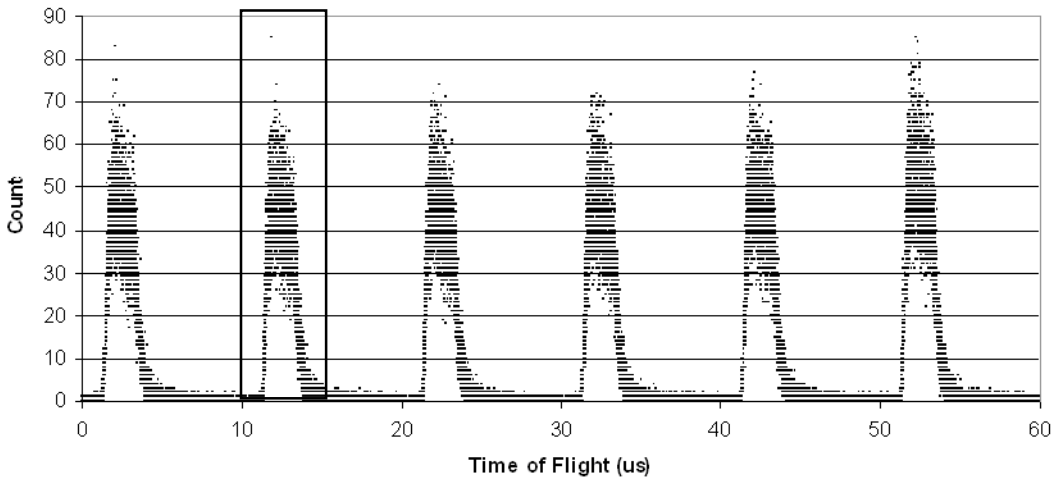

Figure 6.1: TOF spectrum of ^{12}C at Pretzel magnet field of 5359 G with a 2-μs pulse and 8-μs dwell. The box surrounds the time peak resulting from the pulse at time 0 s. (Demoranville et al. 2009)

The flight time of ^{12}C is approximately 12.4 μs at this field. The second peak in Fig. 6.1, surrounded by a box, corresponds to this TOF. The first peak in the spectrum is the result of a prior beam trigger pulse at -10 μs. The peaks are entirely from ^{12}C, as only that mass was selected for transmission through the Pretzel magnet, enabling MF-TOF analysis. For conventional TOF without mass filtering, each peak in the series would contain ^{12}C but could also contain contributions from other masses, arising from different start pulses. By removing these extraneous masses, this mode of operation increases the duty cycle of a MF-TD-TOF instrument, in this case to about 20%.

While this initial experiment begins to illustrate the benefits of mass filtering, the improvements made to the pulsing and detection systems allowed for improved

data to be collected. A second experiment using a graphite sample and the second generations of pulsing and detection electronics described in Table 5.1 and 5.2, respectively, was conducted. For this experiment, a non-filtered time spectrum was collected with a 100-ns pulse width and a 78-μs dwell time with no mask in the Pretzel magnet and a field of 5890 G, resulting in the spectrum in Fig. 6.2.

Next a mask designed to transmit masses 16-17 and 72-79 at the same field was inserted at the Pretzel magnet symmetry axis. The time spectrum in Fig. 6.3 was collected from the same graphite sample with identical parameters, that is a 100-ns pulse width and a 78-μs dwell time, to ensure filtering of all intended masses. This filtering allowed for the decrease of the dwell time such that ion pulses occurred more frequently, interleaving the analyzed peaks. The dwell time was decreased in order to show the interleaving of peaks and to determine the duty cycle increase. In this experiment the optimum dwell time was determined to be 6.8 μs. The spectrum resulting from this decreased dwell time is presented in Fig 6.4.

In Fig. 6.2 through 6.4, the data have been normalized to the mass 16 peaks to account for differences in the ion beam current and analysis time. In each of the three figures, the black peaks represent the peaks occurring from the start pulse at time 0. The gray peaks in Fig. 6.2 represent the peaks that are filtered by the Pretzel mask in Fig. 6.3 and 6.4. In Fig. 6.4, the gray peaks are interleaved pairs of peaks that arise from pulses starting before and after time 0. The annotations in Fig. 6.4 denote the pulse before or after the time 0 from which that peak originates.

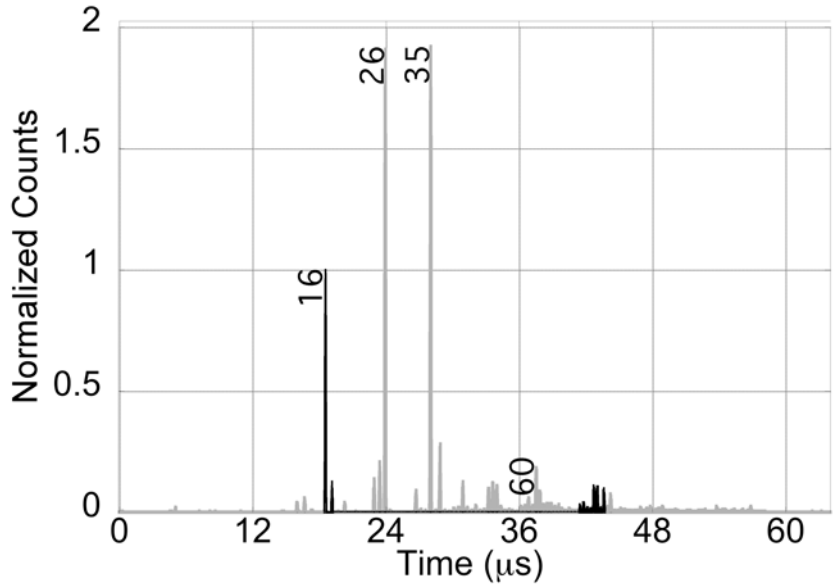

Figure 6.2: Non-mass filtered time spectrum of a graphite sample. Annotations are the mass of the peak. Counts are normalized to the mass 16 counts. The black peaks are transmitted when the Pretzel magnet mask is used; the gray peaks are not. (Demoranville et al. 2010)

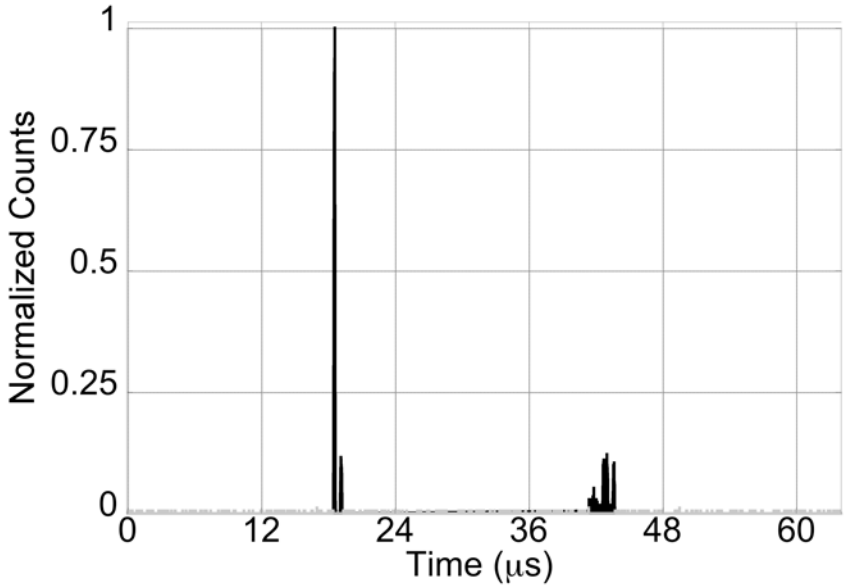

Figure 6.3: Mass filtered time spectrum of a graphite sample. Counts are normalized to the maximum of the mass 16 counts.

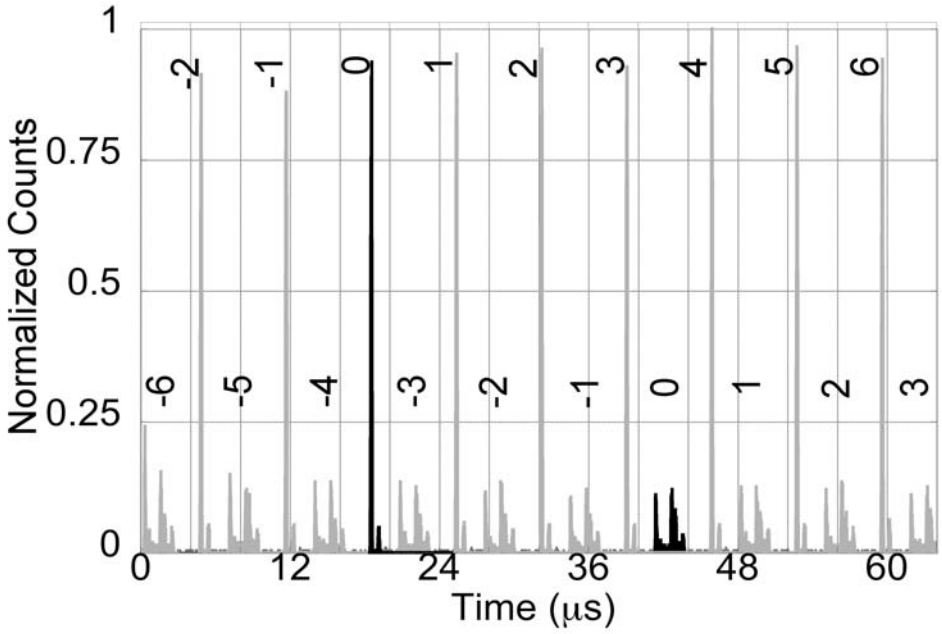

Figure 6.4: Mass filtered and interleaved time spectrum of a graphite sample produced with 100-ns pulse width and 6.8-μs dwell time. Counts are normalized to the maximum of the mass 16 counts. The mass filter is designed to select masses 16-17 and 72-79, as in Figure 6.3. The black peaks represent the peaks occurring from the start pulse at time 0. The gray peaks are interleaving pairs of peaks that arise from pulses starting before and after time 0. Annotations represent the index of the pulse from which the peak is produced, referenced to zero for the peaks that match the TOF scale of Fig. 6.2. Negative notations represent peaks originating from pulses before pulse 0. (Demoranville et al. 2010).

In this second experiment the duty cycle is increased from 0.12% to 1.5%. This is larger than the duty cycle of traditional TOF spectrometers, but is lower than achievable with orthogonal acceleration and Hadamard transform spectrometers

(Fernandez et al., 2002). Certain orthogonal and traditional TOF instruments make use of a filtering capability to remove matrix related background, such as Ar^+ in an ICP-MS TOF instrument (Cotter, 1997 p. 150). However, this scheme does not, and could not, improve duty cycle by interleaving peaks. Simply filtering one species is not sufficient to interleave peaks and create an increased duty cycle. Additionally, the method of pulsing differs and does not allow for the type of filtering achievable with the Pretzel magnet. However, if particular ranges of masses are of interest, using a Pretzel magnet as a mass filter allows the duty cycle to be tuned depending on the species of interest in a specific application. By studying fewer masses or increasing time resolution it may be possible to interleave a larger number of peaks and thereby further enhance the duty cycle.

In order to understand the potential for improvement in duty cycle, a simulation program was created using Labview software that utilized a simulated flight time for a given mass, and a variable peak width and dwell time to simulate a time spectrum (National Instruments, 2003). A series of masses can be entered into the program at a given peak width and the dwell time between pulses varied until the maximum interleaving with no overlap occurs. One interesting case for nuclear forensic applications is the simultaneous detection of oxygen and uranium isotopes. In this case the isotopic mass for $^{16, 18}O$, and $^{233, 234, 235, 236, 237, 238}U$ were simulated and their flight time used in the program with various peak widths. The optimal dwell times for several peak widths, along with the resulting duty cycle are presented in Table 6.2. Over the peak widths selected, the duty cycle remains relatively constant at approximately 3.4%, suggesting no resolution penalty must be incurred for

increased duty cycle. The flight time of uranium isotopes in the system is approximately 70 μs. Therefore, a traditional TOF system of similar size with 25-ns pulse width would be limited to a duty cycle of 0.04%. Thus a Pretzel-magnet-based system offers a distinct advantage to the traditional TOF instrument. The duty cycle increase does not approach that of orthogonal or Hadamard systems, which, as noted in Sec. 2.2 can approach 100%. However, such systems have other limitations.

Table 6.2: Simulated Duty Cycles at Optimum Dwell Times for the Given Pulse Width.

Pulse Width (ns)	Dwell Time (ns)	Duty Cycle (%)
5	146	3.42
10	303	3.30
15	440	3.41
20	596	3.36
25	747	3.35
30	906	3.31

Section 6.2: Time Dilation and Model Validation

The series of experiments conducted to confirm the existence of a time dilation effect, determine its utility, and validate the SIMION model are summarized in Table 6.3.

The first set of experiments, one and two in Table 6.3, used the first generation pulsing and detection electronics summarized in Table 5.1 and 5.2. The Pretzel magnet was fitted with a mask with two slots. Using this mask ^{12}C was transmitted at 3661 G or 5359 G, and ^{28}Si was transmitted at 5550 G or 8233 G. A 200-ns wide pulse with a 60−μs dwell was utilized. Silicon was transmitted at a particular field and a spectrum collected; the beam was stopped, the Pretzel magnet

field changed, and the next spectrum was collected as part of the same data set. Figure 6.5 presents such an over-layed spectrum and the ^{28}Si TOF peaks were measured at fields of 8233 G and 5550 G, respectively. The solid vertical bars represent the TOF predicted by the SIMION model for the Si data. Similar results, at 5339 and 3361 G, were obtained for ^{12}C, and are presented in Fig. 6.6.

Table 6.3: Summary of Time Dilation Experiments.

Experiment	1	2	3	4	5
Sample	Silicon	Graphite	Graphite	Graphite	Silicon
Pulsing electronics[1]	First generation	First generation	Second Generation	Third Generation	Third Generation
Detection electronics[2]	First generation	First generation	Second Generation	Second Generation	Second Generation
Pulse Width	200 ns	200 ns	100 ns	~29 ns	~29 ns
Dwell Time	60 μs	60 μs	78 μs	588 μs	588 μs
Mass	12	12	Full spectrum	Full spectrum	Full spectrum
Field	3661 & 5359 G	5550 & 8233 G	4000-16000 G 2000 G increments	4000-16000 G 2000 G increments	4000-16000 G 2000 G increments
K_P			2.29 ± 0.05	2.3 ± 0.2	
L_0			4.68 ± 0.02	4.7 ± 0.1	
$t_{electronics}$	787 ± 112 ns		1.1 ± 0.1 μs	5.7 ± 0.2	
Figure	6.5	6.6	6.2, 6.7-6.8	6.9, 6.11-12, 6.14	6.10, 6.13-14

1: See Table 5.1
2: See Table 5.2

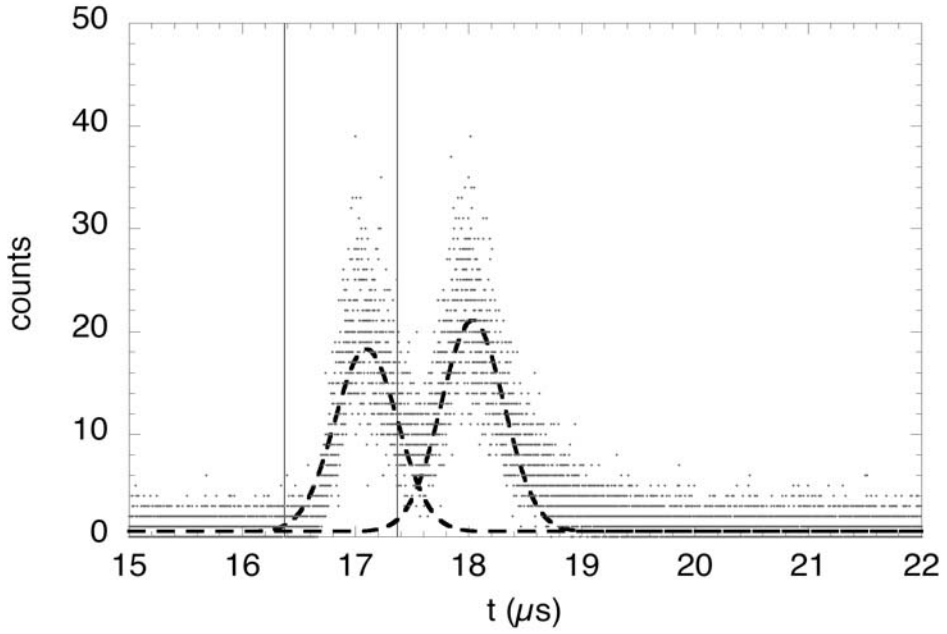

Figure 6.5: TOF spectrum of ^{28}Si at Pretzel magnet fields of 8233 G (left peak) and 5550 G (right peak). The solid lines indicate the TOF predicted by the SIMION model. Dashed lines indicate Gaussian fits to the data. (Demoranville et al. 2009)

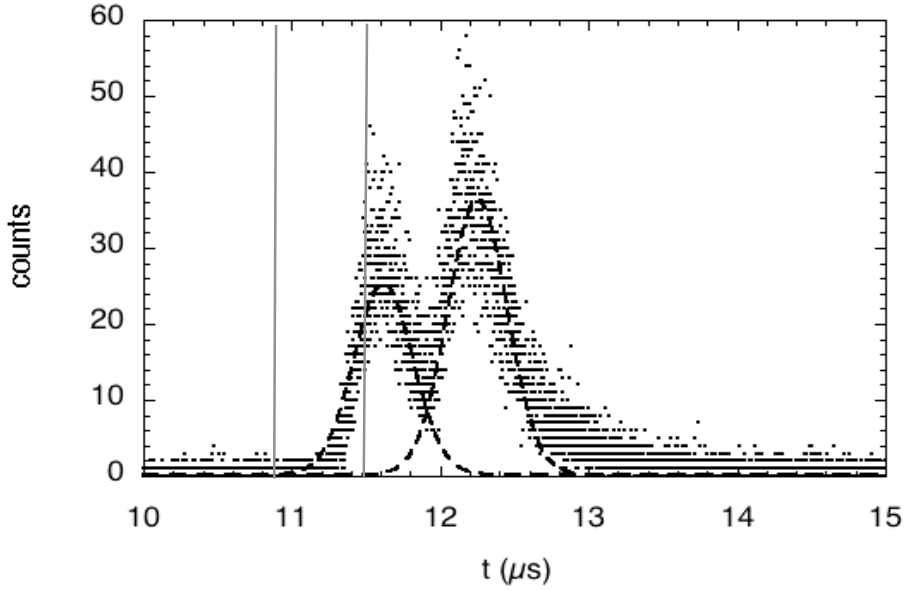

Figure 6.6: TOF spectrum of ^{12}C at Pretzel magnet fields of 5359 G (left peak) and 3361 G (right peak). The solid lines indicate the TOF predicted by the SIMION model. Dashed lines indicate Gaussian fits to the data.

In both cases, as expected, decreasing the Pretzel magnet field increases the flight time. For both the simulation and the experimental data, the difference in flight time between the two silicon fields is about 1 μs and the difference between the two carbon fields is about 0.63 μs, however the absolute TOF values are somewhat different. The computer simulation predicts an average flight time that is 787 ± 112 ns shorter than the recorded flight times. Table 6.4 presents the TOF obtained from the simulation and the experiment for C and Si at each field. The discrepancy in time can be explained by the delay in pulse generation following a trigger request associated with the electronic components, the response time of the electrostatic deflector used to pulse the beam, and other electronic delays. This is described as the $t_{electronics}$ in Eq. 3.9. This data set suggests the design of the model is accurate, as it can accurately predict the flight times. However, the effects of time dilation on mass resolution cannot be determined because of the limitations in the pulsing and detection electronics.

Table 6.4: Experimental and Simulated TOF and Difference by Species and Field.

Species & Field	Experimental TOF (μs)	Simulated TOF (μs)	TOF Delta (μs)
Carbon 5359 G	11.619	10.73472	0.88428
Carbon 3361 G	12.253	11.37372	0.87928
Silicon 8233 G	17.096	16.37669	0.71931
Silicon 5572 G	18.036	17.37199	0.66401

In order to further validate the model and evaluate the effects of time dilation, the third experiment in Table 6.3 was conducted on a graphite sample, using the second generation of pulsing and detection electronics, summarized in Table 5.1 and

5.2. The following time dilation experiments were conducted using 100-ns pulse width and 78-μs dwell time with no mask in the Pretzel magnet. The Pretzel magnet field was varied from 4 kG – 16 kG in 2 kG increments. An example of the time spectra collected from graphite was presented in Fig. 6.2. Several peaks are identified by mass on that spectrum. The location of the peaks changed in time but not in fingerprint at the different Pretzel magnet fields.

To provide a time-to-mass calibration, after the time spectra had been obtained, a Pretzel mask with a 1-u slot was installed in the Pretzel magnet. The time-to-mass calibration was obtained by determining the flight times of ions transmitted through the 1 u slot at a previously calibrated location and field. The resulting time information was used to establish characteristic peaks in the spectra. This enabled definitive identification of several mass peaks, with others identified by interpolation. As was described by Eq. 3.1, in typical TOF analysis path length is constant so time is proportional to the square root of mass, $\sqrt{m}$, at constant energy. Figure 6.7 presents time data collected at various field settings of the Pretzel magnet plotted versus $\sqrt{m}$. The dashed line is a linear guide to the eye at 4 kG. The solid line in the plot represents a calculated value of the TOF through the non-Pretzel portion of the NRL system. A length of 4.7 m was used for this calculation, using Eq. 3.9.

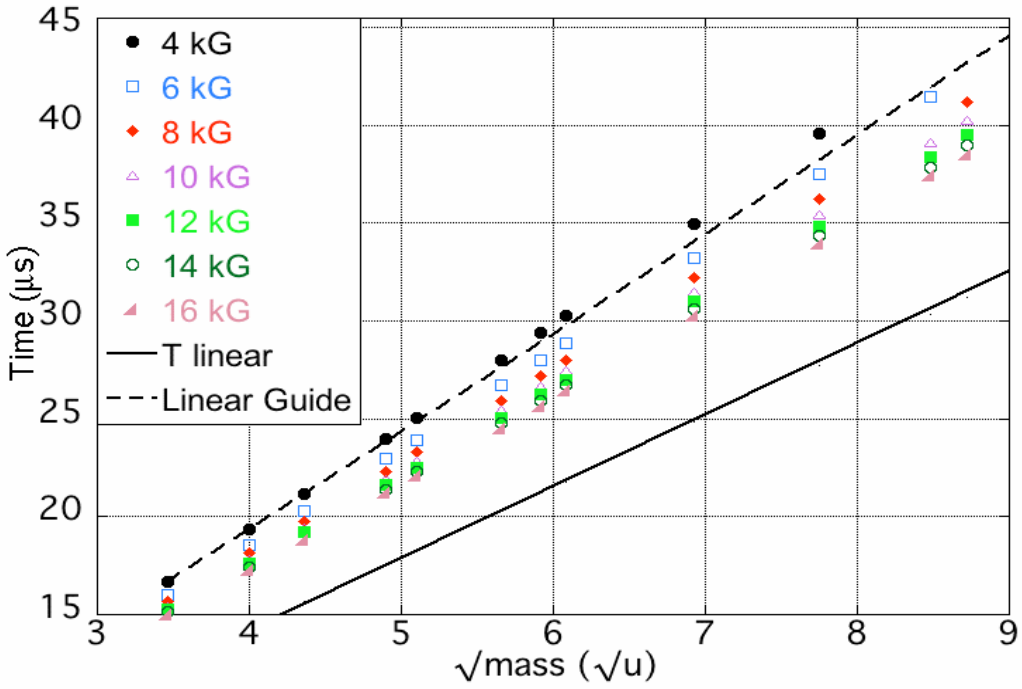

Figure 6.7: Flight time versus square root of mass for data at various fields. The dashed line is a linear guide to the eye at 4 kG. The solid line with no data points is the calculated time-of-flight over the path outside the Pretzel magnet.

It is evident from Fig. 6.7 that the experimental data is slightly non-linear with regard to √m. This supports the theoretical Eq. 3.9, which states the TOF in a Pretzel-magnet based system will display a relationship that is not simply linear in relation to √m. Using n = 0.925 and E = 9 keV, Eq. 3.9 further simplifies to:

$$t_{total} = 1.5097X10^{-5} K_P \frac{m^{0.75974}}{B^{0.51948}} + 7.5881X10^{-7} L_O \sqrt{m} + t_{electronics} \qquad (6.1)$$

The data from experiment 3 was fit using Eq. 6.1 and several parameters were determined. The constant K_P is related to the geometry of the trajectory in the Pretzel magnet. In Eq. 3.3 it is defined as the ratio of trajectory length to maximum

penetration in the Pretzel magnet. This can have a minimum value of 2, arising from the situation of an ion following a trajectory directly into and out of the Pretzel magnet, along the symmetry axis, to the penetration depth. In this situation the ratio is $(2*X_{max})/X_{max}$, or 2. Conversely, the maximum trajectory in the Pretzel magnet would be a circle. In this case, the trajectory can be described as the circumference of a circle with diameter X_{max}. The ratio then has the value $(\pi*X_{max})/X_{max}$, or π. Therefore, K_P is expected to be between 2 and π. By fitting a plot of time to mass, Fig. 6.8, for each field using equation 6.1, a series of values, m1, can be obtained for $1.5907x10^{-5}*K_p/B^{0.51948}$. These values are the coefficient of m and are presented in Table 6.5. Using these values K_P can then be calculated according to:

$$K_P = \frac{m1B^{0.51948}}{1.597X10^{-5}}. \qquad (6.2)$$

The series of values calculated for the data from this experiment is presented in Table 6.6, the average of which is 2.29 ± 0.05, with the error expressed as the standard deviation of the average. This value is in the expected range of 2-π.

The parameter L_O is the length of the trajectory outside the Pretzel magnet. The length can be determined from the fit presented in Fig. 6.8 and Table 6.5. The average m2 value from Table 6.5 is $3.55 \times 10^{-6} \pm 0.2 \times 10^{-6}$. This corresponds to an L_O of 4.68 ± 0.02 m, with the error calculated as the standard deviation of the data in Table 6.3. Calculation of the length outside the Pretzel magnet based on system design drawings results in 4.63 m. In both the case of L_O and K_p, there is good agreement between calculated and predicted values.

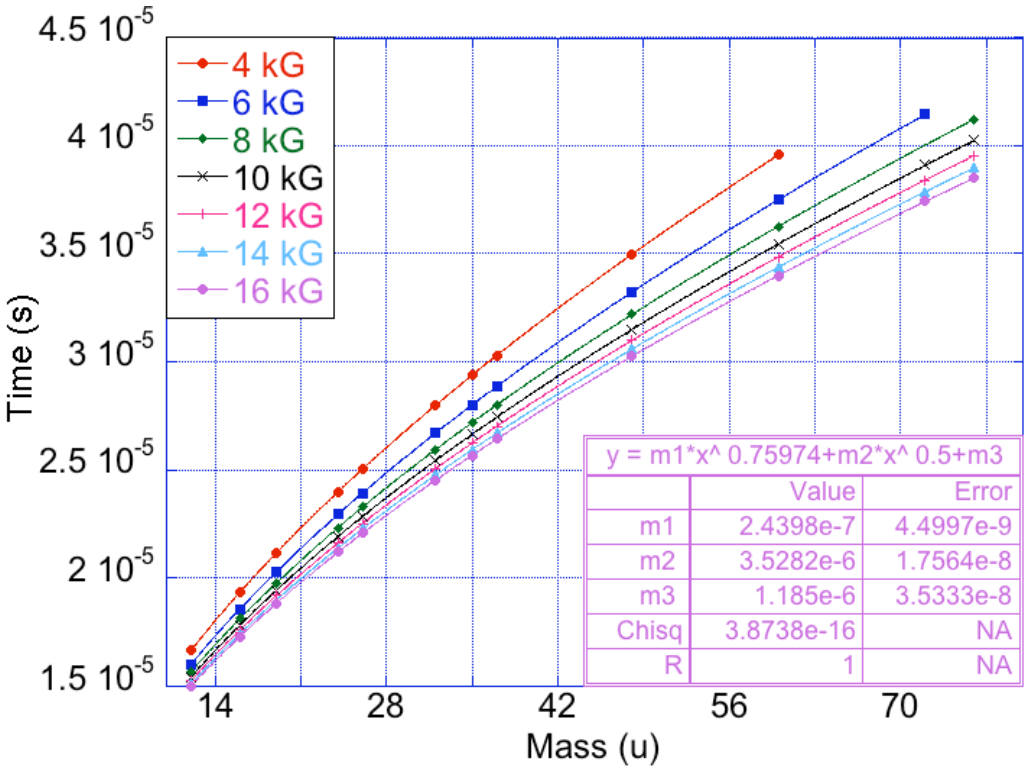

Figure 6.8: Experimental data fit with Eq. 6.1. The values for the fit are presented on the figure for the 16 kG case. The results of all fits are presented in Table 6.5.

The average $t_{electronics}$, from Table 6.5, is 1.1 ± 0.1 μs, with the error calculated as the standard deviation of the data. The results from the first experiment, presented in Table 6.4, suggested a 787 ± 112 ns electronics delay, as determined by comparison with computer simulations of the system. The difference in the current and previous electronics delay results from the changes to the pulsing system and collection electronics made between the first experiment and experiments 2 and 3.

Table 6.5: Fitting Parameters for Data from Fig. 6.8, using Eq 6.1.

	m1	m2	m3
Field (G)	$(1.5907x10^{-5} * K_p/B^{0.51948})$	$(7.5881x10^{-7} * L_O)$	$t_{electronics}$
4000	4.83×10^{-7}	3.56×10^{-6}	1.14×10^{-6}
6000	3.91×10^{-7}	3.56×10^{-6}	1.12×10^{-6}
8000	3.35×10^{-7}	3.57×10^{-6}	1.11×10^{-6}
10000	3.00×10^{-7}	3.56×10^{-6}	1.12×10^{-6}
12000	2.82×10^{-7}	3.53×10^{-6}	1.17×10^{-6}
14000	2.62×10^{-7}	3.53×10^{-6}	1.18×10^{-6}
16000	2.44×10^{-7}	3.53×10^{-6}	1.19×10^{-6}

Table 6.6: Calculation of K_P from m1 Values using Eq. 6.2.

	m1	$B^{0.51948}$	K_p
Field (G)	$(1.5907x10^{-5} * K_p/B^{0.51948})$		$(m1 * B^{0.51948}/1.5907x10^{-5})$
4000	4.83×10^{-7}	74.34	2.26
6000	3.91×10^{-7}	91.76	2.26
8000	3.35×10^{-7}	106.6	2.24
10000	3.00×10^{-7}	119.7	2.26
12000	2.82×10^{-7}	131.5	2.33
14000	2.62×10^{-7}	142.5	2.35
16000	2.44×10^{-7}	152.7	2.34

After the third generation of pulsing electronics summarized in Table 5.1 were implemented, experiment 4 and 5, listed in Table 6.3, were conducted on the time

dilation of the system. In contrast to the earlier experiments, 1-3, which were not well controlled for surface effects, these samples were initially sputtered for 30 minutes in non-pulsed mode, and then switched to TOF mode for analysis. To convert the time spectra to mass spectra, mass assignments based on the fingerprint of the spectrum were made for selected peaks across the entire spectrum. The time value of the peak was plotted against the mass value for the peak and fit using Eq. 6.1. The resulting equation was solved numerically for mass to generate a time-to-mass conversion. This conversion was used to generate the mass spectra contained in this section. The mass spectra for graphite and silicon are presented in Fig. 6.9 & 6.10, respectively. Both spectra were collected at 16 kG and for a duration of 200 s.

In earlier spectra, such as Figure 6.2, surface effects obscured the characteristic spectrum of the sample, as determined by Middleton (1990). However, with the initial 30-minute sputtering, the spectra displayed the characteristic pattern of ion intensities more closely. In the case of graphite, Fig 6.9, the major peaks from carbon closely follow the predicted pattern in mass and intensity as found by Middleton (1990). In the case of silicon, Fig. 6.10, molecular peaks from silicon oxide molecules appear to be present, which were not observed in Middleton's work. However, Middleton explained the absence of oxide molecules as due to the use of high purity silicon. While this current work made use of a high purity silicon wafer, oxygen peaks are frequently observed in the NRL-TEAMS system and a strong oxygen peak is present in Fig. 6.10, suggesting a significant background of oxygen. Thus, the formation of oxide molecules was not unexpected.

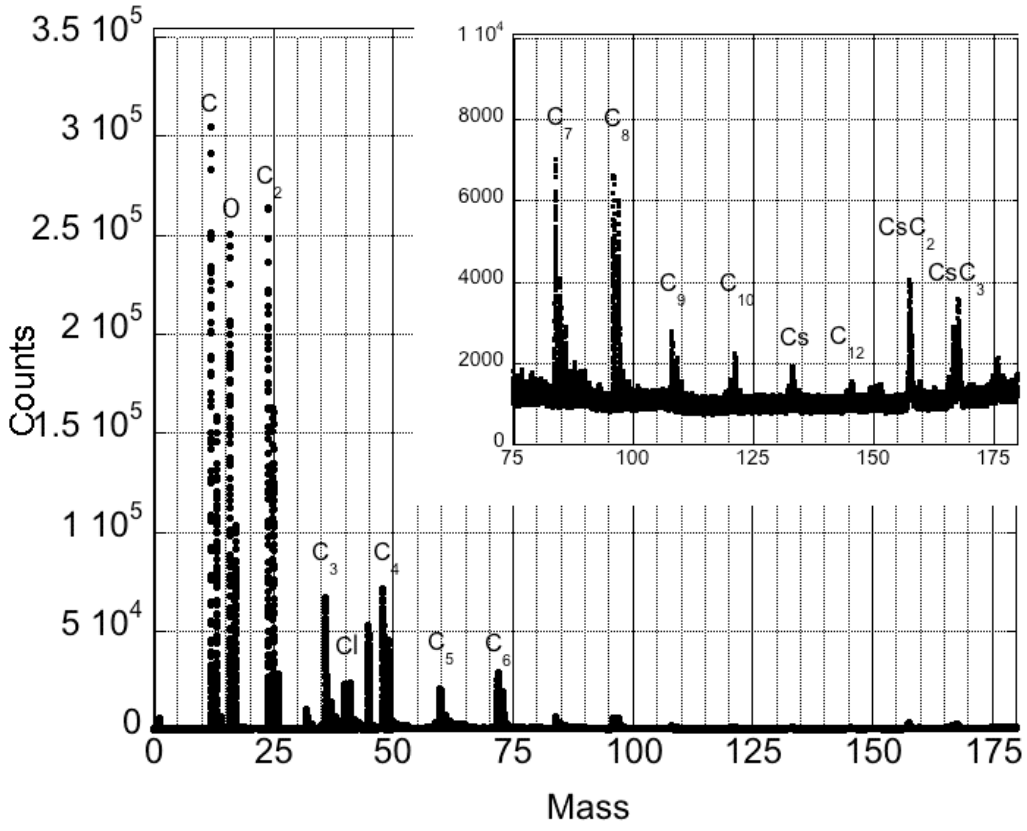

Figure 6.9: Mass spectrum of a graphite sample collected at 16 kG and for a duration of 200 s. Inset is an expanded view of the high mass portion of the spectrum. Annotations are the likely ion species.

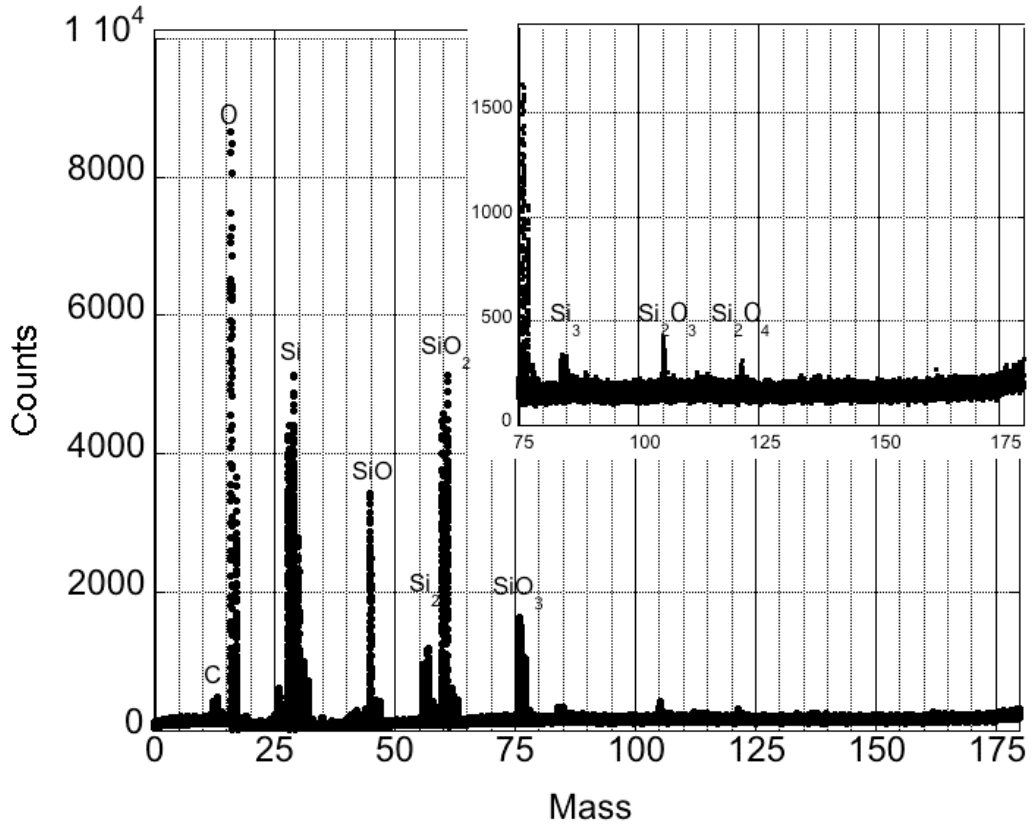

Figure 6.10: Mass spectrum of a silicon sample collected at 16 kG and for a duration of 200 s. Inset is an expanded view of the high mass portion of the spectrum. Annotations are the likely ion species.

Additionally, experiments 3 and 4 sought to verify the earlier results and show the day-to-day and sample-to-sample variability of the technique. To accomplish this a graphite sample was analyzed on three different days, and a silicon sample on two different days. The Pretzel magnet field was varied from 4 kG – 16 kG in 2 kG increments. A time-to-mass calibration was performed on the first day of analysis as described previously in this section in reference to experiment 3. This set of spectra was also analyzed to determine the constants from Eq. 6.1, as described in earlier in

this section for experiment 3. Table 6.7 presents the results of the fitting and calculations. This set of experiments results in $K_P = 2.3 \pm 0.2$, $L_O = 4.7 \pm 0.1$ m, and $t_{electronics} = 6.7 \pm 0.2$ μs. A summary of these parameters, and those determined from the earlier experiments, can be found in Table 6.8. The difference in the electronics delay between this and earlier experiments can again be attributed to changes in electronics, between the experiments. The values of K_P and L_O are within the error of the earlier experiments and the expected values. The larger uncertainty given in experiments 4 and 5 likely reflect systematic variability in day-to-day and sample-to-sample measurements, which were not present in the single measurement used to generate the data from experiment 4.

Table 6.7: Fitting Parameters and Calculations from Experiments 4 & 5, using Eq. 6.1.

	m1	m2	m3	K_p
Field (G)	$(1.5907 \times 10^{-5} * K_p/B^{0.51948})$	$(7.5881 \times 10^{-7} * L_O)$	$t_{electronics}$	
4000	4.84×10^{-7}	3.51×10^{-6}	5.93×10^{-6}	2.39
6000	3.97×10^{-7}	3.48×10^{-6}	5.98×10^{-6}	2.41
8000	3.50×10^{-7}	3.45×10^{-6}	6.01×10^{-6}	2.48
10000	3.04×10^{-7}	3.50×10^{-6}	5.91×10^{-6}	2.41
12000	2.33×10^{-7}	3.68×10^{-6}	5.51×10^{-6}	2.03
14000	2.14×10^{-7}	3.67×10^{-6}	5.54×10^{-6}	2.02
16000	2.02×10^{-7}	3.64×10^{-6}	5.67×10^{-6}	2.04

Table 6.8: Summary of K_P, L_O, and $t_{electronics}$.

Experiment	K_p	L_O	$t_{electronics}$
Expected	2-π	4.63 m	
1&2			0.787 ± 0.112 μs
3	2.29 ± 0.05	4.68 ± 0.02 m	1.1 ± 0.1 μs
4&5	2.3 ± 0.2	4.7 ± 0.1 m	5.7 ± 0.2 μs

Section 6.3: Time Dilation and Mass Resolution

One of the interests in using time-dilated TOF-MS is to increase the mass resolution capability of TOF instruments. While the SIMION model of the NRL-TEAMS system suggests that its mass resolution is fundamentally limited by parameters not related to time dilation (see Sec. 4.2), it is important to determine if the mass resolution of a TD-TOF-MS system does behave as theoretically predicted in Sec. 3.2. Additionally, experimental evidence can be used to validate the SIMION model.

The data from experiments 4 and 5 were further analyzed for mass resolution. The peaks of selected masses were fit with a Gaussian function. An example for 12 u, measured at 10 kG, is presented in Fig. 6.11. The peak widths from the Gaussian fit were converted to FWHM and mass resolution (m/δm) was taken as the nominal mass divided by the FWHM.

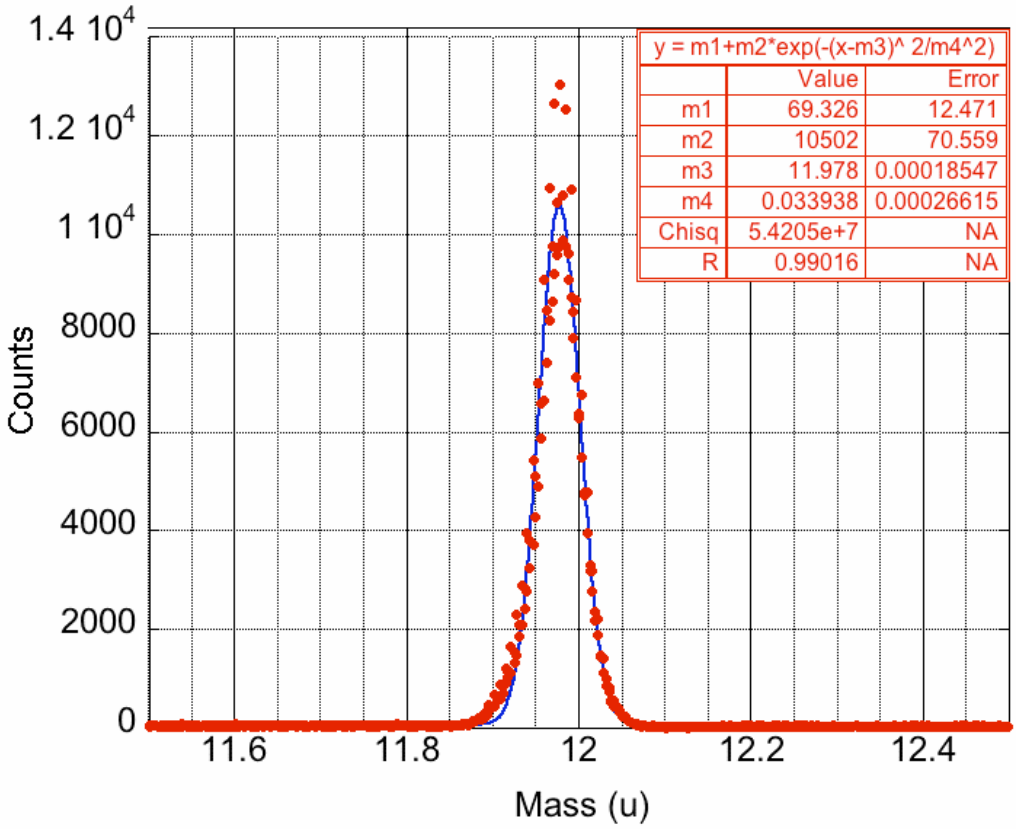

Figure 6.11: Mass 12 u peak measured at 10 kG (red circles) fit with a Gaussian function (solid blue line). The inset box presents the parameters of the Gaussian fit, as calculated by Kaleidograph (Synergy Software, 2010).

Figures 6.12 and 6.13 present the results of the mass resolution calculations for the graphite and silicon samples, respectively. Both figures present the mass resolution in m/δm, plotted versus field for various masses. In both figures, the series of data labeled as "Both 16" presents the average mass 16 data from both the graphite and silicon samples. The error bars in both cases are from the standard deviation from the trials made over the course of several days and are presented for two masses

in each plot. The error bars are of similar magnitude for the other masses and are not presented.

Mass resolution values range from approximately 100 m/δm, in the case of mass 28 from silicon at fields above 8 kG, to approximately 320 m/δm, in the case of mass 105 from silicon at 8 kG. More importantly, when plotted versus field, the overall trend of the data is as expected, e.g. the mass resolution decreases with increasing field. This trend is present only at high masses and is not evident at low masses. As suggested by the simulated 28-u data presented in Fig. 6.13, at low mass the improvement in mass resolution is minimal compared to the error present in the experimental data. The lack of a clear correlation between mass resolution and field at low mass may therefore be due to the error present in the data. While these mass resolution numbers are not large enough for a state-of-the-art TOF instrument, they may allow for some routine TOF measurements where high mass resolution is not necessary. More importantly, the SIMION simulations in Chap. 4 suggest that some of the limitations to mass resolution are functions of the NRL-TEAMS system design. A more appropriately designed, truly TOF instrument would be capable of significantly improved results. Additional improvements to mass resolution are also achievable using the NRL-TEAMS system by conducting experiments at lower acceleration energy and by installation of apertures, for reasons explained in Chap. 4.

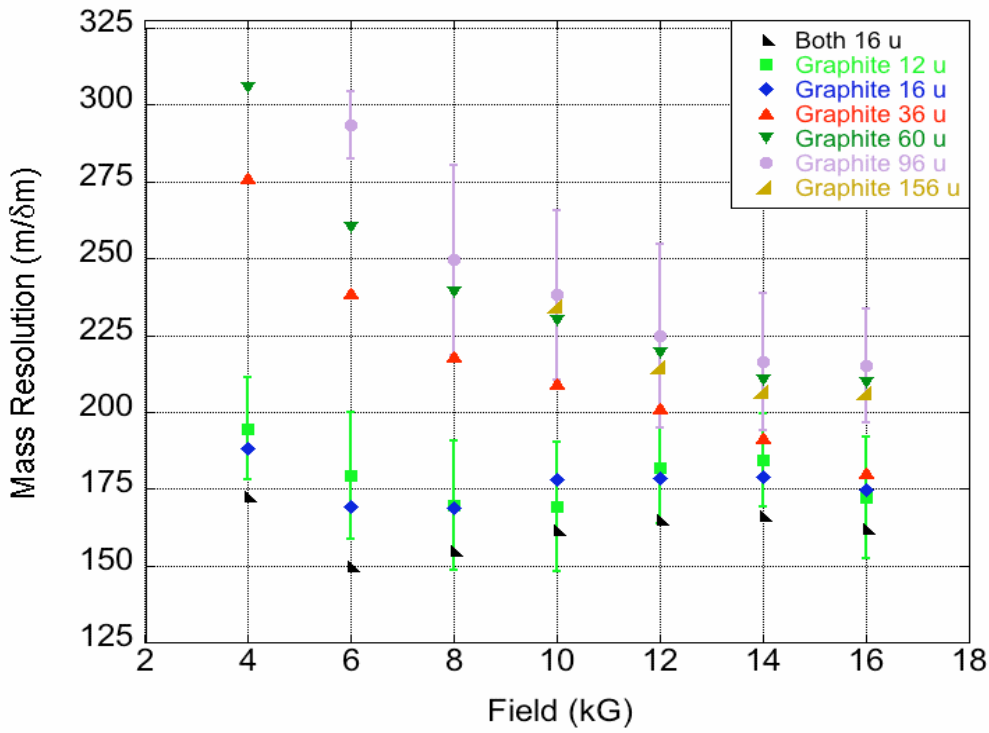

Figure 6.12: Mass resolution presented as mass/FWHM versus field for a graphite sample. Error bars represent the standard deviation of data points taken over several days and are representative of the size of errors for each mass.

This data does suggest that the initial conditions chosen for the SIMION simulations are appropriate to estimate the mass resolution. The solid, gold line presented in Fig. 6.13 is the data from the simulation presented in Fig. 4.2 using the starting conditions from Gnaser (2000) and Verdiel et al. (2008). These conditions slightly overestimate the mass resolution that is actually achieved in the physical system. This is not unexpected, as the model does not account for the initial pulse width. In the simulated data the width of the time data, measured as FWHM, ranges from 80-91 ns, whereas the width in time for silicon in the experimental data ranges from 98-122 ns. Because of the manner of pulsing described in Sec. 5.1, it is not

possible to directly determine the pulse width of the system, but it is likely the pulse width is contributing to the spread in TOF, lowering the mass resolution from the levels predicted by the simulation. This data suggests the pulse width is at least 18-31 ns. This value is on the order approximated by other researchers using similar pulsing systems (Chait & Standing 1981; Rathmann et al. 1985; Katta & Chait 1991; Ma et al. 1992; Piel et al. 1999).

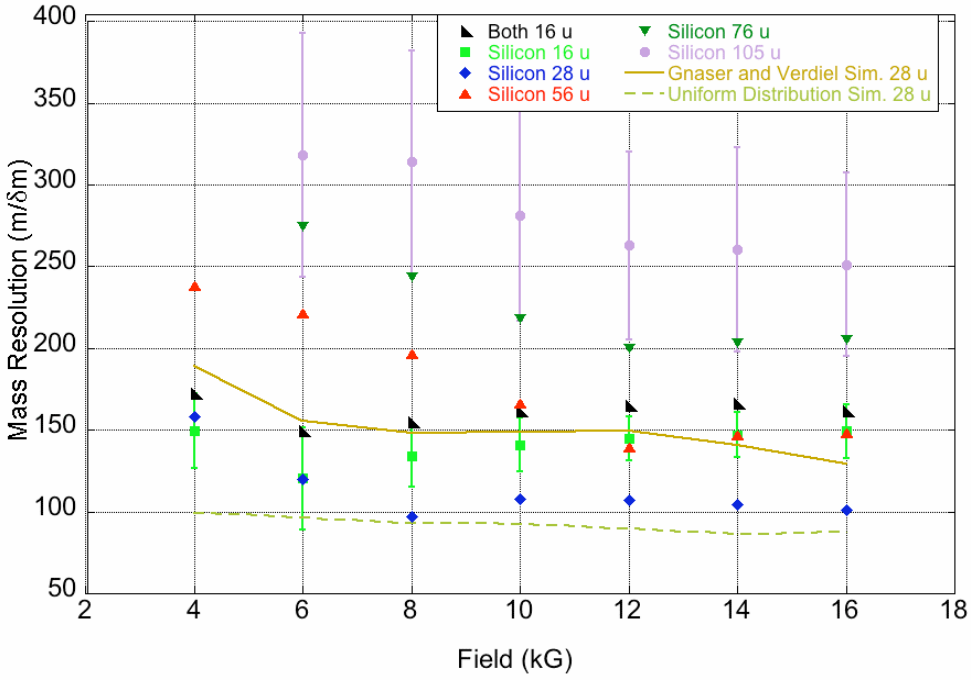

Figure 6.13: Mass resolution as mass/FWHM versus field for a silicon sample. Error bars represent the standard deviation of data points taken over several days and are representative of the size of errors for each mass. Mass 76 and 105 are not transmitted through the Pretzel magnet at 4 kG, so data for those masses begin at 6 kG. The simulated data is from Fig. 4.2. The gold solid line used the literature data from Gnaser (2000) and Verdiel et al. (2008) as the starting conditions. The olive dashed line used the uniform angular and energy distributions described in Sec. 4.2.

The simulations using the uniform distribution of energy and angular distributions are presented in Fig. 6.13 as the dashed, olive line and were originally presented in Fig. 4.2. These conditions slightly underestimate the mass resolution achievable. Because these conditions overestimate the initial angular distribution range, a more broad range of TOF values would result. The more broad range of TOF values results in a lower mass resolution estimation. These results confirm the validity of the SIMION model and suggest that significant changes to the initial modeling conditions are not necessary but provide a reasonable estimation of the mass resolution of the system.

It is also expected that mass resolution will increase as mass increases. Figure 6.14 presents the mass resolution data from the graphite sample taken at 10 kG. The mass resolution data were calculated directly from the mass spectra and from the time spectra, using Eq 6.1. The two methods agree very well, supporting the validity of the theoretical equation and justifying its use with the simulated data to calculate mass resolution, as well as offering justification for the time-to-mass conversion used to create the mass spectra. There is an increase in mass resolution with increasing mass, as predicted. The trend in this plot is representative of graphite at all fields.

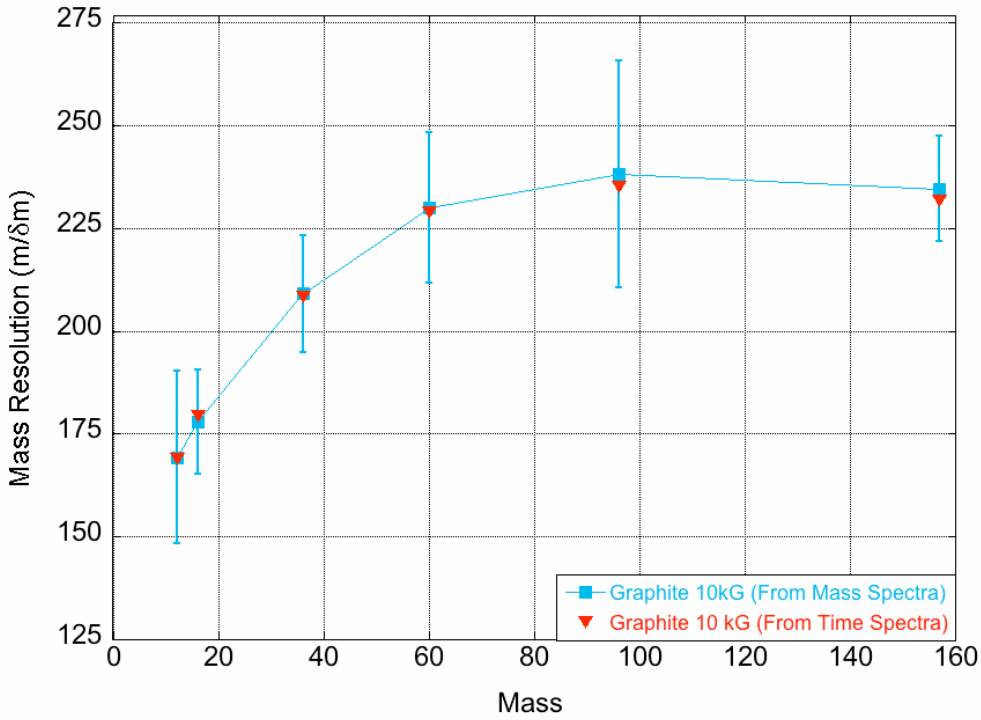

Figure 6.14: Mass resolution as mass/FWHM as a function of mass for the graphite sample at 10 kG. Mass resolution as calculated from the mass spectra (blue squares and circles) and from the time spectra using Eq. 6.1 (red triangles and diamonds). The lines are drawn as a guide to the eye. Error bars are presented for the mass spectra and are ± 1σ.

The predicted trend of mass resolution decreasing with increasing field further confirms the theoretical benefits of a Pretzel-magnet-based system. However, the NRL-TEAMS system is limited in its utility as a TOF instrument because of low mass resolution, which is unrelated to the Pretzel magnet. Additionally, the trends in mass resolution data exhibit some sample-to-sample variability. Further experiments need to be conducted to better understand and control the sample-to-sample variability in the mass resolution data.

Chapter 7: Conclusions

The NRL-TEAMS system has served as a test bed in simulations and experiments to test the concept of Mass Filtered, Time Dilated Time-of-Flight Mass Spectrometry (MF-TD-TOF-MS).

Section 7.1: Theoretical Background and Calculations

A theoretical analysis of Enge's original design and the NRL specific design of the Pretzel magnet led to a series of equations that predicted several of its key parameters, which could be experimentally confirmed provide evidence of the TD effect. Further, calculations based solely on these equations determined a Pretzel-magnet based TOF-MS may offer improvements over traditional, reflectron style instruments. This advantage was highest at low fields, high masses, and low energy. The assumption of similar size, that is a penetration depth equal to the same length as a reflectron, was, however, generous. A Pretzel magnet of that size would be heavier and of a greater width than a drift tube of equal depth. This could prove to be a limitation of such an instrument. However this only considers the TD effect, and the advantages of mass filtering are ignored. The coupling of these two benefits could provide for unique, niche research opportunities.

Section 7.2: SIMION Modeling

SIMION modeling of the NRL-TEAMS system provided the insight that the system was not ideally designed for TOF analysis and, therefore, experimental results cannot provide the high mass resolution an optimally designed system could. Rather, it could

be used as a test-bed to provide insight into the operation and design of such an instrument and confirm the functionality of the MF-TD-TOF-MS concept. These simulations suggest the electrostatic analyzer in the NRL-TEAMS instrument limits the mass resolution, as does the wide range of initial emission angles present in the NRL-TEAMS secondary ion source. Both of these limitations can be better constrained in a future MF-TD-TOF-MS instrument.

Additionally, the model allowed for the investigation of some species of interest, specifically actinides. With the knowledge that initial emission angle was a limiting factor in NRL-TEAMS, these simulations provided the opportunity to conduct experiments as if this factor had been controlled. A nearly order-of-magnitude improvement was seen, and mass resolution values nearing 1000 m/δm, making the technique competitive with some standard MS systems. An optimally designed system would achieve even higher mass resolution, further confirming the usefulness of a MF-TD-TOF-MS system.

Section 7.3: System Improvements and Experimental Results

A series of pulsing systems and detection electronics provided the necessary improvements to perform MF-TD-TOF-MS experiments at the NRL-TEAMS facility. A reflectron ion mirror was also designed installed and tested.

The experiments conducted confirmed the validity of the SIMION model in several ways. First, analysis of the data confirmed theoretical predictions of key parameters of the NRL-TEAMS instrument, including the geometric constant K_P and the length of the instrument outside the Pretzel magnet. Additionally, using a given

pulsing and detection electronics system, the time delay due to the electronics was consistent across several experiments.

Secondly, the mass resolution of the experiments was within the predicted range from the SIMION simulations. The simulations used two different starting conditions, one which should slightly overestimate the mass resolution and a second which should underestimate the mass resolution. The experimental mass resolution for the simulated species fell between the simulated values.

Additionally, the experimental results showed the predicted trend of decreasing mass resolution with increasing field, particularly at high (>36 u) mass. This confirms the value of TD to TOF analysis. The improvements offered by MF were also illustrated for a specific case, resulting in a more than ten-fold increase in duty cycle. It was also shown greater increases are possible, with the case of oxygen and uranium isotopes specifically simulated. In this case an increase from 0.04% to approximately 3.4% could be possible. While this is not necessarily competitive with some instruments, specifically OA and HT-MS instruments, it does offer some distinct advantages, such as the ability to block high intensity, non-interesting species and the ability to combine the technique with TD.

Section 7.4: Method Comparison

It is important to evaluate the utility of MF-TD-TOF-MS against some of the other recently developed TOF techniques: Hadamard transform (HT), orthogonal acceleration (OA), and multi-turn (MT). Table 7.1 presents a short summary of several key benchmarks for MS analysis. Rather than provide a complete review of

each of the techniques, the values presented in Table 7.1 are often for specific situations, but represent the state-of-the-art of those particular techniques.

Table 7.1 Comparison of TOF-MS techniques

TOF	Mass Resolution (m/δm– FWHM)	Duty Cycle (%)	Trans-mission[a]	Dynamic Mass Range	Sensitivity Limit of Detection (LOD)
HT	372[b] 743[c] (at 242 u)[d]	100[d]	100%[e]	>1,500 u[e]	LOD <5 pmol[e]
OA	7500[f]	20[g]	~20%[h]		$>10^6$ range[i] LOD 3 fmol[g]
MT	Variable 350,000[j]	0.0003[j]	Variable <20%[j]	$\frac{m_{mx}-m_{mn}}{m_{mx}} = 2/N^{k,l}$	LOD <50 fmol[j]
MF-TD	320[a] (at 105 u) ~550[b] (at 240 u)	Varies 1.5[a] 3.4[b]	>50%	240 u at 40 keV 1375 u at 9 keV 12,300 u at 1 keV	$>10^4$ range LOD not studied

a) This value is through the mass spectrometer only
b) Measured
c) Thought to be achievable
d) (Brock et al., 1998)
e) (Fernández et al., 2002)
f) (Guilhaus et al., 2000)
g) (Verentchikov et al., 1994)
h) (Myers et al., 1994)
i) (Ray and Hieftje, 2001)
j) (Toyoda, 2010)
k) Where m_{mx} is the maximum m/z value injected, m_{mn} is the minimum m/z value injected and N is number of turns.
l) (Verentchikov et al., 2005)

From Table 7.1 it is possible to determine some of the benefits and drawbacks of each of the techniques. HT-TOF-MS has very powerful increases in duty cycle and transmission, which are related, yet suffers from relatively poor mass resolution.

OA-TOF-MS is perhaps the most widely used and versatile of techniques, having relatively good mass resolution, reasonable transmission and good sensitivity. Yet, the dynamic mass range is not discussed directly in the literature, and several papers allude to the limitations of matching the fill time of the OA pulse region with the overall flight time through the analysis system. This limitation is linked with transmission and duty, as a reduced duty cycle will lower transmission, but increase the mass range allowed to traverse the system. Multi-turn TOF (MT-TOF) systems have incredibly high mass resolution. This is provided by ability to lengthen the flight path. However, each turn around the spectrometer reduces the transmission as well as requiring longer analysis times, thereby reducing the duty cycle. The dynamic mass range is also limited by "over-taking". This occurs when light, quickly moving ions over-take the slowly moving ions in the multiple turns around the system. The philosophy of use behind these systems is to obtain a broad, low-mass resolution scan of the analyte using one pass through the MT-TOF. Any interesting mass ranges in need of high mass resolution data are then separately analyzed using multiple turns through the spectrometer. The data presented in this thesis for MF-TD-TOF-MS suggests it is a relatively low mass resolution technique. However, it was also noted that higher resolution may be achievable through a number of means (i.e. limited angular divergence, lower energy, etc.). Additionally, it may be possible that the dynamic mass range could be higher for MF-TD-TOF-MS than in OA-MS without the sacrifice of duty cycle if interleaving would be appropriate. The transmission for this technique was not explicitly studied, but historical NRL-TEAMS measurements using a single mass suggest transmission will be better than 50% for multiple masses,

through the Pretzel magnet. This number is, of course, variable, as it may be lower if masses are filtered. A MF-TD-TOF-MS system may therefore offer advantages where it is important to achieve very high transmission of analyte. This is true in certain nuclear forensic investigations where sample material is limited. Additionally, further development of the technique may improve mass resolution to a more useful level.

Section 7.5: Future Directions

While this work has validated the MF-TD-TOF-MS concept and provided experimental and simulated evidence that such a technique can offer distinct advantages to TOF-MS analysis, many areas of research remain.

One key question is the ability of the Pretzel magnet to compensate for energy spread. The main advantage of reflectron TOF analysis is the ability of the instrument to perfectly time focus an ion beam with different energy, over a reasonable range. This contributes to the technique's high mass resolving power. The Pretzel magnet should have some ability to compensate for energy spread, because the geometric shape of an ion trajectory is given by momentum, a component of which is energy. Thus an ion with slightly higher energy will have slightly longer flight path. Because this ion is traveling slightly faster, due to its higher energy, this may serve as a time focus. The extent to which this phenomenon is present and able to provide a time focus needs to be investigated. If it is not a perfect time focus, then other elements in an optimally designed system may be able to be added to provide the time focus, or the Pretzel magnet may need to be designed with slightly different parameters to provide the time focus. Alternatively, it may be possible to use a Pretzel magnet as

the mass analyzer in an OA-MS, thereby combining the benefits of the Pretzel magnet with the energy compensation advantage of an OA-MS.

In order to design an optimally designed system, several other factors need to be taken into consideration. For example, it was shown by simulations in Sec. 4.2, that the electrostatic analyzer and the initial angular divergence in the NRL-TEAMS system was limiting mass resolution. An optimal system should be designed in such a way that the system elements do not provide limitations to mass resolution.

Other, more unique, systems could also be considered. It was mentioned in Sec. 2.2 that several groups have been developing multi-turn TOF systems. If a Pretzel magnet could be used in such a system, without degrading the time focusing abilities, the limitation of Pretzel magnet size could be overcome. By using multiple, small Pretzel magnets, it may be possible to magnify the TD effect, while maintaining a size significantly smaller than the current Pretzel magnet system.

While the NRL-TEAMS system is not an ideal system for MF-TD-TOF-MS, it does offer several opportunities for improvement, which if implemented could provide complimentary information to the complete NRL-TEAMS system. Currently the system has very low mass resolution, however simulations suggest the installation of apertures that would limit the initial angular divergence of the system could significantly improve mass resolution to a level competitive with standard MS instruments. Additionally, although several iterations of pulsing systems and detection electronics were used, improvements are still possible. The pulsing system should be changed to the “box-type” explained in Chap. 5.1. Commercially available detection electronics should be considered to enable the detection of species with

TOF longer than 64 μs. Additionally, some initial experiments using electropositive species have been conducted with limited success, but are not included in this thesis. This is not surprising, as electropositive species do not form strong negative ion beams. The NRL-TEAMS Cameca 6f recently has been outfitted with a duoplasmatron ion source, capable of forming positive secondary ion beams. The advantages of MF-TD-TOF-MS presented in this thesis for the electronegative silicon and carbon should be extended to electropositive species using this source with a positive secondary ion beam. This is particularly vital to the development of this technique to nuclear forensic applications, as actinide species are electropositive.

These improvements and continued areas of research would further improve MF-TD-TOF-MS and its potential to provide a new, novel method of MS analysis.

Appendices

Appendix A: Copyright Licenses

Appendix A.1:

Permission for the article:

Demoranville, L.T., K.S. Grabowski, D.L. Knies, and C. Cetina. 2010. Experimental demonstration of mass-filtered, time-dilated, time-of-flight mass spectrometry. *Surface and Interface Analysis.*

JOHN WILEY AND SONS LICENSE
TERMS AND CONDITIONS

Jun 11, 2010

This is a License Agreement between Leonard Demoranville ("You") and John Wiley and Sons ("John Wiley and Sons") provided by Copyright Clearance Center ("CCC"). The license consists of your order details, the terms and conditions provided by John Wiley and Sons, and the payment terms and conditions.

All payments must be made in full to CCC. For payment instructions, please see information listed at the bottom of this form.

License Number	2445951141970
License date	Jun 11, 2010
Licensed content publisher	John Wiley and Sons
Licensed content publication	Surface & Interface Analysis
Licensed content title	Experimental demonstration of mass-filtered, time-dilated, time-of-flight mass spectrometry
Licensed content author	Demoranville L. T., Grabowski K. S., Knies D. L., et al
Licensed content date	Jun 8, 2010
Start page	n/a
End page	n/a
Type of use	Dissertation/Thesis
Requestor type	Author of this Wiley article
Format	Print and electronic
Portion	Full article
Will you be translating?	No
Order reference number	
Total	0.00 USD

Terms and Conditions

TERMS AND CONDITIONS

This copyrighted material is owned by or exclusively licensed to John Wiley & Sons, Inc. or one if its group companies (each a "Wiley Company") or a society for whom a Wiley Company has exclusive publishing rights in relation to a particular journal (collectively "WILEY"). By clicking "accept" in connection with completing this licensing transaction, you agree that the following terms and conditions apply to this transaction (along with the billing and payment terms and conditions established by the Copyright Clearance Center Inc., ("CCC's Billing and Payment terms and conditions"), at the time that you opened your Rightslink account (these are available at any time at http://myaccount.copyright.com).

Terms and Conditions

1. The materials you have requested permission to reproduce (the "Materials") are protected by copyright.

2. You are hereby granted a personal, non-exclusive, non-sublicensable, non-transferable, worldwide, limited license to reproduce the Materials for the purpose specified in the licensing process. This license is for a one-time use only with a maximum distribution equal to the number that you identified in the licensing process. Any form of republication granted by this licence must be completed within two years of the date of the grant of this licence (although copies prepared before may be distributed thereafter). Any electronic posting of the Materials is limited to one year from the date permission is granted and is on the condition that a link is placed to the journal homepage on Wiley's online journals publication platform at www.interscience.wiley.com. The Materials shall not be used in any other manner or for any other purpose. Permission is granted subject to an appropriate acknowledgement given to the author, title of the material/book /journal and the publisher and on the understanding that nowhere in the text is a previously published source acknowledged for all or part of this Material. Any third party material is expressly excluded from this permission.

3. With respect to the Materials, all rights are reserved. No part of the Materials may be copied, modified, adapted, translated, reproduced, transferred or distributed, in any form or by any means, and no derivative works may be made based on the Materials without the prior permission of the respective copyright owner. You may not alter, remove or suppress in any manner any copyright, trademark or other notices displayed by the Materials. You may not license, rent, sell, loan, lease, pledge, offer as security, transfer or assign the Materials, or any of the rights granted to you hereunder to any other person.

4. The Materials and all of the intellectual property rights therein shall at all times remain the exclusive property of John Wiley & Sons Inc or one of its related companies (WILEY) or their respective licensors, and your interest therein is only that of having possession of and the right to reproduce the Materials pursuant to Section 2 herein during the continuance of this Agreement. You agree that you own no right, title or interest in or to the Materials or any of the intellectual property rights therein. You shall have no rights hereunder other than the license as provided for above in Section 2. No right, license or interest to any trademark, trade name, service mark or other branding ("Marks") of WILEY or its licensors is granted hereunder, and you agree that you shall not assert any such right, license or interest with respect thereto.

5. WILEY DOES NOT MAKE ANY WARRANTY OR REPRESENTATION OF ANY KIND TO YOU OR ANY THIRD PARTY, EXPRESS, IMPLIED OR STATUTORY, WITH RESPECT TO THE MATERIALS OR THE ACCURACY OF ANY INFORMATION CONTAINED IN THE MATERIALS, INCLUDING, WITHOUT LIMITATION, ANY IMPLIED WARRANTY OF MERCHANTABILITY, ACCURACY, SATISFACTORY QUALITY, FITNESS FOR A PARTICULAR PURPOSE, USABILITY, INTEGRATION OR NON-INFRINGEMENT AND ALL SUCH WARRANTIES ARE HEREBY EXCLUDED BY WILEY AND WAIVED BY YOU.

6. WILEY shall have the right to terminate this Agreement immediately upon breach of this Agreement by you.

7. You shall indemnify, defend and hold harmless WILEY, its directors, officers, agents and employees, from and against any actual or threatened claims, demands, causes of action or proceedings arising from any breach of this Agreement by you.

8. IN NO EVENT SHALL WILEY BE LIABLE TO YOU OR ANY OTHER PARTY OR ANY OTHER PERSON

OR ENTITY FOR ANY SPECIAL, CONSEQUENTIAL, INCIDENTAL, INDIRECT, EXEMPLARY OR PUNITIVE DAMAGES, HOWEVER CAUSED, ARISING OUT OF OR IN CONNECTION WITH THE DOWNLOADING, PROVISIONING, VIEWING OR USE OF THE MATERIALS REGARDLESS OF THE FORM OF ACTION, WHETHER FOR BREACH OF CONTRACT, BREACH OF WARRANTY, TORT, NEGLIGENCE, INFRINGEMENT OR OTHERWISE (INCLUDING, WITHOUT LIMITATION, DAMAGES BASED ON LOSS OF PROFITS, DATA, FILES, USE, BUSINESS OPPORTUNITY OR CLAIMS OF THIRD PARTIES), AND WHETHER OR NOT THE PARTY HAS BEEN ADVISED OF THE POSSIBILITY OF SUCH DAMAGES. THIS LIMITATION SHALL APPLY NOTWITHSTANDING ANY FAILURE OF ESSENTIAL PURPOSE OF ANY LIMITED REMEDY PROVIDED HEREIN.

9. Should any provision of this Agreement be held by a court of competent jurisdiction to be illegal, invalid, or unenforceable, that provision shall be deemed amended to achieve as nearly as possible the same economic effect as the original provision, and the legality, validity and enforceability of the remaining provisions of this Agreement shall not be affected or impaired thereby.

10. The failure of either party to enforce any term or condition of this Agreement shall not constitute a waiver of either party's right to enforce each and every term and condition of this Agreement. No breach under this agreement shall be deemed waived or excused by either party unless such waiver or consent is in writing signed by the party granting such waiver or consent. The waiver by or consent of a party to a breach of any provision of this Agreement shall not operate or be construed as a waiver of or consent to any other or subsequent breach by such other party.

11. This Agreement may not be assigned (including by operation of law or otherwise) by you without WILEY's prior written consent.

12. These terms and conditions together with CCC's Billing and Payment terms and conditions (which are incorporated herein) form the entire agreement between you and WILEY concerning this licensing transaction and (in the absence of fraud) supersedes all prior agreements and representations of the parties, oral or written. This Agreement may not be amended except in a writing signed by both parties. This Agreement shall be binding upon and inure to the benefit of the parties' successors, legal representatives, and authorized assigns.

13. In the event of any conflict between your obligations established by these terms and conditions and those established by CCC's Billing and Payment terms and conditions, these terms and conditions shall prevail.

14. WILEY expressly reserves all rights not specifically granted in the combination of (i) the license details provided by you and accepted in the course of this licensing transaction, (ii) these terms and conditions and (iii) CCC's Billing and Payment terms and conditions.

15. This Agreement shall be governed by and construed in accordance with the laws of England and you agree to submit to the exclusive jurisdiction of the English courts.

16. Other Terms and Conditions:

BY CLICKING ON THE "I ACCEPT" BUTTON, YOU ACKNOWLEDGE THAT YOU HAVE READ AND FULLY UNDERSTAND EACH OF THE SECTIONS OF AND PROVISIONS SET FORTH IN THIS AGREEMENT AND THAT YOU ARE IN AGREEMENT WITH AND ARE WILLING TO ACCEPT ALL OF YOUR OBLIGATIONS AS SET FORTH IN THIS AGREEMENT.

V1.2

Gratis licenses (referencing $0 in the Total field) are free. Please retain this printable license for your reference. No payment is required.

If you would like to pay for this license now, please remit this license along with your payment made payable to "COPYRIGHT CLEARANCE CENTER" otherwise you will be invoiced within 48 hours of the license date. Payment should be in the form of a check or money order referencing your account number and this invoice number RLNK10797938.
Once you receive your invoice for this order, you may pay your invoice by credit card. Please follow instructions provided at that time.

Make Payment To:
Copyright Clearance Center
Dept 001
P.O. Box 843006
Boston, MA 02284-3006

If you find copyrighted material related to this license will not be used and wish to cancel, please contact us referencing this license number 2445951141970 and noting the reason for cancellation.

Questions? customercare@copyright.com or +1-877-622-5543 (toll free in the US) or +1-978-646-2777.

Appendix A.2:

Permission for the article:
Experimental demonstration of mass-filtered, time-dilated, time-of-flight mass spectrometry. L. T. Demoranville, K. S. Grabowski, D. L. Knies, C. Cetina, Surface and Interface Analysis, 2010, DOI 10.1002/sia.3524

SPRINGER LICENSE
TERMS AND CONDITIONS

Jun 11, 2010

This is a License Agreement between Leonard Demoranville ("You") and Springer ("Springer") provided by Copyright Clearance Center ("CCC"). The license consists of your order details, the terms and conditions provided by Springer, and the payment terms and conditions.

All payments must be made in full to CCC. For payment instructions, please see information listed at the bottom of this form.

License Number	2445970324673
License date	Jun 11, 2010
Licensed content publisher	Springer
Licensed content publication	Journal of Radioanalytical and Nuclear Chemistry
Licensed content title	Testing of mass filtered, time dilated, time-of-flight mass spectrometry
Licensed content author	L. T. Demoranville
Licensed content date	Jan 1, 2009
Volume number	282
Issue number	1
Type of Use	Thesis/Dissertation
Portion	Full text
Number of copies	100
Author of this Springer article	Yes and you are the sole author of the new work
Order reference number	
Title of your thesis / dissertation	Evaluation of mass filtered, time dilated, time-of-flight mass spectrometry
Expected completion date	Aug 2010
Estimated size(pages)	150
Total	0.00 USD
Terms and Conditions	

Introduction
The publisher for this copyrighted material is Springer Science + Business Media. By clicking "accept" in connection with completing this licensing transaction, you agree that the

number(s), and any original (first) copyright notice displayed with material>."

Warranties: Springer Science + Business Media makes no representations or warranties with respect to the licensed material.

Indemnity
You hereby indemnify and agree to hold harmless Springer Science + Business Media and CCC, and their respective officers, directors, employees and agents, from and against any and all claims arising out of your use of the licensed material other than as specifically authorized pursuant to this license.

No Transfer of License
This license is personal to you and may not be sublicensed, assigned, or transferred by you to any other person without Springer Science + Business Media's written permission.

No Amendment Except in Writing
This license may not be amended except in a writing signed by both parties (or, in the case of Springer Science + Business Media, by CCC on Springer Science + Business Media's behalf).

Objection to Contrary Terms
Springer Science + Business Media hereby objects to any terms contained in any purchase order, acknowledgment, check endorsement or other writing prepared by you, which terms are inconsistent with these terms and conditions or CCC's Billing and Payment terms and conditions. These terms and conditions, together with CCC's Billing and Payment terms and conditions (which are incorporated herein), comprise the entire agreement between you and Springer Science + Business Media (and CCC) concerning this licensing transaction. In the event of any conflict between your obligations established by these terms and conditions and those established by CCC's Billing and Payment terms and conditions, these terms and conditions shall control.

Jurisdiction
All disputes that may arise in connection with this present License, or the breach thereof, shall be settled exclusively by the country's law in which the work was originally published.

Other terms and conditions:

v1.2

Gratis licenses (referencing $0 in the Total field) are free. Please retain this printable license for your reference. No payment is required.

If you would like to pay for this license now, please remit this license along with your payment made payable to "COPYRIGHT CLEARANCE CENTER" otherwise you will be invoiced within 48 hours of the license date. Payment should be in the form of a check or money order referencing your account number and this invoice number RLNK10797970.

following terms and conditions apply to this transaction (along with the Billing and Payment terms and conditions established by Copyright Clearance Center, Inc. ("CCC"), at the time that you opened your Rightslink account and that are available at any time at http://myaccount.copyright.com).

Limited License
With reference to your request to reprint in your thesis material on which Springer Science and Business Media control the copyright, permission is granted, free of charge, for the use indicated in your enquiry. Licenses are for one-time use only with a maximum distribution equal to the number that you identified in the licensing process.

This License includes use in an electronic form, provided it is password protected or on the university's intranet, destined to microfilming by UMI and University repository. For any other electronic use, please contact Springer at (permissions.dordrecht@springer.com or permissions.heidelberg@springer.com)

The material can only be used for the purpose of defending your thesis, and with a maximum of 100 extra copies in paper.

Although Springer holds copyright to the material and is entitled to negotiate on rights, this license is only valid, provided permission is also obtained from the (co) author (address is given with the article/chapter) and provided it concerns original material which does not carry references to other sources (if material in question appears with credit to another source, authorization from that source is required as well). Permission free of charge on this occasion does not prejudice any rights we might have to charge for reproduction of our copyrighted material in the future.

Altering/Modifying Material: Not Permitted
However figures and illustrations may be altered minimally to serve your work. Any other abbreviations, additions, deletions and/or any other alterations shall be made only with prior written authorization of the author(s) and/or Springer Science + Business Media. (Please contact Springer at permissions.dordrecht@springer.com or permissions.heidelberg@springer.com)

Reservation of Rights
Springer Science + Business Media reserves all rights not specifically granted in the combination of (i) the license details provided by you and accepted in the course of this licensing transaction, (ii) these terms and conditions and (iii) CCC's Billing and Payment terms and conditions.

Copyright Notice:
Please include the following copyright citation referencing the publication in which the material was originally published. Where wording is within brackets, please include verbatim.
"With kind permission from Springer Science+Business Media: <book/journal title, chapter/article title, volume, year of publication, page, name(s) of author(s), figure

Once you receive your invoice for this order, you may pay your invoice by credit card. Please follow instructions provided at that time.

Make Payment To:
Copyright Clearance Center
Dept 001
P.O. Box 843006
Boston, MA 02284-3006

If you find copyrighted material related to this license will not be used and wish to cancel, please contact us referencing this license number 2445970324673 and noting the reason for cancellation.

Questions? customercare@copyright.com or +1-877-622-5543 (toll free in the US) or +1-978-646-2777.

Appendix B: Data Tables for Chap. 2 Figures

Appendix B.1: Data Table for Fig. 2.1

	Enrichment				Efficiency			
Years	93 %	50 %	5 %	0.7 %	0.5 %	1 %	10 %	50 %
1	206	111	11	2	2000	1000	100	20
6	1235	664	66	9	2000	1000	100	20
10	2059	1107	111	15	2000	1000	100	20
30	6176	3321	332	46	2000	1000	100	20
60	12352	6641	664	93	2000	1000	100	20

Appendix C: Data Tables for Chap. 3 Figures

Appendix C.1: Data Table for Fig. 3.1

Field (G)	m/dm Pretzel	m/dm Traditional	m/dm Total
500	22843	5298	28141
1000	15941	5298	21239
1500	12916	5298	18214
2000	11125	5298	16423
2500	9908	5298	15206
3000	9014	5298	14312
3500	8320	5298	13619
4000	7763	5298	13062
4500	7303	5298	12601
5000	6914	5298	12213
5500	6581	5298	11879
6000	6290	5298	11588
6500	6034	5298	11332
7000	5806	5298	11105
7500	5602	5298	10901
8000	5418	5298	10716
8500	5250	5298	10548
9000	5096	5298	10395
9500	4955	5298	10254
10000	4825	5298	10123
10500	4705	5298	10003
11000	4592	5298	9891
11500	4488	5298	9786
12000	4390	5298	9688
12500	4298	5298	9596
13000	4211	5298	9509
13500	4129	5298	9428
14000	4052	5298	9350
14500	3979	5298	9277
15000	3910	5298	9208
15500	3844	5298	9142
16000	3781	5298	9079
16500	3721	5298	9019

Appendix C.2: Data Table for Fig. 3.2

Mass (u)	m/δm Pretzel	m/δm Traditional	m/δm Total
5	546	765	1311
10	924	1081	2006
15	1258	1325	2582
20	1565	1529	3095
25	1855	1710	3565
30	2130	1873	4003
35	2395	2023	4418
40	2651	2163	4814
45	2899	2294	5193
50	3141	2418	5559
55	3377	2536	5913
60	3608	2649	6257
65	3834	2757	6591
70	4056	2861	6917
75	4274	2962	7236
80	4489	3059	7548
85	4701	3153	7854
90	4910	3244	8154
95	5116	3333	8449
100	5319	3420	8739
105	5520	3504	9024
110	5718	3587	9305
115	5915	3668	9583
120	6109	3746	9856
125	6302	3824	10126
130	6493	3899	10392
135	6682	3974	10655
140	6869	4047	10915
145	7054	4118	11173
150	7239	4189	11427
155	7421	4258	11679
160	7602	4326	11928
165	7782	4393	12175
170	7961	4459	12420
175	8138	4524	12662
180	8314	4588	12903
185	8489	4652	13141
190	8663	4714	13377
195	8836	4776	13612
200	9008	4837	13844
205	9178	4897	14075
210	9348	4956	14304
215	9516	5015	14531
220	9684	5073	14757

225	9851	5130	14981
230	10017	5187	15204
235	10182	5243	15425
240	10346	5298	15645
245	10510	5353	15863
250	10672	5407	16080
255	10834	5461	16295
260	10995	5515	16510
265	11156	5567	16723
270	11315	5620	16935
275	11474	5671	17145
280	11632	5723	17355
285	11790	5774	17563
290	11947	5824	17771
295	12103	5874	17977
300	12258	5924	18182

Appendix C.3: Data Table for Fig. 3.3

Energy (keV)	m/δm Pretzel	m/δm Traditional	m/δm Total
0.5	12219	7493	19712
1	10346	5298	15645
1.5	9387	4326	13713
2	8761	3746	12507
2.5	8304	3351	11655
3	7948	3059	11007
3.5	7660	2832	10492
4	7418	2649	10067
4.5	7211	2498	9709
5	7031	2369	9401
5.5	6872	2259	9131
6	6730	2163	8893
6.5	6602	2078	8680
7	6486	2003	8488
7.5	6379	1935	8314
8	6281	1873	8154
8.5	6190	1817	8008
9	6106	1766	7872
9.5	6027	1719	7746
10	5954	1675	7629
10.5	5884	1635	7519
11	5819	1597	7416
11.5	5757	1562	7320
12	5699	1529	7228
12.5	5643	1499	7142
13	5590	1469	7060
13.5	5540	1442	6982
14	5492	1416	6908
14.5	5446	1391	6837
15	5402	1368	6770
15.5	5359	1346	6705
16	5319	1325	6643
16.5	5279	1304	6584
17	5242	1285	6527
17.5	5205	1267	6472
18	5170	1249	6419
18.5	5136	1232	6368
19	5104	1215	6319
19.5	5072	1200	6272
20	5041	1185	6226

Appendix C.4: Data Table for Fig. 3.4

Length (m)	m/δm Pretzel	m/δm Traditional	m/δm Total
0	10346	0	10346
0.5	10346	1766	12112
1	10346	3532	13878
1.5	10346	5298	15645
2	10346	7064	17411
2.5	10346	8830	19177
3	10346	10596	20943
3.5	10346	12363	22709
4	10346	14129	24475
4.5	10346	15895	26241
5	10346	17661	28007
5.5	10346	19427	29773
6	10346	21193	31539
6.5	10346	22959	33305
7	10346	24725	35071
7.5	10346	26491	36837
8	10346	28257	38604
8.5	10346	30023	40370
9	10346	31789	42136
9.5	10346	33556	43902
10	10346	35322	45668
10.5	10346	37088	47434
11	10346	38854	49200
11.5	10346	40620	50966
12	10346	42386	52732
12.5	10346	44152	54498
13	10346	45918	56264
13.5	10346	47684	58030
14	10346	49450	59797
14.5	10346	51216	61563
15	10346	52982	63329
15.5	10346	54748	65095
16	10346	56515	66861
16.5	10346	58281	68627
17	10346	60047	70393
17.5	10346	61813	72159
18	10346	63579	73925
18.5	10346	65345	75691
19	10346	67111	77457
19.5	10346	68877	79223
20	10346	70643	80989

Appendix D: Data Tables for Chap. 4 Figures

Appendix D.1: Data Table for Fig. 4.1a

Energy (eV)	Number of Ions
0	0
1	13
2	27
3	1399
4	1193
5	1006
6	913
7	718
8	604
9	628
10	427
11	410
12	351
13	274
14	276
15	247
16	219
17	169
18	169
19	142
20	127
21	111
22	89
23	71
24	79
25	44
26	49
27	52
28	40
29	65
30	18
31	21
32	25
33	14
34	10
35	0
36	0
37	0
38	0
39	0

40	0
41	0
42	0
43	0
44	0
45	0
46	0
47	0
48	0
49	0
50	0

Appendix D.2: Data Table for Fig. 4.1b

Emission Angle (Deg.)	Number Ions in Horizontal Angle	Number Ions in Vertical Angle
0	0	0
1	0	0
2	0	0
3	0	0
4	0	0
5	0	0
6	0	0
7	0	0
8	0	0
9	0	0
10	0	0
11	0	0
12	0	0
13	0	0
14	0	0
15	163	163
16	168	156
17	144	167
18	133	171
19	151	141
20	155	147
21	153	155
22	168	148
23	150	165
24	180	175
25	168	163
26	164	160
27	180	168
28	161	160
29	175	175
30	179	174
31	194	182
32	168	168
33	193	163
34	174	184
35	168	174
36	183	177
37	199	150
38	187	192
39	162	170
40	160	196
41	145	197
42	156	181
43	157	170

44	200	213
45	165	183
46	194	176
47	161	188
48	159	180
49	185	185
50	175	183
51	184	186
52	180	170
53	166	163
54	188	162
55	184	158
56	181	169
57	177	197
58	155	190
59	144	161
60	182	185
61	176	179
62	163	160
63	147	142
64	171	157
65	204	164
66	170	167
67	151	171
68	125	109
69	51	47
70	54	30
71	39	46
72	40	46
73	36	34
74	31	33
75	25	16
76	16	23
77	27	20
78	28	35
79	27	20
80	18	15
81	28	19
82	15	16
83	28	21
84	10	12
85	10	16
86	16	14
87	9	12
88	8	14
89	6	3
90	7	3

Appendix D.3: Data Table for Fig. 4.2

Field (kG)	Mass Resolution Uniform Distribution	Error Uniform Distribution	Mass Resolution Based on Gnaser & Verdeil, et al.	Error Gnaser & Verdeil, et al.
4	98.999	3.2330	189.05	13.898
6	96.414	3.3455	155.54	14.542
8	93.107	1.5619	148.28	13.440
10	92.230	2.3971	149.02	17.083
12	89.484	2.3569	149.68	10.856
14	86.489	4.0433	140.94	15.412
16	87.684	2.3599	129.31	16.509

Appendix D.4: Data Table for Fig. 4.4

Field (kG)	Mass Res. ^{208}Pb	Mass Res. $^{208}Pb^{16}O$	Mass Res. Err. $^{208}Pb^{16}O$	Mass Res. ^{232}Th	Mass Res. $^{232}Th^{16}O$	Mass Res. ^{238}U
10	100.42	101.14	3.9282	99.694	99.861	100.440
12	93.838	95.296	4.9157	96.612	96.173	95.215
14	91.920	93.345	4.0050	92.540	92.889	95.305
16	89.187	91.513	4.3754	91.177	92.590	91.529

Appendix D.5: Data Table for Fig. 4.5

Ion Group	Mass Resolution	Error Mass Resolution
1	99.869	5.4750
2	89.326	6.6777
3	102.15	4.7032
4	907.51	60.812
5	913.36	36.505
6	279.18	20.857

Appendix D.6: Data Table for Fig. 4.7

Field (kG)	Mass Res. ^{208}Pb	Mass Res. $^{208}Pb^{16}O$	Mass Res. Err. $^{208}Pb^{16}O$	Mass Res. ^{232}Th	Mass Res. $^{232}Th^{16}O$	Mass Res. ^{238}U
10	894.76	865.18	34.425	864.64	889.3	873.16
12	840.84	855.44	31.839	842.8	851.03	841.15
14	790.41	802.24	35.4	804.38	809.85	819.97
16	783.97	789.82	28.402	794.81	796.38	802.27

Appendix E: Data Tables for Chap. 5 Figures

Appendix E.1: Data Table for Fig. 5.5

Current (nA)	Background Corrected 12 u Count Rate at 5125 G (kHz)	Background Corrected 24 u Count Rate at 3560 G (kHz)
0.001	48	39
0.005	148	75
0.01	178	113
0.015	217	136
0.02	196	144
0.025	158	154
0.03	106	148
0.04	87	140
0.06	60	128
0.08	48	89
0.14	23	83

Appendix E.2: Data Table for Fig. 5.6 and Fig. 5.8

Fig. 4.6 & Fig. 4.8					Fig. 4.6 Uses MCP z axis		Fig. 4.8	
X axis (mm)	Start image (mm)		Z axis (mm)	MCP Position (mm)	End Image (mm)		Z axis (mm)	End Image (mm)
138.2	141.2		200	140			208.13	139.69
138.23	141.2		200.0	140.25			208.11	139.69
138.261	141.2		200.0	139.75			208.11	139.69
138.291	141.2		200.0	140.5			208.12	141.27
138.321	141.2		200.0	139.5			208.12	141.27
138.352	141.2		200.0	140.75			208.09	139.69
138.382	141.2		200.0	139.25			208.09	139.69
138.412	141.2		200.0	141			208.08	139.69
138.442	141.2		200.0	139			208.08	139.69
138.473	141.2		200.0	141.25			208.08	141.27
138.503	141.2		200.0	138.75			208.08	141.27
138.533	141.2		200.1	141.5			208.06	139.69
138.564	141.2		200.1	138.5			208.06	139.69
138.594	141.2		200.1	141.75			207.11	141.27
138.624	141.2		200.1	138.25			207.11	141.27
138.655	141.2		200.2	142			208.04	139.69
138.685	141.2		200.2	138			208.04	139.69
138.715	141.2		200.2	142.25			208.05	141.27
138.745	141.2		200.2	137.75			208.05	141.27
138.776	141.2		200.3	142.5			208.02	139.69
138.806	141.2		200.3	137.5			208.02	139.69
138.836	141.2		200.3	142.75			207.07	141.27
138.867	141.2		200.3	137.25			207.07	141.27

138.897	141.2		200.4	143			206.10	141.27
138.927	141.2		200.4	137			206.10	141.27
138.958	141.2		200.5	143.25			208.01	139.69
138.988	141.2		200.5	136.75			208.01	139.69
139.018	141.2		200.6	143.5			208.01	141.27
139.048	141.2		200.6	136.5			208.01	141.27
139.079	141.2		200.7	143.75			207.99	139.69
139.109	141.2		200.7	136.25			207.99	139.69
139.139	141.2		200.8	144			207.04	141.27
139.17	141.2		200.8	136			207.04	141.27
139.2	141.2		200.9	144.25			206.07	141.27
139.23	141.2		200.9	135.75			206.07	141.27
139.261	141.2		201.0	144.5			207.97	139.69
139.291	141.2		201.0	135.5			207.97	139.69
139.321	141.2		201.2	144.75			207.98	141.27
139.352	141.2		201.2	135.25			207.98	141.27
139.382	141.2		201.3	145			208.02	139.69
139.412	141.2		201.3	135			208.02	139.69
139.442	141.2		201.4	145.25			208.98	139.77
139.473	141.2		201.4	134.75			208.98	139.80
139.503	141.2		201.6	145.5			208.98	139.83
139.533	141.2		201.6	134.5			208.98	139.87
139.564	141.2		201.8	145.75			208.98	139.93
139.594	141.2		201.8	134.25			208.98	140.02
139.624	141.2		202	146			208.98	140.15
139.655	141.2		202	134			208.98	139.77
139.685	141.2		202.1	146.25			208.98	139.80
139.715	141.2		202.1	133.75			208.98	139.83
139.745	141.2		202.4	146.5			208.98	139.87
139.776	141.2		202.4	133.5			208.98	139.93
139.806	141.2		202.6	146.75			208.98	140.02
139.836	141.2		202.6	133.25			208.98	140.15
139.867	141.2		202.8	147			208.98	139.69
139.897	141.2		202.8	133			208.98	139.69
139.927	141.2		203.1	147.25			208.98	139.74
139.958	141.2		203.1	132.75			208.98	139.90
139.988	141.2		203.3	147.5			208.98	139.96
140.018	141.2		203.3	132.5			208.98	139.99
140.048	141.2		203.6	147.75			208.98	140.06
140.079	141.2		203.6	132.25			208.98	140.09
140.109	141.2		204	148			208.98	140.12
140.139	141.2		204	132			208.98	140.28
140.17	141.2		204.3	148.25			208.98	139.74
140.2	141.2		204.3	131.75			208.98	139.90
140.23	141.2		204.7	148.5			208.98	139.96
140.261	141.2		204.7	131.5			208.98	139.99
140.291	141.2		205.1	148.75			208.98	140.06
140.321	141.2		205.1	131.25			208.98	140.09
140.352	141.2		205.6	149			208.98	140.12
140.382	141.2		205.6	131			208.98	140.28
140.412	141.2		206.2	149.25			208.98	139.35
140.442	141.2		206.2	130.75			208.98	139.39

140.473	141.2		206.8	149.5			208.98	139.42
140.503	141.2		206.8	130.5			208.98	139.45
140.533	141.2		207.7	149.75			208.98	139.48
140.564	141.2		207.7	130.25			208.98	139.55
140.594	141.2		210	150			208.98	139.58
140.624	141.2		210	150			208.98	139.61
140.655	141.2		210	130			208.98	139.64
140.685	141.2		210	130			208.98	139.67
140.715	141.2		211.2		143.225		208.98	139.71
140.745	141.2		211.2		143.225		208.98	140.18
140.776	141.2		211.2		143.224		208.98	140.22
140.806	141.2		211.2		143.224		208.98	140.25
140.836	141.2		211.2		143.224		208.98	140.38
140.867	141.2		211.2		143.224		208.98	139.35
140.897	141.2		211.3		143.223		208.98	139.39
140.927	141.2		211.3		143.223		208.98	139.42
140.958	141.2		211.3		143.223		208.98	139.45
140.988	141.2		211.3		143.223		208.98	139.48
141.018	141.2		211.3		143.222		208.98	139.55
141.048	141.2		211.3		143.222		208.98	139.58
141.079	141.2		211.4		143.222		208.98	139.61
141.109	141.2		211.4		143.222		208.98	139.64
141.139	141.2		211.4		143.221		208.98	139.67
141.17	141.2		211.4		143.221		208.98	139.71
141.2	141.2		211.4		143.221		208.98	140.18
138.2	141.2		211.4		143.221		208.98	140.22
138.23	141.2		211.5		143.22		208.98	140.25
138.261	141.2		211.5		143.22		208.98	140.38
138.291	141.2		211.5		143.22		208.98	139.07
138.321	141.2		211.5		143.22		208.98	139.16
138.352	141.2		211.5		143.219		208.98	139.23
138.382	141.2		211.5		143.219		208.98	139.26
138.412	141.2		211.6		143.219		208.98	139.29
138.442	141.2		211.6		143.219		208.98	139.32
138.473	141.2		211.6		143.218		208.98	139.51
138.503	141.2		211.6		143.218		208.98	140.31
138.533	141.2		211.6		143.218		208.98	140.34
138.564	141.2		211.6		143.218		208.98	140.41
138.594	141.2		211.7		143.217		208.98	140.44
138.624	141.2		211.7		143.217		208.98	140.47
138.655	141.2		211.7		143.217		208.98	140.50
138.685	141.2		211.7		143.217		208.98	139.07
138.715	141.2		211.8		143.216		208.98	139.16
138.745	141.2		211.8		143.216		208.98	139.23
138.776	141.2		211.8		143.216		208.98	139.26
138.806	141.2		211.8		143.216		208.98	139.29
138.836	141.2		211.8		143.216		208.98	139.32
138.867	141.2		211.8		143.216		208.98	139.51
138.897	141.2		211.9		143.215		208.98	140.31
138.927	141.2		211.9		143.215		208.98	140.34
138.958	141.2		211.9		143.215		208.98	140.41
138.988	141.2		211.9		143.215		208.98	140.44

139.018	141.2		211.9		143.214		208.98	140.47
139.048	141.2		211.9		143.214		208.98	140.50
139.079	141.2		212.0		143.214		208.98	138.94
139.109	141.2		212.0		143.214		208.98	138.97
139.139	141.2		212.0		143.213		208.98	139.01
139.17	141.2		212.0		143.213		208.98	139.04
139.2	141.2		212.0		143.213		208.98	139.10
139.23	141.2		212.0		143.213		208.98	139.13
139.261	141.2		212.1		143.212		208.98	139.20
139.291	141.2		212.1		143.212		208.98	140.53
139.321	141.2		212.1		143.212		208.98	138.94
139.352	141.2		212.1		143.212		208.98	138.97
139.382	141.2		212.1		143.212		208.98	139.01
139.412	141.2		212.1		143.212		208.98	139.04
139.442	141.2		212.2		143.211		208.98	139.10
139.473	141.2		212.2		143.211		208.98	139.13
139.503	141.2		212.2	149.75			208.98	139.20
139.533	141.2		212.2	130.25			208.98	140.53
139.564	141.2		212.2		143.211		207.00	141.27
139.594	141.2		212.2		143.211		207.00	141.27
139.624	141.2		212.2		143.21		208.98	138.88
139.655	141.2		212.2		143.21		208.98	138.91
139.685	141.2		212.3		143.209		208.98	140.57
139.715	141.2		212.3		143.209		208.98	140.60
139.745	141.2		212.3		143.209		208.98	140.63
139.776	141.2		212.3		143.209		208.98	140.66
139.806	141.2		212.3		143.208		208.98	140.69
139.836	141.2		212.3		143.208		208.98	140.73
139.867	141.2		212.4		143.208		208.98	140.76
139.897	141.2		212.4		143.208		208.98	138.88
139.927	141.2		212.4		143.207		208.98	138.91
139.958	141.2		212.4		143.207		208.98	140.57
139.988	141.2		212.4		143.207		208.98	140.60
140.018	141.2		212.4		143.207		208.98	140.63
140.048	141.2		212.5		143.206		208.98	140.66
140.079	141.2		212.5		143.206		208.98	140.69
140.109	141.2		212.5		143.206		208.98	140.73
140.139	141.2		212.5		143.206		208.98	140.76
140.17	141.2		212.5		143.205		208.98	138.85
140.2	141.2		212.5		143.205		208.98	140.79
140.23	141.2		212.6		143.204		208.98	140.82
140.261	141.2		212.6		143.204		208.98	138.85
140.291	141.2		212.6		143.204		208.98	140.79
140.321	141.2		212.6		143.204		208.98	140.82
140.352	141.2		212.6		143.203		208.98	138.72
140.382	141.2		212.6		143.203		208.98	138.75
140.412	141.2		212.7		143.203		208.98	138.78
140.442	141.2		212.7		143.203		208.98	138.81
140.473	141.2		212.7		143.203		208.98	140.85
140.503	141.2		212.7		143.203		208.98	140.88
140.533	141.2		212.7		143.202		208.98	140.92
140.564	141.2		212.7		143.202		208.98	140.95

140.594	141.2		212.8		143.202	208.98	140.98
140.624	141.2		212.8		143.202	208.98	141.01
140.655	141.2		212.8		143.201	208.98	141.04
140.685	141.2		212.8		143.201	208.98	138.72
140.715	141.2		212.8		143.201	208.98	138.75
140.745	141.2		212.8		143.201	208.98	138.78
140.776	141.2		212.9		143.2	208.98	138.81
140.806	141.2		212.9		143.2	208.98	140.85
140.836	141.2		212.9		143.2	208.98	140.88
140.867	141.2		212.9		143.2	208.98	140.92
140.897	141.2		212.9		139.672	208.98	140.95
140.927	141.2		212.9		139.672	208.98	140.98
140.958	141.2		212.9		139.672	208.98	141.01
140.988	141.2		212.9		139.672	208.98	141.04
141.018	141.2		212.9		143.199	208.98	138.69
141.048	141.2		212.9		143.199	208.98	141.08
141.079	141.2		213.0		139.672	208.98	138.69
141.109	141.2		213.0		139.672	208.98	141.08
141.139	141.2		213.0		139.672	208.98	138.62
141.17	141.2		213.0		139.672	208.98	138.65
141.2	141.2		213.0		143.199	208.98	141.11
138.2	139.7		213.0		143.199	208.98	141.14
138.215	139.7		213.0		139.672	208.98	141.17
138.23	139.7		213.0		139.672	208.98	141.20
138.245	139.7		213.0		139.672	208.98	138.62
138.261	139.7		213.0		139.672	208.98	138.65
138.276	139.7		213.0		143.198	208.98	141.11
138.291	139.7		213.0		143.198	208.98	141.14
138.306	139.7		213.0		139.672	208.98	141.17
138.321	139.7		213.0		139.672	208.98	141.20
138.336	139.7		213.0		139.672	208.98	138.56
138.352	139.7		213.0		139.672	208.98	138.59
138.367	139.7		213.0		143.198	208.98	141.24
138.382	139.7		213.0		143.198	208.98	138.56
138.397	139.7		213.1		139.672	208.98	138.59
138.412	139.7		213.1		139.672	208.98	141.24
138.427	139.7		213.1	149.5		208.98	141.27
138.442	139.7		213.1	130.5		208.98	141.27
138.458	139.7		213.1		139.672	208.98	138.49
138.473	139.7		213.1		139.672	208.98	138.53
138.488	139.7		213.1		143.197	208.98	141.27
138.503	139.7		213.1		143.197	208.98	138.49
138.518	139.7		213.1		139.672	208.98	138.53
138.533	139.7		213.1		139.672	208.98	141.27
138.548	139.7		213.1		139.672	208.98	138.34
138.564	139.7		213.1		139.672	208.98	138.37
138.579	139.7		213.1		143.197	208.98	138.40
138.594	139.7		213.1		143.197	208.98	138.43
138.609	139.7		213.1		139.672	208.98	138.46
138.624	139.7		213.1		139.672	208.98	138.34
138.639	139.7		213.1		139.672	208.98	138.37
138.655	139.7		213.1		139.672	208.98	138.40

138.67	139.7		213.1		143.197	208.98	138.43
138.685	139.7		213.1		143.197	208.98	138.46
138.7	139.7		213.2		139.672	208.98	138.30
138.715	139.7		213.2		139.672	208.98	138.30
138.73	139.7		213.2		139.672	208.98	138.27
138.745	139.7		213.2		139.672	208.98	138.27
138.761	139.7		213.2		143.196	208.98	138.18
138.776	139.7		213.2		143.196	208.98	138.21
138.791	139.7		213.2		139.672	208.98	138.24
138.806	139.7		213.2		139.672	208.98	138.18
138.821	139.7		213.2		139.672	208.98	138.21
138.836	139.7		213.2		139.672	208.98	138.24
138.852	139.7		213.2		143.196	208.98	138.15
138.867	139.7		213.2		143.196	208.98	138.15
138.882	139.7		213.2		139.672	208.98	138.11
138.897	139.7		213.2		139.672	208.98	138.11
138.912	139.7		213.2		139.672	206.03	141.27
138.927	139.7		213.2		139.672	206.03	141.27
138.942	139.7		213.2		143.195	208.00	139.69
138.958	139.7		213.2		143.195	208.00	139.69
138.973	139.7		213.3		139.672	208.96	139.69
138.988	139.7		213.3		139.672	208.96	139.69
139.003	139.7		213.3		139.672	208.01	141.27
139.018	139.7		213.3		139.672	208.01	141.27
139.033	139.7		213.3		143.195	207.99	139.69
139.048	139.7		213.3		143.195	207.99	139.69
139.064	139.7		213.3		139.672	208.94	139.69
139.079	139.7		213.3		139.672	208.94	139.69
139.094	139.7		213.3		139.672	206.97	141.27
139.109	139.7		213.3		139.672	206.97	141.27
139.124	139.7		213.3		143.194	208.95	141.27
139.139	139.7		213.3		143.194	208.95	141.27
139.155	139.7		213.3		139.672	206.00	141.27
139.17	139.7		213.3		139.672	206.00	141.27
139.185	139.7		213.3		139.672	207.97	139.69
139.2	139.7		213.3		139.672	207.97	139.69
139.215	139.7		213.3		143.194	208.92	139.69
139.23	139.7		213.3		143.194	208.92	139.69
139.245	139.7		213.4		139.672	207.97	141.27
139.261	139.7		213.4		139.672	207.97	141.27
139.276	139.7		213.4		139.673	207.95	139.69
139.291	139.7		213.4		139.673	207.95	139.69
139.306	139.7		213.4		143.193	208.91	139.69
139.321	139.7		213.4		143.193	208.91	139.69
139.336	139.7		213.4		139.673	207.00	141.27
139.352	139.7		213.4		139.673	207.00	141.27
139.367	139.7		213.4		139.673	208.91	141.27
139.382	139.7		213.4		139.673	208.91	141.27
139.397	139.7		213.4		143.192	205.96	141.27
139.412	139.7		213.4		143.192	205.96	141.27
139.427	139.7		213.4		139.673	207.93	139.69
139.442	139.7		213.4		139.673	207.93	139.69

139.458	139.7		213.4		139.673	208.89	139.69
139.473	139.7		213.4		139.673	208.89	139.69
139.488	139.7		213.4		143.192	207.94	141.27
139.503	139.7		213.4		143.192	207.94	141.27
139.518	139.7		213.5		139.673	207.92	139.69
139.533	139.7		213.5		139.673	207.92	139.69
139.548	139.7		213.5		139.673	208.87	139.69
139.564	139.7		213.5		139.673	208.87	139.69
139.579	139.7		213.5		143.191	206.97	141.27
139.594	139.7		213.5		143.191	206.97	141.27
139.609	139.7		213.5		139.673	208.87	141.27
139.624	139.7		213.5		139.673	208.87	141.27
139.639	139.7		213.5		139.673	206.00	141.27
139.655	139.7		213.5		139.673	206.00	141.27
139.67	139.7		213.5		143.191	208.85	139.69
139.685	139.7		213.5		143.191	208.85	139.69
139.7	139.7		213.5		139.673	207.90	139.69
138.2	139.7		213.5		139.673	207.90	139.69
138.215	139.7		213.5		139.673	207.90	141.27
138.23	139.7		213.5		139.673	207.90	141.27
138.245	139.7		213.5		143.19	208.84	139.69
138.261	139.7		213.5		143.19	207.88	139.69
138.276	139.7		213.6		139.673	208.84	139.69
138.291	139.7		213.6		139.673	207.88	139.69
138.306	139.7		213.6		139.673	206.93	141.27
138.321	139.7		213.6		139.673	206.93	141.27
138.336	139.7		213.6		143.189	208.84	141.27
138.352	139.7		213.6		143.189	208.84	141.27
138.367	139.7		213.6		139.673	205.96	141.27
138.382	139.7		213.6		139.673	205.96	141.27
138.397	139.7		213.6		139.673	208.82	139.69
138.412	139.7		213.6		139.673	208.82	139.69
138.427	139.7		213.6		143.189	207.86	139.69
138.442	139.7		213.6		143.189	207.86	139.69
138.458	139.7		213.6		139.673	207.87	141.27
138.473	139.7		213.6		139.673	207.87	141.27
138.488	139.7		213.6		139.673	207.85	139.69
138.503	139.7		213.6		139.673	207.85	139.69
138.518	139.7		213.6		143.188	208.80	139.69
138.533	139.7		213.6		143.188	208.80	139.69
138.548	139.7		213.7		139.673	206.90	141.27
138.564	139.7		213.7		139.673	206.90	141.27
138.579	139.7		213.7		139.673	208.81	141.27
138.594	139.7		213.7		139.673	208.81	141.27
138.609	139.7		213.7		143.188	208.78	139.69
138.624	139.7		213.7		143.188	207.83	139.69
138.639	139.7		213.7		139.673	208.78	139.69
138.655	139.7		213.7		139.673	207.83	139.69
138.67	139.7		213.7		139.673	207.83	141.27
138.685	139.7		213.7		139.673	207.83	141.27
138.7	139.7		213.7		143.187	207.81	139.69
138.715	139.7		213.7		143.187	207.81	139.69

138.73	139.7		213.7		139.673		208.77	139.69
138.745	139.7		213.7		139.673		208.77	139.69
138.761	139.7		213.7		139.673		206.86	141.27
138.776	139.7		213.7		139.673		206.86	141.27
138.791	139.7		213.7		143.187		208.77	141.27
138.806	139.7		213.7		143.187		208.77	141.27
138.821	139.7		213.7	149.25			207.79	139.69
138.836	139.7		213.7	130.75			207.79	139.69
138.852	139.7		213.8		139.674		208.75	139.69
138.867	139.7		213.8		139.674		208.75	139.69
138.882	139.7		213.8		139.674		207.80	141.27
138.897	139.7		213.8		139.674		207.80	141.27
138.912	139.7		213.8		143.186		207.78	139.69
138.927	139.7		213.8		143.186		207.78	139.69
138.942	139.7		213.8		139.674		206.83	141.27
138.958	139.7		213.8		139.674		206.83	141.27
138.973	139.7		213.8		139.674		208.73	139.69
138.988	139.7		213.8		139.674		208.73	139.69
139.003	139.7		213.8		143.186		208.74	141.27
139.018	139.7		213.8		143.186		208.74	141.27
139.033	139.7		213.8		139.674		207.76	139.69
139.048	139.7		213.8		139.674		207.76	139.69
139.064	139.7		213.8		139.674		208.71	139.69
139.079	139.7		213.8		139.674		208.71	139.69
139.094	139.7		213.8		143.185		207.76	141.27
139.109	139.7		213.8		143.185		207.76	141.27
139.124	139.7		213.9		139.674		207.74	139.69
139.139	139.7		213.9		139.674		207.74	139.69
139.155	139.7		213.9		139.674		208.70	139.69
139.17	139.7		213.9		139.674		208.70	139.69
139.185	139.7		213.9		143.185		206.79	141.27
139.2	139.7		213.9		143.185		206.79	141.27
139.215	139.7		213.9		139.674		208.70	141.27
139.23	139.7		213.9		139.674		208.70	141.27
139.245	139.7		213.9		139.674		208.68	139.69
139.261	139.7		213.9		139.674		208.68	139.69
139.276	139.7		213.9		143.184		207.72	139.69
139.291	139.7		213.9		143.184		207.72	139.69
139.306	139.7		213.9		139.674		207.73	141.27
139.321	139.7		213.9		139.674		207.73	141.27
139.336	139.7		213.9		139.674		208.66	139.69
139.352	139.7		213.9		139.674		208.66	139.69
139.367	139.7		213.9		143.184		207.71	139.69
139.382	139.7		213.9		143.184		207.71	139.69
139.397	139.7		214.0		139.674		206.76	141.27
139.412	139.7		214.0		139.674		206.76	141.27
139.427	139.7		214.0		139.674		208.67	141.27
139.442	139.7		214.0		139.674		208.67	141.27
139.458	139.7		214.0		143.183		208.64	139.69
139.473	139.7		214.0		143.183		207.69	139.69
139.488	139.7		214.0		139.674		208.64	139.69
139.503	139.7		214.0		139.674		207.69	139.69

139.518	139.7		214.0		139.674	207.69	141.27
139.533	139.7		214.0		139.674	207.69	141.27
139.548	139.7		214.0		143.183	208.63	139.69
139.564	139.7		214.0		143.183	208.63	139.69
139.579	139.7		214.0		139.674	207.67	139.69
139.594	139.7		214.0		139.674	207.67	139.69
139.609	139.7		214.0		139.674	208.63	141.27
139.624	139.7		214.0		139.674	208.63	141.27
139.639	139.7		214.0		143.182	206.72	141.27
139.655	139.7		214.0		143.182	206.72	141.27
139.67	139.7		214.1		139.674	208.61	139.69
139.685	139.7		214.1		139.674	208.61	139.69
139.7	139.7		214.1		139.675	207.65	139.69
138.2	138.2		214.1		139.675	207.65	139.69
138.2	138.23		214.1		143.182	207.66	141.27
138.2	138.26		214.1		143.182	207.66	141.27
138.2	138.29		214.1		139.675	208.59	139.69
138.2	138.32		214.1		139.675	208.59	139.69
138.2	138.35		214.1		139.675	207.64	139.69
138.2	138.38		214.1		139.675	207.64	139.69
138.2	138.41		214.1		143.181	206.69	141.27
138.2	138.44		214.1		143.181	206.69	141.27
138.2	138.47		214.1		139.675	208.60	141.27
138.2	138.50		214.1		139.675	208.60	141.27
138.2	138.53		214.1		139.675	208.57	139.69
138.2	138.56		214.1		139.675	207.62	139.69
138.2	138.59		214.1		143.181	208.57	139.69
138.2	138.62		214.1		143.181	207.62	139.69
138.2	138.65		214.1		139.675	207.62	141.27
138.2	138.68		214.1		139.675	207.62	141.27
138.2	138.71		214.2		139.675	208.56	139.69
138.2	138.74		214.2		139.675	208.56	139.69
138.2	138.77		214.2		143.18	207.60	139.69
138.2	138.80		214.2		143.18	207.60	139.69
138.2	138.83		214.2		139.675	206.65	141.27
138.2	138.86		214.2		139.675	206.65	141.27
138.2	138.89		214.2		139.675	208.56	141.27
138.2	138.92		214.2		139.675	208.56	141.27
138.2	138.95		214.2		143.18	208.54	139.69
138.2	138.98		214.2		143.18	208.54	139.69
138.2	139.01		214.2		139.675	207.58	139.69
138.2	139.04		214.2		139.675	207.58	139.69
138.2	139.07		214.2		139.675	207.59	141.27
138.2	139.10		214.2		139.675	207.59	141.27
138.2	139.13		214.2		143.179	208.52	139.69
138.2	139.17		214.2		143.179	208.52	139.69
138.2	139.2		214.2		139.675	207.57	139.69
138.2	139.23		214.2		139.675	207.57	139.69
138.2	139.26		214.3		139.675	206.62	141.27
138.2	139.29		214.3		139.675	206.62	141.27
138.2	139.32		214.3		143.179	208.53	141.27
138.2	139.35		214.3		143.179	208.53	141.27

138.2	139.38		214.3		139.675		208.51	139.69
138.2	139.41		214.3		139.675		208.51	139.69
138.2	139.44		214.3		139.675		207.55	139.69
138.2	139.47		214.3		139.675		207.55	139.69
138.2	139.50		214.3		143.178		207.55	141.27
138.2	139.53		214.3		143.178		207.55	141.27
138.2	139.56		214.3	149			207.53	139.69
138.2	139.59		214.3	131			207.53	139.69
138.2	139.62		214.3		139.675		208.49	139.69
138.2	139.65		214.3		139.675		208.49	139.69
138.2	139.68		214.3		139.675		206.58	141.27
138.2	139.71		214.3		139.675		206.58	141.27
138.2	139.74		214.3		143.178		208.49	141.27
138.2	139.77		214.3		143.178		208.49	141.27
138.2	139.80		214.3		139.675		207.51	139.69
138.2	139.83		214.3		139.675		207.51	139.69
138.2	139.86		214.4		139.676		208.47	139.69
138.2	139.89		214.4		139.676		208.47	139.69
138.2	139.92		214.4		143.177		207.52	141.27
138.2	139.95		214.4		143.177		207.52	141.27
138.2	139.98		214.4		139.676		207.50	139.69
138.2	140.01		214.4		139.676		207.50	139.69
138.2	140.04		214.4		139.676		208.45	139.69
138.2	140.07		214.4		139.676		208.45	139.69
138.2	140.10		214.4		143.177		206.55	141.27
138.2	140.13		214.4		143.177		206.55	141.27
138.2	140.17		214.4		139.676		208.46	141.27
138.2	140.2		214.4		139.676		208.46	141.27
138.2	140.23		214.4		139.676		207.48	139.69
138.2	140.26		214.4		139.676		207.48	139.69
138.2	140.29		214.4		143.176		208.43	139.69
138.2	140.32		214.4		143.176		208.43	139.69
138.2	140.35		214.4		139.676		207.48	141.27
138.2	140.38		214.4		139.676		207.48	141.27
138.2	140.41		214.5		139.676		207.46	139.69
138.2	140.44		214.5		139.676		207.46	139.69
138.2	140.47		214.5		143.176		208.42	139.69
138.2	140.50		214.5		143.176		208.42	139.69
138.2	140.53		214.5		139.676		206.51	141.27
138.2	140.56		214.5		139.676		206.51	141.27
138.2	140.59		214.5		139.676		208.42	141.27
138.2	140.62		214.5		139.676		208.42	141.27
138.2	140.65		214.5		143.175		207.44	139.69
138.2	140.68		214.5		143.175		207.44	139.69
138.2	140.71		214.5		143.175		208.40	139.69
138.2	140.74		214.5		143.175		208.40	139.69
138.2	140.77		214.5		136.172		207.45	141.27
138.2	140.80		214.5		143.104		207.45	141.27
138.2	140.83		214.5		136.172		207.43	139.69
138.2	140.86		214.5		143.104		207.43	139.69
138.2	140.89		214.5		136.243		208.38	139.69
138.2	140.92		214.5		143.033		208.38	139.69

138.2	140.95		214.5		136.243		206.48	141.27
138.2	140.98		214.5		143.033		206.48	141.27
138.2	141.01		214.5		136.314		208.39	141.27
138.2	141.04		214.5		142.962		208.39	141.27
138.2	141.07		214.5		136.314		208.36	139.69
138.2	141.10		214.5		142.962		207.41	139.69
138.2	141.13		214.5		142.891		208.36	139.69
138.2	141.17		214.5		142.891		207.41	139.69
138.2	141.2		214.5		136.385		207.41	141.27
138.2	138.2		214.5		136.385		207.41	141.27
138.2	138.23		214.5		142.82		208.35	139.69
138.2	138.26		214.5		142.82		207.39	139.69
138.2	138.29		214.5		136.456		208.35	139.69
138.2	138.32		214.5		136.456		207.39	139.69
138.2	138.35		214.5		139.676		206.44	141.27
138.2	138.38		214.5		139.676		206.44	141.27
138.2	138.41		214.5		136.527		208.35	141.27
138.2	138.44		214.5		142.749		208.35	141.27
138.2	138.47		214.5		136.527		208.33	139.69
138.2	138.50		214.5		142.749		208.33	139.69
138.2	138.53		214.5		136.598		207.38	141.27
138.2	138.56		214.5		142.678		207.38	141.27
138.2	138.59		214.5		136.598		208.31	139.69
138.2	138.62		214.5		142.678		208.31	139.69
138.2	138.65		214.5		136.669		206.41	141.27
138.2	138.68		214.5		136.669		206.41	141.27
138.2	138.71		214.5		142.608		208.32	141.27
138.2	138.74		214.5		142.608		208.32	141.27
138.2	138.77		214.5		136.74		208.30	139.69
138.2	138.80		214.5		136.74		208.30	139.69
138.2	138.83		214.5		136.81		207.34	141.27
138.2	138.86		214.5		136.81		207.34	141.27
138.2	138.89		214.5		142.537		208.28	139.69
138.2	138.92		214.5		142.537		208.28	139.69
138.2	138.95		214.5		136.881		206.37	141.27
138.2	138.98		214.5		136.881		206.37	141.27
138.2	139.01		214.5		136.952		208.28	141.27
138.2	139.04		214.5		136.952		208.28	141.27
138.2	139.07		214.5		142.466		208.26	139.69
138.2	139.10		214.5		142.466		208.26	139.69
138.2	139.13		214.5		137.023		207.31	141.27
138.2	139.17		214.5		137.023		207.31	141.27
138.2	139.2		214.5		137.094		208.24	139.69
138.2	139.23		214.5		142.395		208.24	139.69
138.2	139.26		214.5		137.094		206.33	141.27
138.2	139.29		214.5		142.395		206.33	141.27
138.2	139.32		214.5		139.676		208.25	141.27
138.2	139.35		214.5		139.676		208.25	141.27
138.2	139.38		214.5		137.165		208.23	139.69
138.2	139.41		214.5		142.325		208.23	139.69
138.2	139.44		214.5		137.165		207.27	141.27
138.2	139.47		214.5		142.325		207.27	141.27

138.2	139.50		214.5		137.236		208.21	139.69
138.2	139.53		214.5		137.236		208.21	139.69
138.2	139.56		214.5		142.254		206.30	141.27
138.2	139.59		214.5		142.254		206.30	141.27
138.2	139.62		214.5		137.307		208.21	141.27
138.2	139.65		214.5		142.183		208.21	141.27
138.2	139.68		214.5		137.307		208.19	139.69
138.2	139.71		214.5		142.183		208.19	139.69
138.2	139.74		214.5		137.377		207.24	141.27
138.2	139.77		214.5		137.377		207.24	141.27
138.2	139.80		214.5		142.113		208.17	139.69
138.2	139.83		214.5		142.113		208.17	139.69
138.2	139.86		214.5		137.448		206.26	141.27
138.2	139.89		214.5		142.042		206.26	141.27
138.2	139.92		214.5		137.448		208.18	141.27
138.2	139.95		214.5		142.042		208.18	141.27
138.2	139.98		214.5		137.519		208.16	139.69
138.2	140.01		214.5		137.519		208.16	139.69
138.2	140.04		214.5		141.972		207.20	141.27
138.2	140.07		214.5		141.972		207.20	141.27
138.2	140.10		214.5		137.59		208.14	139.69
138.2	140.13		214.5		141.901		208.14	139.69
138.2	140.17		214.5		137.59		206.23	141.27
138.2	140.2		214.5		141.901		206.23	141.27
138.2	140.23		214.5		137.661		208.14	141.27
138.2	140.26		214.5		137.661		208.14	141.27
138.2	140.29		214.5		141.83		208.12	139.69
138.2	140.32		214.5		141.83		208.12	139.69
138.2	140.35		214.5		137.732		207.17	141.27
138.2	140.38		214.5		141.76		207.17	141.27
138.2	140.41		214.5		137.732		208.10	139.69
138.2	140.44		214.5		141.76		208.10	139.69
138.2	140.47		214.5		137.802		206.19	141.27
138.2	140.50		214.5		137.802		206.19	141.27
138.2	140.53		214.5		137.873		208.11	141.27
138.2	140.56		214.5		141.689		208.11	141.27
138.2	140.59		214.5		137.873		208.09	139.69
138.2	140.62		214.5		141.689		208.09	139.69
138.2	140.65		214.5		141.618		207.13	141.27
138.2	140.68		214.5		141.618		207.13	141.27
138.2	140.71		214.5		139.676		208.07	139.69
138.2	140.74		214.5		139.676		208.07	139.69
138.2	140.77		214.5		137.944		206.16	141.27
138.2	140.80		214.5		141.548		206.16	141.27
138.2	140.83		214.5		137.944		208.07	141.27
138.2	140.86		214.5		141.548		208.07	141.27
138.2	140.89		214.5		138.015		207.10	141.27
138.2	140.92		214.5		141.477		207.10	141.27
138.2	140.95		214.5		138.015		206.12	141.27
138.2	140.98		214.5		141.477		206.12	141.27
138.2	141.01		214.5		141.407		207.06	141.27
138.2	141.04		214.5		141.407		207.06	141.27

138.2	141.07		214.5		138.085		206.09	141.27
138.2	141.10		214.5		141.336		206.09	141.27
138.2	141.13		214.5		138.085		206.05	141.27
138.2	141.17		214.5		141.336		206.05	141.27
138.2	141.2		214.5		138.156		208.13	139.69
			214.5		141.265		208.13	139.69
			214.5		138.156		208.11	139.69
			214.5		141.265		208.11	139.69
			214.5		141.124		208.12	141.27
			214.5		141.195		208.12	141.27
			214.5		141.124		208.09	139.69
			214.5		141.195		208.09	139.69
			214.5		138.227		208.08	139.69
			214.5		141.053		208.08	139.69
			214.5		138.227		208.08	141.27
			214.5		141.053		208.08	141.27
			214.5		138.298		208.06	139.69
			214.5		140.983		208.06	139.69
			214.5		138.298		207.11	141.27
			214.5		140.983		207.11	141.27
			214.5		138.369		208.04	139.69
			214.5		140.912		208.04	139.69
			214.5		138.369		208.05	141.27
			214.5		140.912		208.05	141.27
			214.6		138.439		208.02	139.69
			214.6		140.771		208.02	139.69
			214.6		140.841		207.07	141.27
			214.6		138.439		207.07	141.27
			214.6		140.771		206.10	141.27
			214.6		140.841		206.10	141.27
			214.6		138.51		208.01	139.69
			214.6		138.581		208.01	139.69
			214.6		140.7		208.01	141.27
			214.6		138.51		208.01	141.27
			214.6		138.581		207.99	139.69
			214.6		140.7		207.99	139.69
			214.6		138.651		207.04	141.27
			214.6		140.63		207.04	141.27
			214.6		138.651		206.07	141.27
			214.6		140.63		206.07	141.27
			214.6		138.722		207.97	139.69
			214.6		138.793		207.97	139.69
			214.6		140.559		207.98	141.27
			214.6		138.722		207.98	141.27
			214.6		138.793		208.02	139.69
			214.6		140.559		208.02	139.69
			214.6		138.863		208.98	139.77
			214.6		138.934		208.98	139.80
			214.6		139.005		208.98	139.83
			214.6		139.076		208.98	139.87
			214.6		140.418		208.98	139.93
			214.6		140.488		208.98	140.02

			214.6		138.863		208.98	140.15
			214.6		138.934		208.98	139.77
			214.6		139.005		208.98	139.80
			214.6		139.076		208.98	139.83
			214.6		140.418		208.98	139.87
			214.6		140.488		208.98	139.93
			214.6		139.146		208.98	140.02
			214.6		139.217		208.98	140.15
			214.6		139.288		208.98	139.69
			214.6		139.358		208.98	139.69
			214.6		139.146		208.98	139.74
			214.6		139.217		208.98	139.90
			214.6		139.288		208.98	139.96
			214.6		139.358		208.98	139.99
			214.6		139.429		208.98	140.06
			214.6		139.5		208.98	140.09
			214.6		139.57		208.98	140.12
			214.6		139.641		208.98	140.28
			214.6		140.347		208.98	139.74
			214.6		139.429		208.98	139.90
			214.6		139.5		208.98	139.96
			214.6		139.57		208.98	139.99
			214.6		139.641		208.98	140.06
			214.6		140.347		208.98	140.09
			214.6		139.676		208.98	140.12
			214.6		139.676		208.98	140.28
			214.6		139.712		208.98	139.35
			214.6		139.782		208.98	139.39
			214.6		139.853		208.98	139.42
			214.6		139.923		208.98	139.45
			214.6		140.206		208.98	139.48
			214.6		140.277		208.98	139.55
			214.6		139.712		208.98	139.58
			214.6		139.782		208.98	139.61
			214.6		139.853		208.98	139.64
			214.6		139.923		208.98	139.67
			214.6		140.206		208.98	139.71
			214.6		140.277		208.98	140.18
			214.6		139.994		208.98	140.22
			214.6		140.065		208.98	140.25
			214.6		140.135		208.98	140.38
			214.6		139.994		208.98	139.35
			214.6		140.065		208.98	139.39
			214.6		140.135		208.98	139.42
			214.8	148.75			208.98	139.45
			214.8	131.25			208.98	139.48
			215.2	148.5			208.98	139.55
			215.2	131.5			208.98	139.58
			215.6	148.25			208.98	139.61
			215.6	131.75			208.98	139.64
			216	148			208.98	139.67
			216	132			208.98	139.71

			216.3	147.75			208.98	140.18
			216.3	132.25			208.98	140.22
			216.6	147.5			208.98	140.25
			216.6	132.5			208.98	140.38
			216.8	147.25			208.98	139.07
			216.8	132.75			208.98	139.16
			217.1	147			208.98	139.23
			217.1	133			208.98	139.26
			217.3	146.75			208.98	139.29
			217.3	133.25			208.98	139.32
			217.5	146.5			208.98	139.51
			217.5	133.5			208.98	140.31
			217.8	146.25			208.98	140.34
			217.8	133.75			208.98	140.41
			218	146			208.98	140.44
			218	134			208.98	140.47
			218.1	145.75			208.98	140.50
			218.1	134.25			208.98	139.07
			218.3	145.5			208.98	139.16
			218.3	134.5			208.98	139.23
			218.5	145.25			208.98	139.26
			218.5	134.75			208.98	139.29
			218.6	145			208.98	139.32
			218.6	135			208.98	139.51
			218.7	144.75			208.98	140.31
			218.7	135.25			208.98	140.34
			218.9	144.5			208.98	140.41
			218.9	135.5			208.98	140.44
			219.0	144.25			208.98	140.47
			219.0	135.75			208.98	140.50
			219.1	144			208.98	138.94
			219.1	136			208.98	138.97
			219.2	143.75			208.98	139.01
			219.2	136.25			208.98	139.04
			219.3	143.5			208.98	139.10
			219.3	136.5			208.98	139.13
			219.4	143.25			208.98	139.20
			219.4	136.75			208.98	140.53
			219.5	143			208.98	138.94
			219.5	137			208.98	138.97
			219.6	142.75			208.98	139.01
			219.6	137.25			208.98	139.04
			219.6	142.5			208.98	139.10
			219.6	137.5			208.98	139.13
			219.7	142.25			208.98	139.20
			219.7	137.75			208.98	140.53
			219.7	142			207.00	141.27
			219.7	138			207.00	141.27
			219.8	141.75			208.98	138.88
			219.8	138.25			208.98	138.91
			219.8	141.5			208.98	140.57
			219.8	138.5			208.98	140.60

			219.9	141.25			208.98	140.63
			219.9	138.75			208.98	140.66
			219.9	141			208.98	140.69
			219.9	139			208.98	140.73
			219.9	140.75			208.98	140.76
			219.9	139.25			208.98	138.88
			219.9	140.5			208.98	138.91
			219.9	139.5			208.98	140.57
			219.9	140.25			208.98	140.60
			219.9	139.75			208.98	140.63
			220	140			208.98	140.66

Appendix F: Data Tables for Chap. 6 Figures

Appendix F.1: Data Table for Fig. 6.7

Square Root Mass	Time 4 kG (ns)	Time 6 kG (ns)	Time 8 kG (ns)	Time 10 kG (ns)	Time 12 kG (ns)	Time 14 kG (ns)	Time 16 kG (ns)
3.4641	16659	16040	15682	15441	15262	15125	15015
4.0000	19358	18581	18134	17835	17615	17442	17301
4.3589	21192	20311	19795	19457	19204		18853
4.8990	23996	22950	22340	21933	21633	21396	21204
5.0990	25051	23941	23291	22858	22539	22289	22084
5.6569	27995	26707	25944	25438	25065	24771	24531
5.9161	29392	28017	27201	26657	26257	25944	25687
6.0828	30296	28864	28014	27447	27027	26699	26430
6.9282	34967	33217	32188	31494	30983	30583	30256
7.7460	39559	37485	36262	35445	34847	34374	33985
8.4853		41432		39086	38410	37865	37415
8.7178			41206	40226	39524	38959	38490
9.7980							43591
10.954						49762	49102
11.662						53238	52516
14.213						65121	64156

Appendix F.2: Data Table for Fig. 6.8

Mass (u)	Time 4 kG ($*10^{-5}$ s)	Time 6 kG ($*10^{-5}$ s)	Time 8 kG ($*10^{-5}$ s)	Time 10 kG ($*10^{-5}$ s)	Time 12 kG ($*10^{-5}$ s)	Time 14 kG ($*10^{-5}$ s)	Time 16 kG ($*10^{-5}$ s)
12	1.67	1.60	1.57	1.54	1.53	1.51	1.50
16	1.94	1.86	1.81	1.78	1.76	1.74	1.73
19	2.12	2.03	1.98	1.95	1.92		1.89
24	2.40	2.30	2.23	2.19	2.16	2.14	2.12
26	2.51	2.39	2.33	2.29	2.25	2.23	2.21
32	2.80	2.67	2.59	2.54	2.51	2.48	2.45
35	2.94	2.80	2.72	2.67	2.63	2.59	2.57
37	3.03	2.89	2.80	2.74	2.70	2.67	2.64
48	3.50	3.32	3.22	3.15	3.10	3.06	3.03
60	3.96	3.75	3.63	3.54	3.48	3.44	3.40
72		4.14		3.91	3.84	3.79	3.74
76			4.12	4.02	3.95	3.90	3.85

Appendix F.3: Data Table for Fig. 6.12

Field (kG)	Res. Both 16u	Res. 12u	Res. Err. 12u	Res. 16u	Res. 36u	Res. 60u	Res. 96u	Res. 156u	Res. Err. 156u
4	172	194	16.6	188	276	305			
6	149	179	20.7	169	238	260	293		
8	154	169	21.1	168	218	239	249		
10	161	169	20.9	178	209	229	238	234	12.8
12	165	181	17.9	178	201	219	224	214	10.4
14	166	184	15.2	179	191	210	216	206	3.1
16	161	172	19.9	174	180	209	215	206	3.1

Appendix F.4: Data Table for Fig. 6.13

Field (kG)	Res. Both 16u	Res. 16u	Res. Err. 16 u	Res. 28u	Res. 56u	Res. 76u	Res. 105u	Res. Err. 105u	Gnaser/ Verdiel Sim. Res. 28u	Uni. Dist. Sim. Res. 28u
4	172	149	22.9	158	238				189	98.9
6	149	120	31.4	120	221	274	318	74.6	155	96.4
8	154	134	18.4	97	196	243	313	68.3	148	93.1
10	161	141	16.2	107	166	217	281	64.2	149	92.2
12	165	144	13.5	107	139	200	262	57.2	149	89.4
14	166	147	13.7	104	146	203	260	62.3	140	86.4
16	161	149	16.3	101	148	205	251	56.2	129	87.6

Appendix F.5: Data Table for Fig. 6.14

Mass (u)	Mass Resolution, Graphite Mass Spectra	Mass Resolution Error, Graphite Mass Spectra	Mass Resolution, Graphite Time Spectra
12	169.3	20.9	
16	178	12.7	140.82
28			106.39
36	209.1	14.3	
56			165.76
60	229.9	18.3	
76			215.98
96	238.2	27.6	
105			283.11
157	234.6	12.8	

Appendix G: Sample SIMION Geometry File

Appendix G.1: Geometry file for reflectron ion mirror

```
;6 way cross reflectron assembly model
;
PA_Define(300,300,300,planar,none,electrostatic)
Locate(0,0,0,1,0,0,0)
{
;outer beam tube along z axis
Locate(139.7,139.7,0)
{
        electrode (0)
        {
                Fill{within{cylinder(0,0,279.4,79,79,279.4)} }
        }
}
;outer beam tube along x axis
Locate(0,139.7,139.7,1,90,0,0)
{
        electrode (0)
        {
                Fill{within{cylinder(0,0,279.4,79,79,279.4)} }
        }
}
;outer beam tube along y axis
Locate(139.7,0,139.7,1,0,0,270)
{
        electrode (0)
        {
                Fill{within{cylinder(0,0,279.4,79,79,279.4)} }
        }
}
;inner beam tube along z axis
Locate(139.7,139.7,0)
{
        non_electrode ()
        {
                Fill{within{cylinder(0,0,279.4,73.4,73.4,279.4)} }
        }
}
;inner beam tube along x axis
Locate(0,139.7,139.7,1,90,0,0)
{
        non_electrode ()
```

```
	{
		Fill{within{cylinder(0,0,279.4,73.4,73.4,279.4)} }
	}
}
;inner beam tube along y axis
Locate(139.7,0,139.7,1,0,0,270)
{
	non_electrode ()
	{
		Fill{within{cylinder(0,0,279.4,73.4,73.4,279.4)} }
	}
}
;rear reflectron plate
Locate(139.7,139.7,107.7,1,45,,)
{
	electrode(1)
	{
		Fill{Within{cylinder(0,0,3.175,80,54,3.175)} }
	}
}
;halo electrode
Locate(118.5,139.7,88.5,1,45,,)
{
	electrode(2)
	{
		Fill{Within{cylinder(0,0,3.175,100,54,3.175)} }
	}
}
Locate(118.5,139.7,88.5,1,45,,)
{
	non_electrode()
	{
		Fill{Within{cylinder(0,0,3.175,70,34,3.175)} }
	}
}
;front reflectron plate
Locate(97.3,139.7,67.3,1,45,,)
{
	electrode(3)
	{
		Fill{Within{cylinder(0,0,3.175,100,54,3.175)} }
	}
}
;faraday cup suppressor
Locate(139.7,139.7,139.7,1,45,,)
{
```

```
	electrode(5)
	{
		Fill{Within{Cylinder(0,0,0,28,28,3.175)} }
	}
}
;Center beam path
Locate(139.7,139.7,0)
{
	non_electrode ()
	{
		Fill{within{cylinder(0,0,279.4,14,14,279.4)} }
	}
}
;MCP
Locate(45,139.7,109.7,1,270,0,0)
{
	electrode (4)
	{
		Fill{within{cylinder(0,0,20,10,10,16)} }
	}
}
;MCP beam path
Locate(50,139.7,109.7,1,270,0,0)
{
	non_electrode ()
	{
		Fill{within{cylinder(0,0,0,8,8,15)} }
	}
}
;faraday cup
Locate(148.6,139.7,148.6,1,45,,)
{
	electrode(6)
	{
		Fill{Within{cylinder(0,0,0,28,28,3.175)} }
	}
}
}
```

Bibliography

BENNINGHOVEN, A., F.G. RÜDENAUER, AND H.W. WERNER. 1987. Secondary Ion Mass Spectrometry: Basic Concepts, Instrumental Aspects, Applications and Trends. J. Wiley, New York.

BETTI, M., G. TAMBORINI, AND L. KOCH. 1999. Use of secondary ion mass spectrometry in nuclear forensic analysis for the characterization of plutonium and highly enriched uranium particles. *Anal. Chem* 71: 2616–2622.

BOXER, S.G., M.L. KRAFT, AND P.K. WEBER. 2009. Advances in Imaging Secondary Ion Mass Spectrometry for Biological Samples. *Annual Review of Biophysics* 38: 53-74.

BROCK, A., N. RODRIGUEZ, AND R.N. ZARE. 2000. Characterization of a Hadamard transform time-of-flight mass spectrometer. *Review of Scientific Instruments* 71: 1306.

BROCK, A., N. RODRIGUEZ, AND R.N. ZARE. 1998. Hadamard Transform Time-of-Flight Mass Spectrometry. *Analytical Chemistry* 70: 3735-3741.

CETINA, C., L.T. DEMORANVILLE, K.S. GRABOWSKI, AND D.L. KNIES. 2010. Evaluation of Standards for Silicon Analysis in Germanium Genesis Collectors by SIMS-AMS. *In* Lunar and Planetary Institute Science Conference Abstracts, 2729.

CETINA, C., K.S. GRABOWSKI, AND D.L. KNIES. 2009. SIMS-AMS Method for Measuring Solar Wind Silicon in DLC Genesis Collectors. *In* Lunar and Planetary Institute Science Conference Abstracts, 2550.

CETINA, C., K.S. GRABOWSKI, D.L. KNIES, AND L.T. DEMORANVILLE. 2008. SIMS-AMS depth profiles for NASA Genesis samples: Preliminary measurements. *Applied Surface Science* 255: 1479–1481.

CETINA, C., D.L. KNIES, K.S. GRABOWSKI, A.D. BERRY, AND R.L. MOWERY. 2007. Nanogram amounts of selected rare earth elements measured by AMS. *Nuclear Instruments and Methods in Physics Research Section B: Beam Interactions with Materials and Atoms* 259: 188–193.

CETINA, C. ET AL. 2003. A microchannel plate system for accelerator mass spectrometry measurements. *Nuclear Instruments and Methods in Physics Research Section A: Accelerators, Spectrometers, Detectors and Associated Equipment* 513: 403-407.

CHAIT, B., AND K. STANDING. 1981. A time-of-flight mass spectrometer for measurement of secondary ion mass spectra. *International Journal of Mass Spectrometry and Ion Physics* 40: 185-193.

COTTER, R. 1997. Time-of-flight mass spectrometry : instrumentation and applications in biological research. American Chemical Society, Washington DC.

DATAR, S.A. ET AL. 2000. High sensitivity measurement of implanted As in the presence of Ge in Ge[sub x]Si[sub 1−x]/Si layered alloys using trace element accelerator mass spectrometry. *Applied Physics Letters* 77: 3974.

DEMORANVILLE, L.T., K.S. GRABOWSKI, D.L. KNIES, AND C. CETINA. 2010. Experimental demonstration of mass-filtered, time-dilated, time-of-flight mass spectrometry. *Surface and Interface Analysis*.

DEMORANVILLE, L., D. KNIES, K. GRABOWSKI, AND A. MIGNEREY. 2009. Testing of mass filtered, time dilated, time-of-flight mass spectrometry. *Journal of Radioanalytical and Nuclear Chemistry* 282: 305-308.

DESGRANGES, L., C. VALOT, AND B. PASQUET. 2006. Characterisation of irradiated nuclear fuel with SIMS. *Applied Surface Science* 252: 7048–7050.

ENDER, R.M., M. DÖBELI, M. SUTER, AND H. SYNAL. 1997a. Accelerator SIMS at PSI/ETH Zurich. *Nuclear Instruments and Methods in Physics Research Section B: Beam Interactions with Materials and Atoms* 123: 575-578.

ENDER, R.M., M. DÖBELI, M. SUTER, AND H. SYNAL. 1997b. Characterization of the accelerator SIMS setup at PSI/ETH Zurich. *In* J. Duggan, and I. L. Morgan [eds.], The fourteenth international conference on the application of accelerators in research and industry, 819-822. AIP, Denton, Texas (USA). Available at: http://link.aip.org/link/?APC/392/819/1 [Accessed July 9, 2010].

ENGE, H. 1963. Achromatic Magnetic Mirror for Ion Beams. *Review of Scientific Instruments* 34: 385-&.

ERDMANN, N. ET AL. 2000. Production of monodisperse uranium oxide particles and their characterization by scanning electron microscopy and secondary ion mass spectrometry. *Spectrochimica Acta Part B: Atomic Spectroscopy* 55: 1565-1575.

ESAKA, F. ET AL. 2007. Particle isolation for analysis of uranium minor isotopes in individual particles by secondary ion mass spectrometry. *Talanta* 71: 1011-1015.

FERNÁNDEZ, F.M. ET AL. 2002. Hadamard Transform Time-of-Flight Mass Spectrometry: A High-Speed Detector for Capillary-Format Separations. *Analytical Chemistry* 74: 1611-1617.

FIFIELD, L.K. 1996. Accelerator mass spectrometry, large and small. *Nuclear Instruments and Methods in Physics Research Section A: Accelerators, Spectrometers, Detectors and Associated Equipment* 382: 292-298.

FLETCHER, J. 2009. Cellular imaging with secondary ion mass spectrometry. *ANALYST* 134: 2204-2215.

GNASER, H. 2007. Energy and Angular Distributions of Sputtered Species. *In* Sputtering by Particle Bombardment, 231-328. Available at: http://dx.doi.org/10.1007/978-3-540-44502-9_5 [Accessed June 7, 2010].

GNASER, H. 2000. Negative cluster ions in sputtering of Si, SiC and graphite: Abundance distributions, energy spectra and fragmentation processes. *Nuclear Instruments and Methods in Physics Research Section B: Beam Interactions with Materials and Atoms* 164-165: 705-714.

GOVE, H.E. 1999. From Hiroshima to the iceman: the development and applications of accelerator mass spectrometry. CRC Press.

GRABOWSKI, K.S., D.L. KNIES, T.M. DETURCK, D.J. TREACY, AND OTHERS. 2000. A report on the Naval Research Laboratory AMS facility. *Nuclear Instruments and Methods in Physics Research Section B: Beam Interactions with Materials and Atoms* 172: 34–39.

GRABOWSKI, K.S., D.L. KNIES, G.K. HUBLER, AND H.A. ENGE. 1997. A new accelerator mass spectrometer for trace element analysis at the Naval Research Laboratory. *Nuclear Instruments and Methods in Physics Research Section B: Beam Interactions with Materials and Atoms* 123: 566–570.

GUILHAUS, M., D. SELBY, AND V. MLYNSKI. 2000. Orthogonal acceleration time-of-flight mass spectrometry. *Mass Spectrometry Reviews* 19: 65-107.

HOU, X., W. CHEN, Y. HE, AND B.T. JONES. 2005. Analytical Atomic Spectrometry for Nuclear Forensics. *Applied Spectroscopy Reviews* 40: 245 - 267.

KALLIO, A.P. ET AL. 2008. Oxygen Isotope Analysis of a Genesis Solar Wind Concentrator Sample With MegaSIMS. *In* AGU Spring Meeting Abstracts, 05.

KARATAEV, V., B. MAMYRIN, AND D. SHMIKK. 1972. New method for focusing ion bunches in time-of-flight mass spectrometers. *Soviet Physics - Technical Physics* 16: 1177-1179.

KATTA, V., AND B. CHAIT. 1991. A pulsed ion-bombardment Time-of-Flight mass spectrometer with high-sensitivity for the analysis of peptides. *International Journal of Mass Spectrometry and Ion Processes* 105: 129-145.

KNIES, D.L., K.S. GRABOWSKI, AND C. CETINA. 2007. Ion optic calculations and installation of a modified SIMS ion source. *Nuclear Instruments and Methods in Physics Research Section B: Beam Interactions with Materials and Atoms* 259: 118–122.

KNIES, D.L., K.S. GRABOWSKI, AND C. CETINA. 2006. Implementing a SIMS ion source on the NRL trace element accelerator mass spectrometer. *Applied Surface Science* 252: 7297–7300.

KNIES, D.L., K.S. GRABOWSKI, C. CETINA, G.K. HUBLER, M. GETANEH, AND S.J. TUMEY. 2004. Status report of the NRL TEAMS facility. *Nuclear Instruments and Methods in Physics Research Section B: Beam Interactions with Materials and Atoms* 223: 72–77.

KNIES, D.L., K.S. GRABOWSKI, G.K. HUBLER, AND H.A. ENGE. 1997. 1-200 amu tunable Pretzel magnet notch-mass-filter and injector for trace element accelerator mass spectrometry. *Nuclear Instruments and Methods in Physics Research Section B: Beam Interactions with Materials and Atoms* 123: 589-593.

LEHTO, S. 2002. Development of a SIMS method for isotopic analysis of uranium containing particles.

MA, C., S.M. MICHAEL, M. CHIEN, J. ZHU, AND D.M. LUBMAN. 1992. The design of an atmospheric pressure ionization/time-of-flight mass spectrometer using a beam deflection method. *Review of Scientific Instruments* 63: 139.

MADEN, C. 2003. The potential of accelerator secondary ion mass spectrometry in environmental sciences. Swiss Federal Insititute of Technology Zurich.

MADEN, C., M. DÖBELI, B. HOFMANN, AND M. SUTER. 2004. In-situ Ir concentration measurements in KT-boundary sediments by accelerator secondary ion mass spectrometry. *Nuclear Instruments and Methods in Physics Research Section B: Beam Interactions with Materials and Atoms* 219: 176–180.

MADEN, C., M.D. PSI, AND B. HOFMANN. 2001. Investigation of Platinum Group Elements at the Cretaceous-Teriary Boundary with Accelerator SIMS. ETH. Available at: http://www.ipp.phys.ethz.ch/research/experiments/tandem/Annual/2001/27.pdf.

MAHONEY, C. 2010. Cluster Secondary Ion Mass Spectrometry of Polymers and Related Materials. *Mass Spectrometry Reviews* 29: 247-293.

MAMYRIN, B.A., V. KARATAEV, D.V. SHMIKK, AND V. ZAGULIN. 1973. Mass-reflectron a New Nonmagnetic Time-of-Flight High-Resolution Mass-Spectrometer. *Zhurnal Eksperimentalnoi I Teoreticheskoi Fiziki* 64: 82-89.

MAMYRIN, B.A. 2001. Time-of-flight mass spectrometry (concepts, achievements, and prospects). *International Journal of Mass Spectrometry* 206: 251-266.

MANURA, D.J., AND D. DAHL. 2008. SIMION Version 8.0 user Manual. Scientific Instrument Services, USA, Ringoes, NJ.

MAO, P.H., D.S. BURNETT, C.D. COATH, G. JARZEBINSKI, T. KUNIHIRO, AND K.D. MCKEEGAN. 2008. MegaSIMS: a SIMS/AMS hybrid for measurement of the Sun's oxygen isotopic composition. *Applied Surface Science* 255: 1461–1464.

MAO, P.H., T. KUNIHIRO, K.D. MCKEEGAN, C.D. COATH, G. JARZEBINSKI, AND D.S. BURNETT. 2006. MegaSIMS Update: Oxygen Transmission, Destruction of OH Molecular Ions, and Stability of Three-Isotope Measurements. *In* 37th Annual Lunar and Planetary Science Conference, 2153.

MAY, M. ET AL. 2008. Nuclear Forensics: Role, State of the Art, Program Needs. American Physical Society and American Association for the Advancement of Science, USA.

MAYER, K., AND M. WALLENIUS. 2008. Nuclear Forensic Methods in Safeguards. *Esarda Bulletin* 38: 44-51.

MCDANIEL, F.D., S.A. DATAR, B.N. GUO, S.N. RENFROW, Z.Y. ZHAO, AND J.M. ANTHONY. 1998. Low-level copper concentration measurements in silicon wafers using trace-element accelerator mass spectrometry. *Applied Physics Letters* 72: 3008.

MCDANIEL, F.D. ET AL. 1993. Trace element analysis by accelerator mass spectrometry. *Journal of Radioanalytical and Nuclear Chemistry Articles* 167: 423-432.

MCDANIEL, F. ET AL. 1992. Radionuclide dating and trace element analysis by accelerator mass spectrometry. *Journal of Radioanalytical and Nuclear Chemistry* 160: 119-140.

MCKEEGAN, K.D. ET AL. 2010. Genesis SiC Concentrator Sample Traverse: Confirmation of 16O-Depletion of Terrestrial Oxygen. *In* Lunar and Planetary Institute Science Conference Abstracts, 2729.

MCKEEGAN, K.D. ET AL. 2009. Performance Characteristics of the MegaSIMS for Isotopic Analysis of Captured Solar Wind. *In* AGU Fall Meeting Abstracts, 04.

MCKEEGAN, K.D., C.D. COATH, G. JARZEBINSKI, T. KUNIHIRO, AND P.H. MAO. 2005. MegaSIMS: A High Energy Secondary Ion Mass Spectrometer for the Analysis of Captured Solar Wind. *Microscopy and Microanalysis* 11: 1376–1377.

MIDDLETON, R. 1990. A Negative Ion Cookbook. Available at: www.pelletron.com/cookbook.pdf.

MOODY, K.J., I.D. HUTCHEON, AND P.M. GRANT. 2005. Nuclear forensic analysis. CRC Press.

MYERS, D., G. LI, P. YANG, AND G. HIEFTJE. 1994. An inductively coupled plasma--time-of-flight mass spectrometer for elemental analysis. Part I: Optimization and characteristics. *Journal of the American Society for Mass Spectrometry* 5: 1008-1016.

NATIONAL INSTRUMENTS. 2003. Labview. National Instruments. Available at: http://www.ni.com/labview/ [Accessed August 2, 2010].

PAJO, L. 2001. UO2 fuel pellet impurities, pellet surface roughness n (18 O)/n (16 O) ratios, applied to nuclear forensic science. University of Helsinki.

PAJO, L., G. TAMBORINI, G. RASMUSSEN, K. MAYER, AND L. KOCH. 2001. A novel isotope analysis of oxygen in uranium oxides: comparison of secondary ion mass spectrometry, glow discharge mass spectrometry and thermal ionization mass spectrometry. *Spectrochimica Acta Part B: Atomic Spectroscopy* 56: 541-549.

PIEL, N., H.W. BECKER, J. MEIJER, W.H. SCHULTE, AND C. ROLFS. 1999. Production of short ion pulses for TOF-RBS. *Nuclear Instruments and Methods in Physics Research Section A: Accelerators, Spectrometers, Detectors and Associated Equipment* 437: 521–530.

RANEBO, Y., N. NIAGOLOVA, N. ERDMANN, M. ERIKSSON, G. TAMBORINI, AND M. BETTI. 2010. Production and Characterization of Monodisperse Plutonium, Uranium, and Mixed Uranium−Plutonium Particles for Nuclear Safeguard Applications. *Analytical Chemistry* 82: 4055-4062.

RATHMANN, D., N. EXELER, AND B. WILLERDING. 1985. Ion beam pulsing for time of flight (TOF) experiments. *Journal of Physics E: Scientific Instruments* 18: 17.

RAY, S.J., AND G.M. HIEFTJE. 2001. Mass analyzers for inductively coupled plasma

time-of-flight mass spectrometry. *Journal of Analytical Atomic Spectrometry* 16: 1206–1216.

ROWE, C.H. 1970. Pretzel Magnet for Wide Range Spectrum Analysis of Electron Beams up to 35 MeV. *In* Proceedings of the Third International Conference on Magnet Technology. Hamburg Deutsches Elektronen-Synchrotron (1970, 589-605.

SIE, S.H., T.R. NIKLAUS, D.A. SIMS, F. BRUHN, G. SUTER, AND G. CRIPPS. 2002. AUSTRALIS: a new tool for the study of isotopic systems and geochronology in mineral systems. *Australian Journal of Earth Sciences* 49: 601-611.

SKOOG, D., F.J. HOLLER, AND S.R. CROUCH. 2007. Principles of instrumental analysis. 6th ed. Thomson Brooks/Cole, Belmont CA.

STAN-SION, C. ET AL. 2002. Upgrading of the ultra-clean injector for depth profiling at the Munich AMS facility. *Nuclear Instruments and Methods in Physics Research Section B: Beam Interactions with Materials and Atoms* 192: 331-338.

SYNERGY SOFTWARE. 2010. KaleidaGraph - scientific graphing, curve fitting, data analysis software. Synergy Software. Available at: http://www.synergy.com/prodinfo.htm [Accessed August 2, 2010].

TAMBORINI, G., M. BETTI, V. FORCINA, T. HIERNAUT, B. GIOVANNONE, AND L. KOCH. 1998. Application of secondary ion mass spectrometry to the identification of single particles of uranium and their isotopic measurement. *Spectrochimica Acta Part B: Atomic Spectroscopy* 53: 1289–1302.

TAMBORINI, G., D. PHINNEY, O. BILDSTEIN, AND M. BETTI. 2002. Oxygen Isotopic Measurements by Secondary Ion Mass Spectrometry in Uranium Oxide Microparticles: A Nuclear Forensic Diagnostic. *Analytical Chemistry* 74: 6098-6101.

TÖRÖK, S., J. OSÁN, L. VINCZE, S. KURUNCZI, G. TAMBORINI, AND M. BETTI. 2004. Characterization and speciation of depleted uranium in individual soil particles using microanalytical methods. *Spectrochimica Acta Part B: Atomic Spectroscopy* 59: 689–699.

TOYODA, M. 2010. Development of multi-turn time-of-flight mass spectrometers and their applications. *European Journal of Mass Spectrometry (Chichester, England)* 16: 397-406.

TUNIZ, C., J.R. BIRD, D. FINK, AND HERZOG, GREGORY F. 1998. Accelerator mass spectrometry: ultrasensitive analysis for global science. CRC Press.

VERDEIL, C., T. WIRTZ, H. MIGEON, AND H. SCHERRER. 2008. Angular distribution of sputtered matter under Cs+ bombardment with oblique incidence. *Applied Surface Science* 255: 870-873.

VERENTCHIKOV, A.N., W. ENS, AND K.G. STANDING. 1994. Reflecting time-of-flight mass spectrometer with an electrospray ion source and orthogonal extraction. *Analytical chemistry* 66: 126–133.

VERENTCHIKOV, A.N., M.I. YAVOR, Y.I. HASIN, AND M.A. GAVRIK. 2005. Multi-reflecting TOF analyzer for high resolution MS and parallel MS-MS. *Mass Spectrometry* 2: 11–22.

WALLENIUS, M., P. PEERANI, AND L. KOCH. 2000. Origin determination of plutonium material in nuclear forensics. *Journal of Radioanalytical and Nuclear Chemistry* 246: 317–321.

WEAVER, J., S.R.F. BIEGALSKI, AND B.A. BUCHHOLZ. 2009. Assessment of non-traditional isotopic ratios by mass spectrometry for analysis of nuclear activities. *Journal of Radioanalytical and Nuclear Chemistry* 282: 709-713.

WILSON, R.G., F.A. STEVIE, AND C.W. MAGEE. 1989. Secondary ion mass spectrometry: a practical handbook for depth profiling and bulk impurity analysis. Wiley.

YOON, O.K., I.A. ZULETA, J.R. KIMMEL, M.D. ROBBINS, AND R.N. ZARE. 2005. Duty cycle and modulation efficiency of two-channel Hadamard transform time-of-flight mass spectrometry. *Journal of the American Society for Mass Spectrometry* 16: 1888-1901.

ZARE, R.N., F.M. FERNÁNDEZ, AND J.R. KIMMEL. 2003. Hadamard Transform Time-of-Flight Mass Spectrometry: More Signal, More of the Time. *Angewandte Chemie International Edition* 42: 30-35.